The composition of cometary ices as inferred from measured production rates of volatiles

Von der Fakultät für Elektrotechnik, Informationstechnik, Physik
der Technischen Universität Carolo-Wilhelmina
zu Braunschweig
zur Erlangung des Grades einer
Doktorin der Naturwissenschaften
(Dr.rer.nat.)
genehmigte
Dissertation

von Manuela Lippi
aus Carrara, Italien

Contents

Summary

Comets are believed to be the remnants of our Solar System formation, and the study of the chemical and physical features of cometary nuclei (as production rates, excitation conditions and rotational temperatures in the coma, relative abundance of isotopes, ...) can provide important information regarding the composition and the physical conditions prevailing in the proto-planetary nebula, and the delivery of water and organics to the early Earth.

Comets today reside in two distinct reservoirs, the Oort cloud and the Kuiper belt region, and they are grouped dynamically into several orbital categories. A new paradigm to explain the formation and dissemination of comets has been proposed (the Nice model, Gomes et al. (2005)): this model predicts that comets formed in the outer proto-planetary disk (10-30 AU) and entered both the Oort cloud and the Kuiper disk, though likely in different proportions. Thus, a comparison of chemical taxonomies in different populations can test a possible radial gradient in the chemistry of icy planetesimals in the proto-planetary disk, along with the dynamical models that predict their dissemination.

Using high-dispersion spectroscopy in the mid-IR (between about 3 to 5 μm), a number of parent gas species, sublimating directly from cometary nuclei, can be measured; in total, less than 20 comets have been studied so far using this technique, and, even if these studies indicate at present three distinct classes based on nuclei organic composition ("organic enriched", "organic normal" and "organic depleted"), it is evident that this sample is too small to be representative for the whole population.

The present work constitutes a contribution to the study of chemical compounds in comets. In particular, the actual knowledge of the physical phenomena that governs the molecular emissions in the coma and the observational techniques used in the infrared spectral region for this kind of investigations are described. A model for the ν_1 vibrational transition of the HCN molecule has been developed, and a review of the mathematical steps needed to retrieve the chemical composition from measured emission line fluxes in comets is given.

Inorganic and organic parent molecules were detected and analyzed in two comets, 8P/Tuttle (hereafter 8P) and C/2007 W1 (Boattini) (hereafter C/2007 W1), using CRIRES at ESO Very Large Telescope.

8P is an Halley type comet with an orbital period of 13.6 years and an orbital inclination of about 55 degrees. It has been observed in January 2008 (heliocentric distance and geocentric distance ranging from about 1.027 to 1.028 AU and 0.48 to 0.54 AU, respectively; maximum visual brightness $M_v \approx 5.3$ mag), when the observational conditions were highly favorable for infrared detections of parent volatiles from cometary ices. The comparison between 8P and other comets reveals that this comet is depleted

in CO (carbon monoxide), CH_4 (methane), C_2H_6 (ethane), and HCN (hydrogen cyanide), but at the same time it is very enriched in CH_3OH (methanol). Different explanations for this unusual behavior are given: it could be that 8P/Tuttle is constituted of two quite different cometesimals (radar observations of this comet show a bilobate nucleus (Harmon et al., 2008)), or, more simply, that it belongs to a new taxonomical class not observed before. For 8P, HCN and CN production rates (the latter retrieved from optical observations, Schleicher and Woodney (2007)) were compared: CN production rate was found to be higher than the HCN ones, suggesting that the latter cannot be considered the only parent molecule for the CN radical.

Comet C/2007 W1 is a dynamically new comet coming from the Oort cloud. It was observed, for the first time, in May 2008 and in the beginning of July 2008 (heliocentric distance and geocentric distance ranging from about 1.17 to 0.86 AU, and from 0.34 to 0.30 AU, respectively; maximum visual brightness $M_v \approx 7$ mag). The comparison of its composition with the one of already observed comets reveals that this comet is enriched in carbon compounds, so that it was possible to classify it as an organic enriched comet.

Finally, possible correlations between dynamical and chemical classes were investigated for different comets, but no obvious relationships were found.

1 Comets: introduction

Comets are one of the most charming astronomical events that one can observe in the sky. In the past apparitions of comets were often related to bad omens, and for many centuries these bright objects had been considered strange phenomena generated in the Earth atmosphere.

Only in 1577 Tycho Brahe, in the attempt to measure the parallax shift of a comet from two different locations, demonstrated that comets were extraterrestrial objects, further away than the Moon. Successively, Edmond Halley, using Newton's gravitational law, was able to calculate the orbital parameters and the period for a few comets, predicting with success the return of a bright comet (1P/Halley). This coincided with the beginning of cometary science. During early times comets had been studied basically only from the point of view of their dynamics, and for a long time their physical nature remained unknown.

In 1949 Fred Whipple hypothesized a model to describe the nature of comets (Whipple, 1949): this model became famous under the name of the "dirty snow ball" hypothesis. According to Whipple, a comet was a solid nucleus only a few kilometers in diameter, composed mainly of water ice mixed with solid particles. When far from the Sun, the nucleus is too small to be observed as resolved but, as soon as it approaches the Sun, the ices present on the top surface layers of the nucleus are released and the comet transforms in the spectacular object that people can see.

Whipple's theory was confirmed only in March 1986, when the first image of a cometary nucleus was taken by the spacecraft GIOTTO (see Fig. 1.1). Shortly before that time, only the composition of the plasma tail of comet 21P/Giacobini-Zinner had been observed via the International Cometary Explorer spacecraft, in September 1985.

Since 1986 other comets have been explored *in situ* by space missions[1]; moreover the increasing capabilities of telescopes have permitted to gather more and more information about these celestial objects. Nevertheless, still a lot of questions remain unsolved: which is the internal composition of cometary nuclei? Where did comets form and how had they evolved during time in our Solar System? Can we consider comets as the most primitive remains of our Solar System formation?

The aim of this chapter is to give a brief overview of what is known about comets nowadays. In particular, in the first section the structure of comets will be described together with their dynamical classification. The second section will concentrate more on the chemical aspect of these bodies, while in the third section scenarios on cometary origins and connections with the Solar System origins and evolution will be given.

---

[1]Comet 26P/Grigg-Skjiellerup, by GIOTTO in 1992, comet 19P/Borrelly by Deep Space1 in 2001, comet 81P/Wild 2, by Stardust in 2004 and comet 9P/Tempel 1, by Deep Impact in 2005.
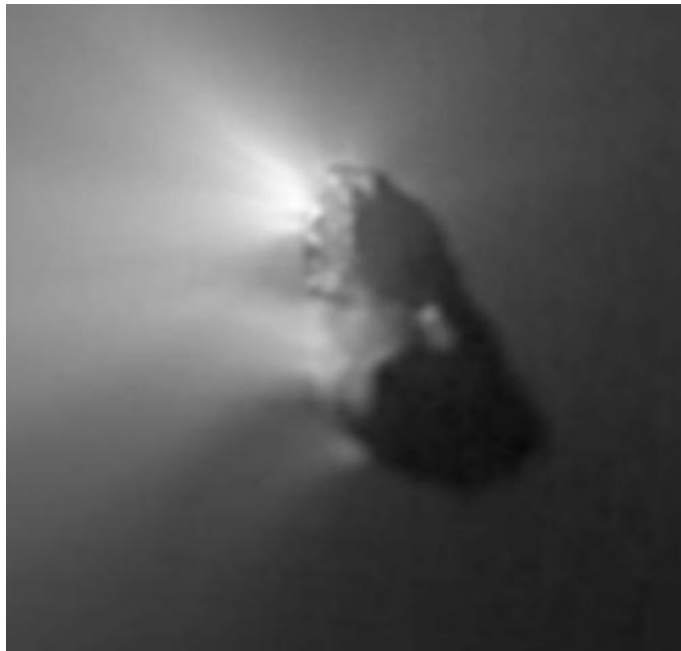
Figure 1.1: Halley's nucleus as seen from GIOTTO spacecraft during its close approach, in March 1986. In the same period 1P/Halley had been observed also from Vega1, Vega2, Suisei and Saki-gake spacecrafts. (Source: http://spiff.rit.edu/classes/phys301/lectures/comets/comets.html).

1.1   What is a comet?

The main component of a comet consists in a few kilometers size body, composed mainly of ices and dust, called **nucleus**. Little is known about the physical properties of the nucleus and the few information that are available nowadays come mainly from spacecraft observations. Ground based photometric observations can also provide important issues (see for example Lamy et al. (2004)), although not at the same great details as spacecrafts.

As soon as a comet approaches the Sun it becomes active (see Fig. 1.2): due to the solar radiation, the ices present on the top surface layers of the nucleus start to sublimate and the comet develops a **coma**. In the sublimation process also part of the solid material is dragged away, so that the coma composition consists of gas and dust; a cometary coma can reach a diameter of 10^6 km.

During the activity period the comet develops also two tails: the **ion tail** and the **dust tail**. The ion tail forms because the molecules previously released from the nucleus surface are photo-dissociated by solar UV radiation; consisting of charge particles, the ion tail is driven away from the coma by the solar wind, in the anti-solar direction. Dust that is released during the sublimation process is instead driven by the Sun radiation pressure and it will form the dust tail; dust and ion tails can both be as long as $10^7 - 10^8$ km.

As the comet absorbs ultraviolet light, dissociation of molecules, ions and radicals in the coma will produce hydrogen, which will form a **hydrogen envelope**; this envelope cannot be seen from Earth because its light is absorbed by the atmosphere, but it has been detected by spacecrafts. During the observations of comet Hale Bopp, in 1997, astronomers have discovered the existence of a **neutral gas tail** composed mainly of atomic sodium (not indicated in Fig. 1.2, Cremonese et al. (1997)); this tail is located
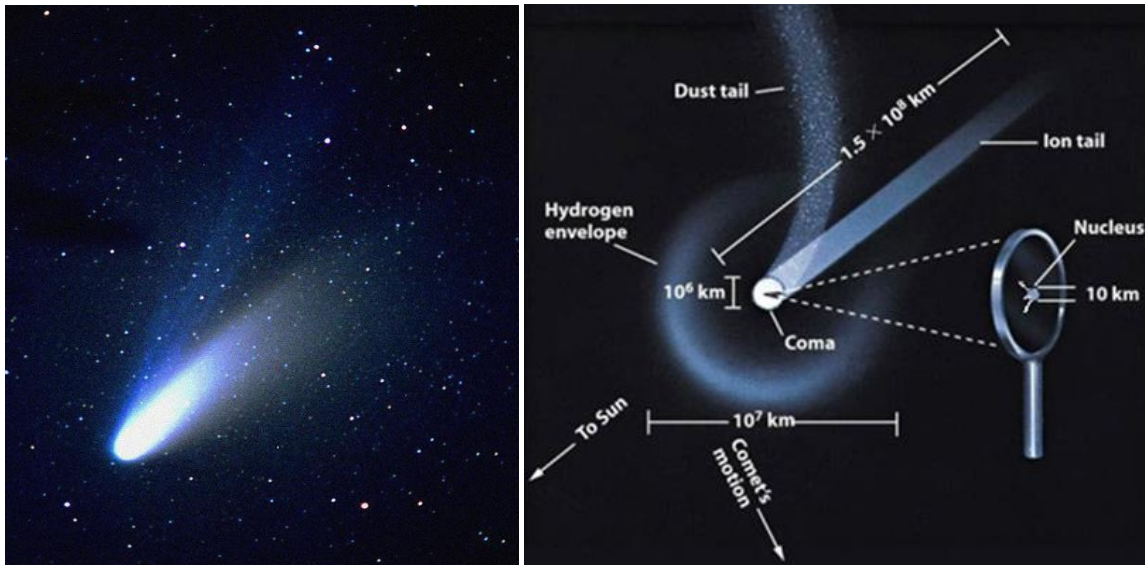
Figure 1.2:   Comet Hale-Bopp in the 1995 apparition (on the left) and the corresponding structure (on the right).   For a description of the single indicated elements see the text.   (Sources: http://astronomy.swin.edu.au/sao/imagegallery/Hale-Bopp.jpg and http://www.daviddarling.info/images/comet_structure.jpg).

between the dust and the gas tail and its origin is still not completely clear. Probably it generates from sodium atoms that are formed in the coma and pushed out through radiation pressure, or it could also be possible that the sodium atoms are created in the tail, through either collisions between dust grains or the bombardment of the dust grains with ultraviolet light from the Sun (process of sputtering).

The level of activity for a comet is related to a lot of factors, but in particular it depends on the nucleus composition and on its distance from the Sun (this concept will be explained more in details in section 1.2.4).

It is particularly difficult to observe the nucleus of a comet even when it gets close to Earth since, in the active phase, the light coming from the nucleus is contaminated by the light coming from the coma, consisting mainly of sunlight reflected by the dust particles.

1.1.1   Cometary reservoirs and dynamical taxonomy

For a long time cometary research had been restricted mainly to the study of the dynamical properties of these bodies. Depending on their orbital period P, comets can be classified in short period comets ($P < 200$ years) and long period comets ($P > 200$ years). Two big reservoirs of cometary nuclei are known in our Solar System [2] (see Fig. 1.3):

- **the Oort cloud:** it has been postulated in 1950 by Oort (Oort, 1950), who made a systematic study of orbital parameters of long period comets. The Oort cloud is a vast spherical cloud surrounding our planetary system, at heliocentric distance

---

[2]Recent observations of main belt asteroids revealed that few of them exibith a quite low activity, similar to the one of comets. If to consider these objects as comets and the main asteroid belt as a new cometary reservoir is still under debate.

11
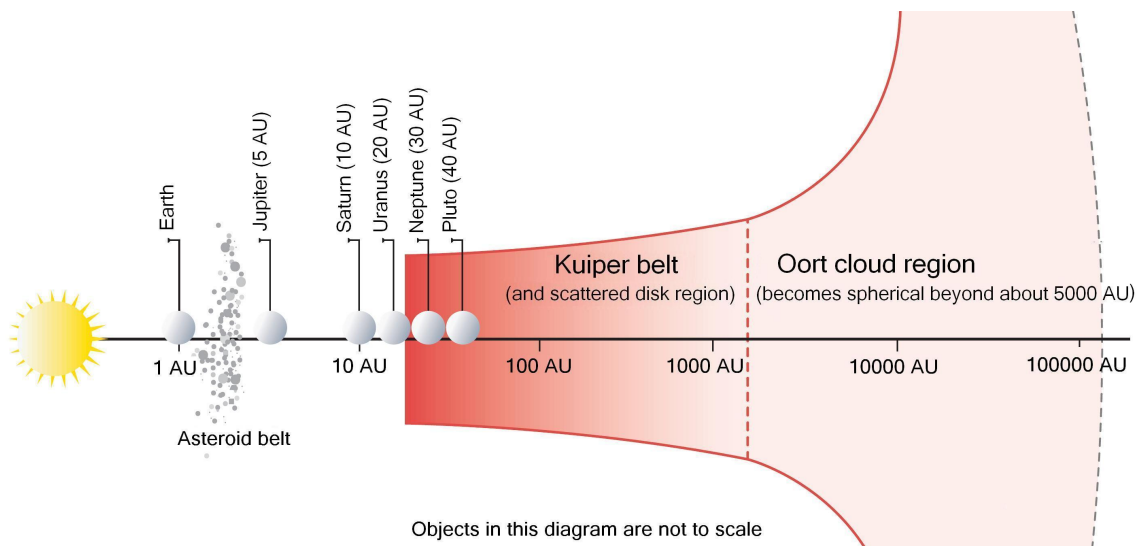
Figure 1.3: A schematic view of the expected position of cometary reservoirs in our Solar System. Note that the objects in the diagram are not scaled, and that the Oort cloud becomes spherical beyond about 5000 AU. (Source: Stern (2003)).

$r_h \geq 10^4$ AU. Comets coming from the Oort cloud are randomly distributed, they have highly eccentric orbits and they enter in the planetary system when their orbits are perturbed by nearby stars, by close encounters with giant molecular clouds or by the tidal field of the galactic disk. When a Oort cloud comet enters in the planetary system its orbit can be perturbed and changed by the gravitational effects exercised by the giant planets, so that a long period comet can evolve, after a certain time, in a short period one.

- **The Kuiper belt:** the majority of short period comets belongs to the Kuiper belt, an almost flattened annulus of objects beyond the orbit of Neptune. Dynamical studies of the trans-neptunian region show that orbits with semi-major axis $a < 35$ AU and $40 < a < 42$ AU are unstable to gravitational perturbations by Neptune and Uranus: some of the Kuiper belt objects in the unstable zones can then evolve inwards and form a source of short period comets.

Oort cloud and Kuiper belt comets can be dynamically classified in classes according the Tisserand's parameter, a quasi-constant in the three body problem Sun-Jupiter-comet:

$$T_J = \frac{a_J}{a} + 2\sqrt{\frac{a}{a_J}(1 - e^2)} \cos i. \tag{1.1}$$

Here a_J is the semi-major axis of Jupiter orbit, while a, e and i are respectively the semi-major axis, the eccentricity and the inclination of the orbit of the comet, with respect to the ecliptic. Depending on the value that the Tisserand's parameter assumes, the orbit of the considered body is under the gravitational influence of Jupiter or not; in general for comets $T_J < 3$, even if very few comets have $T_J > 3$ (although only slightly so).

Following Levison classification (Levison, 1996), comets can be classified in two big classes that can be divided, in turn, in other sub-classes (see Fig. 1.4):
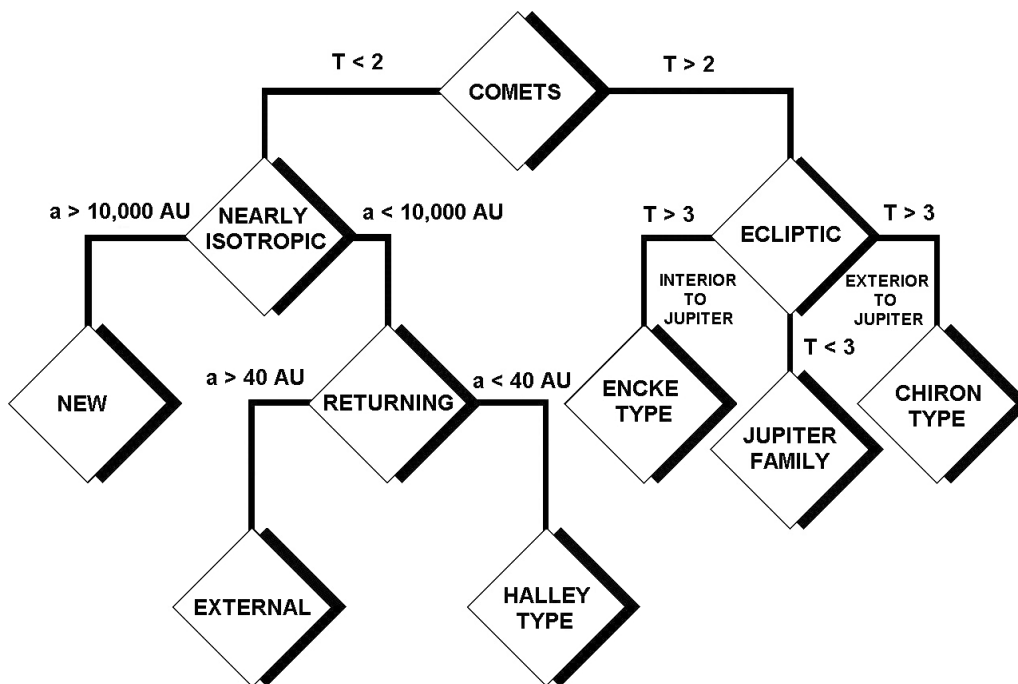
Figure 1.4: Cometary dynamical classification according Levison. Depending on the Tisserand's parameter T comets are classified in two big groups (ecliptic and nearly isotropic). The two classes are then divided in other subclasses, depending on the semi-major axes a, in case of nearly isotropic comets, and on their Tisserand's parameter for ecliptic comets (Source: Levison (1996)).

- **ecliptic comets**: ecliptic comets come from the Kuiper belt; these are comets with Tisserand's parameter $T_J > 2$; they have short periods (< 200 years) and small inclinations. They can be divided in three sub-categories:

  - **Jupiter family comets**: comets with $2 < T_J < 3$, whose orbits are completely dominated by Jupiter influence;

  - **Encke type comets** : comets with $T_J > 3$ and with semi-major axis a internal to Jupiter's orbit (i.e. $a < a_J$);

  - **Chiron type comets**: comets with semi-major axis beyond Jupiter's orbit ($a > a_J$) and Tisserand's parameter $T_J > 3$.

- **Nearly isotropic comets**: nearly isotropic comets come mainly from the Oort cloud, and they are characterized by $T_J < 2$. Comets injected into the inner planetary system are grouped dynamically into several orbital categories:

  - **returning comets**: the class of returning comets regroup a large number of objects characterized by long periods, semi-major axes $a > 40$ AU, and a nearly isotropic distribution of the inclinations.

  - **Halley type comets**: these objects are characterized by $T_J < 2$ and they have semi-major axis $a < 40$ AU, orbital periods ≤ 200 years and a distinctly non-random distributions of inclinations. To explain the isotropic distribution of Halley type comets the existence of an inner Oort cloud is postulated. The

inner Oort cloud should consist in a disk extended between 2000 and 20000 AU and with median inclinations that range from 10 to 50 degrees.

– **Dynamically new comets**: this class contains comets whose orbits suggest that they have entered the inner Solar System for the first time.

The current location of comets is a result of dynamical events that affected our Solar System in the early age. Probably comets had formed in the outer planetary region, between Jupiter and Neptune; in a second moment, due to gravitational interactions with the forming giant planets, the majority of them had been expelled outside the Solar System to form the Oort cloud, while others moved in the Kuiper belt, or in the inner Solar System, where they died in impacts with the planets and the Sun. A possible scenario that can explain the observed distribution is the **Nice Model** (Gomes et al. (2005) and Charnoz and Morbidelli (2007)), that will be briefly described in section 1.4.

1.2   Chemical properties of cometary volatile ices

Comets are considered among the most primitive bodies of our Solar System. Since they are rather small, and since they live the majority of their life in cold environments, far away from the Sun, they cannot have undergone much thermal evolution, and probably only the outer layers of the nucleus have been modified through bombardment by energetic charged particles, cosmic rays, or through surface erosion by interstellar grains or dust debris; moreover, the surface of cometary nuclei in the Oort cloud may have been heated by passing stars or supernova explosions. Despite the various processes that could have affected the surface of a nucleus during its history, its internal composition should have remained widely unchanged since the time of its formation, and it should reflect the composition of the proto-planetary disk, in the place where it formed.

The chemical composition of cometary nuclei could be different for comets that had evolved in different dynamical ways (for instance between Oort cloud and Kuiper belt objects), since different processes may have affected the cometary material during time: short period comets have been subjected more times to solar radiation than long period comets, and they should show a lower content of volatile material and a more highly processed surface. The extent to which comets are modified, depending on their history from their initial state, is a fundamental question in cometary science.

In situ exploration represents the best way to determine the nuclear chemical composition; unfortunately, space missions are very expensive and sophisticated and lots of technical difficulties can be encountered so that, until now, they were restricted only to a very small number of comets (see the first note of this chapter). In particular, among these missions, Giotto, Vega1 and Vega2, Stardust and Deep Impact were designed to study the chemical composition of a cometary nucleus.

In 1986 Giotto made the closest approach to comet 1P/Halley and it provided pictures of a cometary nucleus, very important to study in details its physical properties like the dimension, the shape, the albedo, the temperature, the density and the rotational period, and to understand which percent of the surface is active; moreover, during this mission, the chemical composition of the ejected material from the comet (gas and dust) was retrieved through mass spectroscopy. In the same year, Vega1, along with its twin Vega2,

were used to help Giotto's upcoming flyby, providing images of comet Halley; these images, as well as the ones from Giotto, were intended to measure the physical parameters of the nucleus, as well as to study the structure and dynamics of the coma and the gas and dust composition close to the nucleus.

Stardust flew by comet 81P/Wild 2, taking detailed pictures of its nucleus, collecting, during the flyby, dust samples from the comet's coma and returning them to Earth: the analysis of these samples is still not complete, but important information have been already obtained.

Deep Impact, launched on January 12th, 2005, released an impactor on the nucleus of comet 9P/Tempel 1; from the impact internal material was ejected and could be studied.

The next very important step in cometary research will be done with the Rosetta space mission, in 2014, when for the fist time a scientific spacecraft will operate for a long time interval in orbit around the nucleus of comet 67P/Churyumov-Gerasimenko, and a lander, equipped with different instruments, will be sent on its surface, providing important issues on cometary chemistry.

Nowadays our knowledge of the chemical composition of cometary nuclei, its variation among comets and its variation with time and heliocentric distance is based mainly on ground based measurements of intensity flux lines that are emitted by molecules excited by solar radiation in the coma. This investigation is indirect because it considers only molecules that are released from the nucleus surface and that can be affected by numerous processes: if stored in the Kuiper belt, ultraviolet radiation from the Sun can induce losses of hyper volatile elements or produce chemical reactions on the nucleus surface. For comets stored in the Oort cloud instead, the loss of hyper volatiles can happen when a comet is heated by supernovae or passing stars. In both the cases collisions, cosmic rays and interactions with gas and dust present in the interstellar medium can erode the surface, changing its original chemistry. Differences in composition are then expected between the surface and the bulk material of a nucleus, and from comet to comet; how the molecular composition and abundance of the coma is related to the one inside the nucleus is still an open issue.

1.2.1   Gas sublimation, production rates and mixing ratios

The main process through which the material is released from the nucleus is sublimation induced by the solar heating. Molecules that are released directly from the nucleus are called **parent molecules**, while the ones that are created afterwards, via photo-dissociation of parent molecules by the solar radiation, are called **daughter molecules** (see Fig 1.5); due to their nature, parent molecules are expected to be more representative of the nuclear composition and they should give fundamental information about the chemical properties of a comet. Spectroscopy of daughter molecules provides complementary information for the chemistry and the physics of the coma, and the relative abundances of these molecules can be related, using suitable models, to the ones of parent molecules. Unfortunately, for some daughter species the identity of the corresponding parent remains ambiguous or unknown, and spectroscopy of parent molecules remains the best way to deduce the internal composition of the nucleus.

The sublimation process depends on many parameters, like dust/ice ratio or composition and internal physical structure of the nucleus, and it is governed by the balance
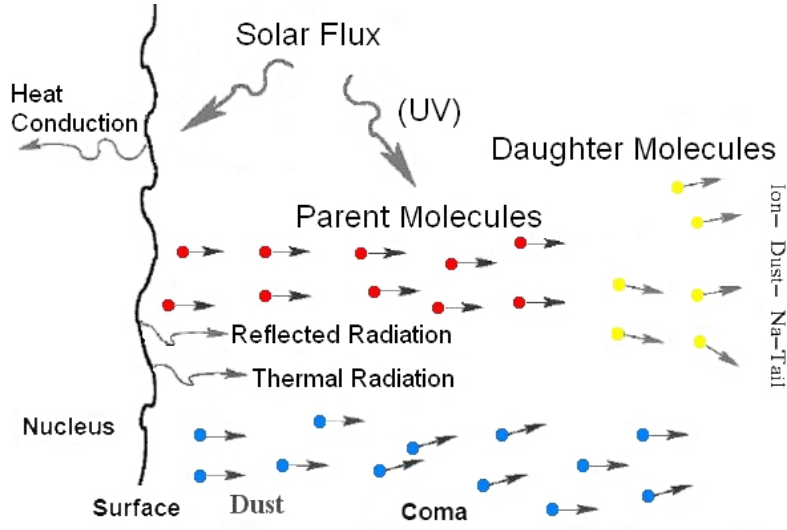
Figure 1.5: Parent molecules (red dots), daughter molecules (yellow dots) and dust (blue dots) in a cometary coma; various physical processes (like heat conduction and thermal emission) are also indicated. (Adapted from: Jewitt (2008)).

between the effective incident solar radiation energy on the surface, the reflected radiation, the thermally re-radiated energy, and the energy used for volatile sublimation and internal heat conduction.

Assuming only solar heating, and using the approximation of a homogeneous and spherical nucleus of radius R, the energy balance between the energy absorbed by the surface of a cometary nucleus and the emitted one is given by:

$$\frac{F_\odot e^{-\tau}\left(1 - A_b\right)}{4\pi r_h^2}\pi R^2 = 4\pi R^2 \epsilon\sigma T^4 + QL_s\left(T\right) + 4\pi R^2 K_T \frac{\partial T}{\partial z}, \qquad (1.2)$$

where $F_\odot$ denotes the incident solar flux at 1 AU, τ is the optical depth of the coma, r_h the heliocentric distance of the comet in AU, A_b the comet albedo, ϵ the infrared emissivity, Q is the gas production rate of the sublimating chemical specie, $L(T)$ the latent heat used for sublimation at temperature T, and K_T is the thermal conductivity. In the above equation, the term on the left side represents the energy received from the Sun, while the three terms on the right side represent the losses caused by thermal infrared reradiation, the losses due to sublimation of ices and the ones due to the heat conduction in the nucleus, respectively. Unfortunately, many of the critical parameters that govern the sublimation process are still only poorly known; comparisons of observations with models provides constraints for the assumptions and parameters on which models are based (see for example Prialnik et al. (2004)).

A valid help in testing sublimation models comes from spectroscopic observations of cometary emission lines in the inner coma: from these observations it is in fact possible to retrieve the chemical and physical conditions in the cometary inner coma, like the **production rates** of different molecular species, i.e the number of molecules that are released per second from the cometary surface, and the temperature of the sublimating gas. The processes involved in the molecular excitation and in emission lines creation in the coma will be reviewed in chapter 2, and a detailed description of the steps needed to

Species	Method	Origin	M.R.%
H_2O	R, IR, MS	P	100
OH	R, IR, UV	D	100
CO	R, IR, UV, MS	P, D	$0.4 \div 30$
CO_2	IR, MS	P	$2 \div 6$
CH_4	IR	P	$0.14 \div 1.4$
C_2H_2	IR, MS	P	$0.2 \div 0.5$
C_2H_6	IR, MS	P	$0.11 \div 0.67$
CH_3OH	R, IR, MS	P	$0.15 \div 6.2$
H_2CO	R, IR	P	$0.13 \div 4$
NH_3	R, IR, MS	P	$0.5 \div 1.5$
HCN	R, IR, MS	P	$0.08 \div 0.25$
NH	V	D	$0.11 \div 1.6$
S_2	UV	?	$0.0012 \div 0.005$
SO_2	R	P	0.2
SO	R	D	0.2
H_2S	R, MS	P	$0.12 \div 1.5$

Table 1.1: Averaged mixing ratios, relative to water, for some cometary molecules. In the table, R means observed in the radio, IR in the infrared, V in the visible, UV in the ultraviolet, MS with mass spectroscopy. P and D indicate if the molecule is a parent or a daughter one, respectively. For the mixing ratios the minimum and the maximum reported values are indicated; single molecules are discussed in the text. (Table adapted from Jewitt (2008)).

translate the measured fluxes in production rate will be given in chapter 5.

The abundance of minor volatiles is usually provided in terms of **mixing ratio**, that is the ratio between the production rate of the considered specie and the one of the the main activity driver, that is H_2O for comets closer than 3 AU to the Sun. If Q_i is the production rate of a particular species i, and Q_{H_2O} is the one relative to the water, the mixing ratio is given by:

$$M.R. = \frac{Q_i}{Q_{H_2O}} 100\%. \tag{1.3}$$

1.2.2   Main parent molecules and some important daughter molecules in comets

The majority of the results on parent and daughter molecules have been derived from remote spectroscopic observations at UV, IR and radio wavelengths, and from few *in situ* measurements using mass spectroscopy. In particular, in the past decade, remarkable progress have been made in the instrumental capabilities at IR and radio wavelengths and over two dozen parent cometary molecules have now been detected; a list of the most common confirmed molecules found in the coma is listed in table 1.1.

The main volatile constituent of the nucleus is water ice, followed by carbon monoxide. Although the activity of cometary nuclei is dominated by these two main ices, the minor species, with abundances of at most a few percent, give important clues for the understanding of the origin and formation of comets. A relative overview of the most

important constituents in comets is given hereafter.

Water and water derived molecules

- **Water (H_2O):** water ice is the most abundant parent volatile in cometary nuclei and it dominates the gaseous activity within 3 AU. The determination of H_2O production rates is therefore of vital importance to characterize cometary activity. The first detection of water was made in December 1985, via infrared spectroscopy from the Kuiper Airborn Observatory (KAO) on 1P/Halley (Mumma et al., 1986), but its existence was already indirectly established before. Water emission lines are difficult to be measured directly from ground based telescopes, since, depending on the wavelength range, they can be strongly absorbed by the water vapor in the terrestrial atmosphere.

- **Hydroxyl (OH):** hydroxyl is an interesting and useful daughter molecule: its abundance is directly related to its parent molecule H_2O, and it can be then used to derive or to confirm water production rates in most comets. The OH radical has been observed extensively in the UV ($\sim$ 3000 Å) and radio (1665 and 1667 MHz, near 18 cm) spectral regions.

- **Atomic hydrogen (H):** observation of the HI Lyman-α emissions at $\lambda = 1216$ Å revealed the existence of a huge atomic hydrogen cloud surrounding the cometary coma; it is believed that water is the main parent molecule for H.

Carbon compounds

- **Carbon monoxide (CO) and carbon dioxide (CO_2):** the second most abundant volatile in comets is CO. The CO molecule was discovered in comets in the UV spectrum ($\sim$ 1500 Å, (Feldman et al., 1997)); successive observations revealed mixing ratios [CO/H_2O] ranging from $\sim$ 0.4% to nearly 30%. Radio lines of CO are intrinsically weak because of the small dipole moment of this molecule, however, these lines are the most easily detected gaseous emissions for comets at large heliocentric distances ($r \geq 3$ AU). The first clear detection of IR CO emission lines near 4.7 μm was obtained during observations of comet Hyakutake (Mumma et al., 1996). CO is considered a parent molecule but it is suspected to come (at least partly) from an extended source, i.e. CO is released not only from the nucleus surface but likely also from cometary dust in the coma.

  The presence of carbon dioxide in comets was indirectly confirmed by the existence of a related daughter product, CO_2^+, in cometary tails (Feldman et al., 2004). The IR CO_2 band (around 4.6 μm) is expected to be quite strong, but unfortunately it is absorbed by the terrestrial atmosphere and observations of CO_2 in this region have been performed only by the Vega, ISO and GIOTTO spacecrafts. [CO_2/H_2O] abundances range from 2 to 6%. The ions CO^+ and CO_2^+, observed in the cometary coma, are probably produced by photodissociation of a large fraction of CO and CO_2.

- **Methanol (CH_3OH) and formaldehyde (H_2CO):** identification of methanol in cometary comae was obtained first from the detection of several rotational lines

at 145 GHz in comets C/1989 X1 (Austin) and C/1990 K1 (Levy) at the 30-m telescope of the "Institut de Radioastronomie Millimétrique (IRAM)" (Bockelee-Morvan et al., 1991). Methanol has now been observed in many comets, both at radio and infrared wavelengths, and the CH_3OH abundances inferred from these observations are generally consistent. The $[CH_3OH/H_2O]$ abundance ratios measured up to now range from less than 0.15% to 6%, with many comets around 2%.

Cometary formaldehyde was first identified in 1P/Halley by mass spectroscopy on board GIOTTO spacecraft. H_2CO may appear also from extended sources. Its abundance in comets is quite low and for this reason observations by IR long-slit spectroscopy are difficult. DiSanti et al. (2002) reported the detection of the Q-branch of the H_2CO-ν_1 band in high resolution spectra of 153P/Ikeya-Zhang, obtained with CSHELL at NASA/IRTF. For all the comets the $[H_2CO/H_2O]$ ratio has been estimated between 0.13% to 1.3%, with the exception of comet 1P/Halley (4%).

- **Methane (CH_4), ethane (C_2H_6) and acetylene (C_2H_2):** methane, ethane and acetylene have been first clearly detected spectroscopically in comet C/1996 B2 (Hyakutake) through ground based observations in the IR region, around 3.3 and 3.35 μm (Mumma et al., 1996); typical $[CH_4/H_2O]$ mixing ratios range from 0.14% to 1.4%, while $[C_2H_2/H_2O]$ range from 0.2% to 0.5% and $[C_2H_6/H_2O]$ are remarkably constant 0.6%. Symmetric hydrocarbons cannot be observed in the radio spectral region: in fact, due to their geometry, the dipole moment for these molecules is zero, and thus rotational transitions, that correspond to emission lines in this region, are forbidden.

- **C_2, C_3 and CH**: observations of comets in the UV and in the visible ranges revealed the existence of numerous carbon daughter species. Among them C_2 and C_3, both observed in the visible and in the UV spectral ranges. The former is believed to form from C_2H_2, while the parent relative to the latter is still unknown. CH is also a daughter products, likely created from photo-dissociation of methane that decay first in CH_2 and then in CH; CH is observed in the visible and infrared ranges, and since in the IR it is more easy detectable than CH_4, it exist a significantly larger database of detections for this molecule.

Nitrogen compounds

- **Ammonia (NH_3):** the most abundant N-bearing molecule in the gas phase is ammonia. Radio emissions of the NH_3 molecule are weak and can be detected only in bright comets. Ammonia was tentatively detected in the radio (24 GHz) for comet C/1983 H1 (Altenhoff et al., 1983), and its existence was confirmed by the observations of several lines in comets Hyakutake (Palmer et al., 1996) and Hale Bopp (Bird et al., 1997), from which abundances of $\sim$ 0.5% were derived. Ammonia can be observed also in the IR, around 3.00 μm, but also in this case the target has to be really bright. It is possible to investigate this parent moelcule indirectly, observing its photodissotiation products NH and NH_2 in the visible (Feldman et al., 2004). Ammonia mixing ratios $[NH_3/H_2O]$ are estimated to be between 0.5 and 1.5%.

- **Hydrogen cyanide (HCN) and cyanide (CN):** HCN was firmly detected in comet 1P/Halley in the radio range, at 88.6 GHz (Despois et al., 1986). It is now one of the most easiest parent molecules to observe from the Earth and it can serve as a proxy for monitoring gas production rates evolution. HCN has been observed in several comets, in the radio and in the infrared regions, and abundances relative to H_2O range from 0.08 to 0.25%.

  CN has been observed easily in the visible spectral range since the earliest days of cometary spectroscopy, but its origin is still not completely understood. One of the candidate parent molecules is HCN, but directly comparisons showed inconsistencies with this hypothesis, and about $20 - 50\%$ of the CN is thought to come directly from the dust grains present in the coma (see for example Fray et al. (2005)).

Sulfur compounds

- **Sulfur monoxide (SO) and dioxide (SO_2):** SO and SO_2 have been detected so far only in comet Hale Bopp through several rotational lines in the radio region (Bockelée-Morvan et al., 2000). It is likely that SO is the main daughter product coming from the photo-dissociation of SO_2. Abundances up to 0.2% have been found for these two molecules.

- **Hydrogen sulfide (HS) and disulfur (S_2):** hydrogen sulfide is believed to be the most abundant sulfur parent molecule in comets, and it was first detected at 169 GHz at the IRAM-Telescope in comets C/1989 X1 (Austin) and C/1990 K1 (Levy) (Bockelee-Morvan et al. (1991), Crovisier et al. (1991)). [H_2S/H_2O] ranges from 0.12 to 1.5%.

  The S_2 molecule was discovered in the UV, near 2900 Å (A'Hearn et al., 1983); the most common form of solid sulfur is S_8 and the discovery of S_2 in a comet was the first detection of this unusual molecule in any astronomical object.

- **Carbon monosulfide (CS):** CS emissions are observed in the UV (the most strong band is at $\approx$ 2576 Å) and in the radio. The most likely parent is CS_2; another possible source could be OCS, detected in the radio, but the contribution of this last compound is expected to be minor.

Dust composition

The composition of cometary dust has been measured *in situ* from Giotto (ESA) and the two soviet Vega spacecrafts; moreover, dust samples have been collected and sent to Earth during the Stardust mission (NASA). Three main dust components have been individuated (Kissel et al., 1986; Flynn et al., 2006):

- particles similar to CO chondrites: Na, Mg, Si, Ca, Fe ($\approx 35\%$);

- particles consisting mainly of light atoms: C, H, O, N (the so-called CHON particles) ($\approx 30\%$); CHON particles are believed to consist mainly of organic material;

- particles consisting of silicates, but also light elements (mixture of the two cases) ($\approx 35\%$).

The analysis of the dust grains sampled by Stardust revealed also the presence of abundant amorphous silicates in addition to crystalline silicates, such as olivine and pyroxene; the presence of both amorphous and crystalline silicates implies a mixture of materials that were processed in different ways (low temperatures for the amorphous component, high temperature for the crystalline one).

Information on the chemical and mineralogical composition of cometary dust grains can also be obtained from spectral observations (Hanner and Bradley, 2004): small silicate grains in the dust coma are detected around $10\,\mu m$ and at longer wavelengths (between $16\,\mu m$ and $35\,\mu m$, not accessible from the ground). Also in this case, the resulting dust composition is compatible with a combination of crystalline and amorphous grains.

The properties that characterize cometary dust seem to have no counterpart in any meteoritic material, with the exception of the interplanetary dust particles (IDPs); these particles are thought to originate from comets, or at least from a significant part of their population, and they can be analyzed in order to retrieve additional information on cometary dust composition (see for example Hanner and Bradley (2004)).

1.2.3   Isotopic ratios

Isotopic ratios are a crucial diagnostic of the physical-chemical conditions that prevailed during the formation of cometary material; chemical models of the primitive solar nebula predict, for example, a strong dependence of the ratio between water (H_2O) and deuterated water (HDO) on heliocentric distance r_h, so that in principle it is possible to determine the r_h distribution of the formation site for different comets from the distribution of the D/H enrichment.

The D/H ratio for water molecule has been detected only in two Oort cloud comets, C/1996 B2 (Hyakutake) (Bockelee-Morvan et al., 1998) and C/1995 O1 (Hale-Bopp) (Meier et al., 1998) and in two Halley type comets, 1P/Halley (Eberhardt et al., 1995) and 8P/Tuttle (Villanueva et al., 2009); these kind of measurements are in fact restricted to few bright targets, or to space mission targets, because emission lines of HDO are quite weak with respect other emission lines, and thus more difficult to be detected. All four determinations are a factor of ten larger than the proto-solar value and close to D/H $\approx 3 \cdot 10^{-4}$, i.e. twice the Vienna Standard Mean Ocean Water (VSMOW).

The comparison between cometary and terrestrial D/H ratios reveals that cometary water is different from the terrestrial one. This can lead to the conclusion that another source, different from comets, is needed to explain the presence of water on the Earth, but at the same time it is still not possible to reach a firm conclusion considering only four measurements between the large amount of comets in our Solar System. It would be crucial to determine D/H ratios for a large number of comets, and in particular for Jupiter family comets, since there are still no measurements available for this dynamical class.

The inferred isotopic ratios for other elements ($^{14}N/^{15}N$, $^{12}C/^{13}C$, $^{32}S/^{34}S$) are sparse and limited to few comets, and they are expected to be different in Jupiter family comets and Oort cloud comets if the two populations formed at different places or different times in the solar nebula. So far, most isotope ratios reported for comets (except for D/H)

Isotopes	Molecule	Comet	Method	Comet Value	Solar System	ISM
[D/H]	H_3O^+	Ha	MS	$(3.08 \pm 0.53)10^{-4}$	$(1.49 \pm 0.03)10^{-4}$	$1.5\ 10^{-5}$
				$(3.02 \pm 0.22)10^{-4}$	(Earth)	
	H_2O	Hy	R	$(2.9 \pm 1.0)10^{-4}$		
		Hb	R	$(3.3 \pm 0.8)10^{-4}$		
		Tu	IR	$(4.09 \pm 1.45)10^{-4}$		
[$^{12}C/^{13}C$]	HCN	Hb	R	111 ± 15	89.9	77 ± 7
				90 ± 15		
				109 ± 22		
		Hy	R	34 ± 12		
	CN	WM1	R	115 ± 20		
		Ha	V	95 ± 12		
[$^{14}N/^{15}N$]	HCN	Hb	R	323 ± 46	272	450 ± 100
				330 ± 98		
	CN	Hb	V	150 ± 40		
	CN	WM1	V	140 ± 15		
[$^{32}S/^{34}S$]	CS	Hb	R	27 ± 3	22.6	32 ± 5

Table 1.2: Some of the isotopic ratios measured in comets, compared with solar and interstellar values. Except for comet 8P/Tuttle (Villanueva et al., 2009), values are taken from Bockelée-Morvan et al. (2004), and the original papers referenced therein should be cited. (R = radio, IR = infrared, V = visible, MS = mass spectroscopy; Hb = Hale Bopp, Ha = 1P/Halley, Hy = Hyakutake, WM1 = C/2000 WM1 (LINEAR), Tu = 8P/Tuttle).

Molecule	Sublimation Temperature (K)	Heliocentric Distance (AU)
CO	25	120
CH_4	31	80
C_2H_6	44	40
C_2H_2	57	24
H_2S	57	24
NH_3	78	14
CO_2	80	13
HCN	95	8
CH_3OH	99	8
H_2O	152	3

Table 1.3: Temperatures and heliocentric distances at which various volatiles start to sublimate. (Source: Meech and Svoren (2004)).

are compatible with the terrestrial values (see Altwegg and Bockelée-Morvan (2003)); in table 1.2 a review of some measured isotopic ratios in comets is reported.

1.2.4   Heliocentric evolution of production rates

The evolution of production rates along a cometary orbit depends on the available solar energy and on the volatility of the species: different molecular species will in fact sublimate at different temperatures, i.e. at different distances from the Sun (see Tab. 1.3 and Fig. 1.6); moreover the sublimation rate will depend on the structure and the percentage of active nucleus surface (presence or not of jets, night/day effects, ...).
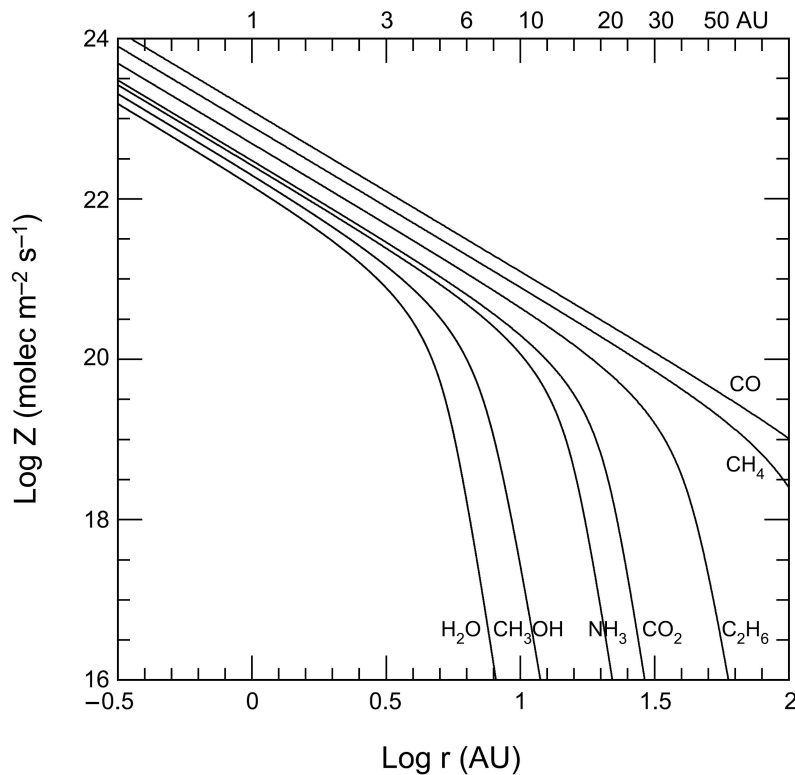
Figure 1.6: Production rates Z as a function of the heliocentric distance ($\log(r)$), for various molecules present in comets, calculated assuming an isothermal nucleus of albedo $A_b = 0.04$. (Adapted from: Meech and Svoren (2004)).

It is particular important to determine the cometary activity, if present, at large heliocentric distances and over a wide range of r_h, to cover the long term evolution of different species: numerical simulations of the structure and evolution of a comet nucleus show variations of the ratios of volatiles along the orbit (see Fig. 1.7); moreover, it can be demonstrate that if a comet is monitored for a sufficiently large portion of its orbit, the integration over time of the derived production rates can provide averaged relative abundances that should be quite close to those prevailing in the nucleus.

The systematic differences in the dependence of the production rates from the heliocentric distance can be used to get a rough estimate of the relative depths below the nucleus surface, where these species originate, or of the nature of the ices (crystalline or amorphous ices); comets that present an upper layer containing crystalline ice are expected to show a quite different evolution of gas activity with respect to comets where amorphous ice is still present close to the surface (the heat conduction of amorphous ice is about four times lower than for the crystalline one (Prialnik et al., 2004)).

Unfortunately, activity far from the Sun is very low and it is possible to study the heliocentric evolution of volatiles only for very bright comets; moreover, comets are usually observed mostly only at singular distance range and only in the water-driven sublimation regime, inside $r_h \approx 3$ AU.

Figure 1.8 shows an example of the heliocentric evolution of production rates for comet Hale Bopp. This comet was active enough to permit the monitoring of the sublimation of different ices, even at large heliocentric distance (7 AU). The evolution of
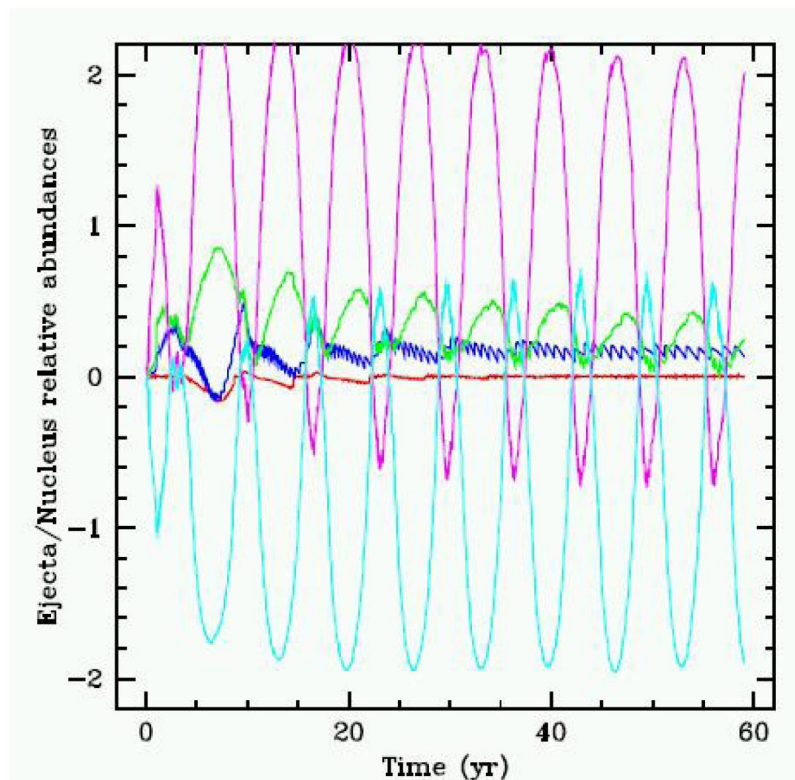
Figure 1.7: Modeled abundance ratios as a function of time, along several orbital revolution. (Blue CO/CO_2, green CH_4/NH_3, cyan HCN/NH_3, magenta CO_2/HCN, red CO/CH_4. (Source: Prialnik (2006)).

production rates of different molecules appears quite different: for example, when the comet is further than 3 AU, the heliocentric dependence of CO production rate is less steep than the one of OH, while, for heliocentric distances < 3 AU, the two volatiles show a similar evolution, until perihelion. After perihelion the same behavior is repeated, but in a reverse order. Other volatiles are characterized by production rates evolutions that can be similar either to CO or to OH, depending on their volatility.

In general, the approximate heliocentric evolution of production rates is represented by a power law, r_h^{-k}, obtained by fitting the slope of $\log(Q)$ over $\log(r_h)$.

For example, for comet Hale Bopp the retrieved heliocentric evolutions for production rates were $Q(H_2O) \propto r_h^{-1.88\pm0.18}$ molecules/s (between 1.49 and 0.93 AU from the Sun) $Q(CO) \propto r_h^{-1.76\pm0.26}$ molecules/s (between 4.10 and 2.02 AU from the Sun, DiSanti et al. (2001)), $Q(C_2H_6) \propto r_h^{-2.43\pm0.13}$ molecules/s (between 3.01 and 2.83 AU from the Sun, Dello Russo et al. (2001)); comet 153P/Ikeya-Zhang, observed between March and April 2002, showed a steeper heliocentric dependence for the water molecule production rate compared to comet Hale Bopp: $Q(H_2O) \propto r_h^{-3.21\pm0.26}$ molecules/s (between 0.51 and 0.78 AU from the Sun, Dello Russo et al. (2004)).

When the sublimation rate is dominated by the insolation the heliocentric dependence is expected to scale as r_h^{-2} but, in reality, the resulting exponent k can vary significantly from comet to comet and from species to species, suggesting that the sublimation rate is controlling also by other physical processes; moreover, when comparing pre- and post-

24
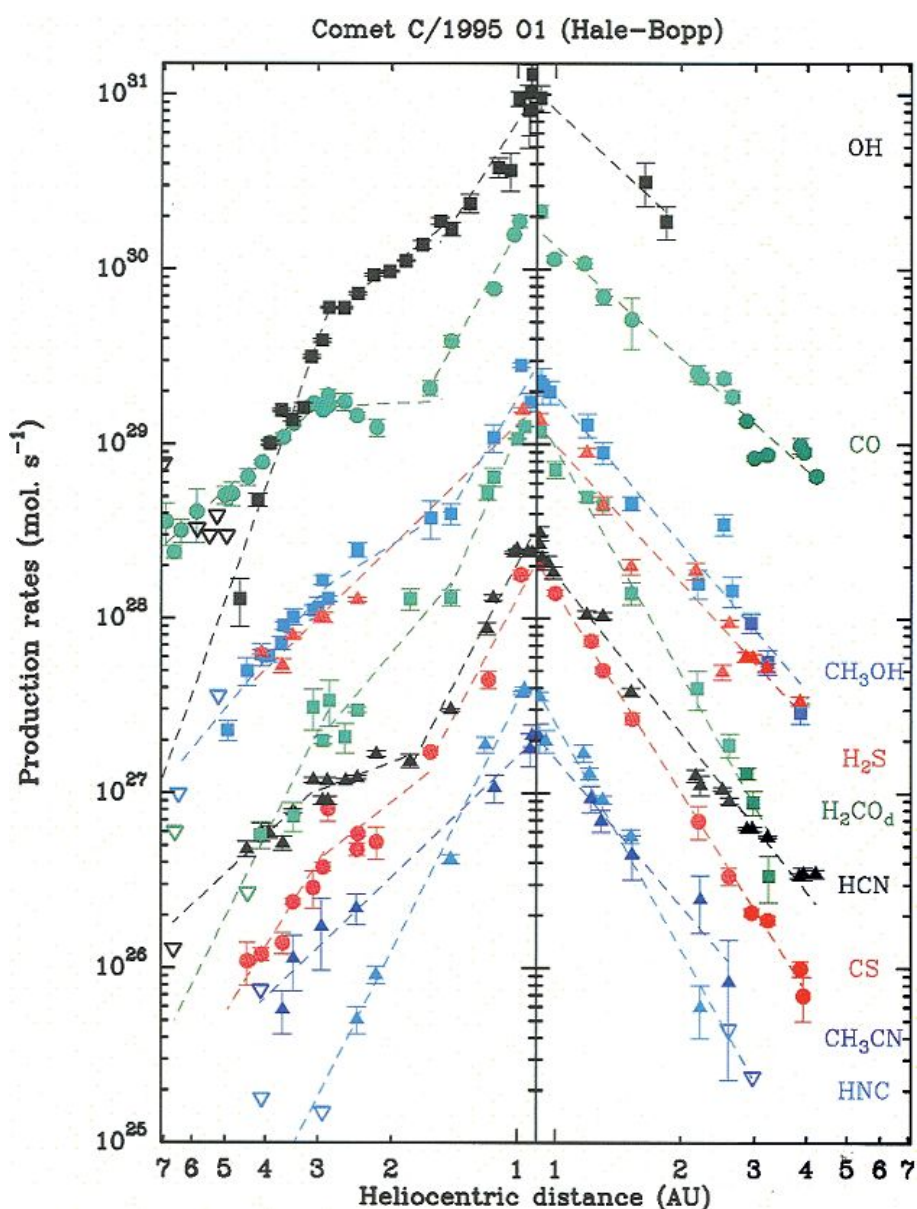
Figure 1.8: Gas production rates over heliocentric distance of comet Hale-Bopp, during the 1995 apparition. (Source: Biver et al. (1997)).

perihelion observations, the overall activity evolution is very similar for the monitored parent species on the inbound and outbound path, but some systematic differences in the evolution of gas activity can be seen.

Although the composition of a relatively large number of comets have been investigated through the study of the production rates of different nuclear species, the systematic sampling of production rates as a function of heliocentric distances is very poor, since only few comet are bright enough to be monitored along a sufficiently part of their orbit, and further observations are needed to better understand the processes, besides sublimation, through which molecules are released from the nucleus.

25

1.3 Chemical diversity among comets: the need of a new taxonomy

The increasing capabilities of infrared and radio instrumentation made it possible to measure detailed and reliable molecular abundances for a bunch of comets. The number of comets studied so far is still quite low, nevertheless, some trends begin to emerge. A preliminary classification based on the organic chemistry of comets revealed that at least three classes exist: **"organic depleted"**, **"organic normal"** and **"organic enriched"**; moreover, some comets show a quite high or low amount of certain species relative to the others ("super enriched" and "super depleted" comets, respectively). In table 1.4 mixing ratios measured for different comets are listed, while in figure 1.9 the same values are plotted.

It is particularly interesting to verify if connections between dynamical and chemical classes are present. From figure 1.9 it is possible to notice that, on average, Jupiter family comets tend to be more depleted in the most volatile species than comets that come from the Oort cloud, even if exceptions are present (see for example comet C/1999 S4, a depleted Oort cloud comet that disintegrated during its apparition, in 2000); in general, it is still not possible to correlate without doubts chemical compositions and dynamical classes of comets.

The main question that arises is if these compositional differences are connected with different nuclei formation regions, with different evolutionary history for different comets, or with the combination of these two possibilities.

The presence of higher or low contents of hyper volatile ices, as CO and CH_4, could be a stringent clue to the formation temperature of comets, since these ices condense at temperatures lower than 30 K; on the other hand, the apparent volatile depletion of Jupiter family comets relative to Oort cloud comets may be caused by thermal processing from multiple passages close to the Sun.

Whereas the HCN/H_2O ratio is relative constant, several species, such as CO, CH_3OH and H_2CO, show important variations from comet to comet; this can suggest that a substantial radial mixing of elements occurred in the proto-solar nebula, as predicted by current dynamical models (see next section). This possible mixing can explain why C/1999 S4 and 73P/Schwassman-Wachmann, belonging to different dynamical classes, are both carbon-depleted, and why it is possible to find comets that show a similar chemical composition even if coming from different present day reservoirs.

Indeed the separation between the three chemical classes is not really sharp, and it is necessary to measure more and more comets to better define their chemical taxonomy.

Comet	CO	CH$_4$	C$_2$H$_6$	C$_2$H$_2$	HCN	CH$_3$OH
Oort Cloud comets						
C/2004 Q2	5.07 ± 0.51	1.36 ± 0.22	0.54 ± 0.08	0.07 ± 0.01	0.15 ± 0.05	1.77 ± 0.19
C/1999 H1	1.80 ± 0.20	0.84 ± 0.26	0.67 ± 0.07	0.25 ± 0.04	0.21 ± 0.03	1.72 ± 0.73
C/2000 WM1	0.52 ± 0.12	0.34 ± 0.10	0.47 ± 0.09	< 0.05	0.15 ± 0.02	1.22 ± 0.30
C/2006 P1	1.45 ± 0.18	0.26 ± 0.05	0.36 ± 0.05	0.39 ± 0.09	0.19 ± 0.03	-
C/2001 A2	3.86 ± 1.02	1.65 ± 0.40	1.61 ± 0.38	0.36 ± 0.15	0.46 ± 0.19	3.68 ± 0.25
C/1996 B2	15.7 ± 4.24	0.78 ± 0.31	0.61 ± 0.22	0.16 ± 0.08	0.18 ± 0.04	1.7 ± 0.4
C/1995 O1	13.26 ± 3.16	1.16 ± 0.42	0.63 ± 0.26	0.29 ± 0.18	0.40 ± 0.10	2.4 ± 0.3
C/2006 M4	0.49 ± 0.20	0.82 ± 0.09	0.49 ± 0.05	-	-	3.35 ± 0.79
C/1999 S4	0.75 ± 0.43	0.12 ± 0.03	0.13 ± 0.02	< 0.14	0.10 ± 0.03	< 0.17
Halley Type comets						
1P/Halley	3.5	< 1	0.4	0.3	0.2	1.7
153P/I.Z.	4.7 ± 0.8	0.49 ± 0.15	0.62 ± 0.09	0.18 ± 0.05	0.18 ± 0.04	2.5 ± 0.5
Jupiter Family comets						
21P	10.31 ± 1.87	-	0.22 ± 0.05	< 0.35	< 0.22	1.15
73P-B	< 1.9	-	0.17 ± 0.05	< 0.03 ± 0.01	0.29 ± 0.05	0.19 ± 0.08
73P-C	0.53 ± 0.07	< 0.25	0.11 ± 0.07	0.05 ± 0.02	0.19 ± 0.11	0.19 ± 0.05
17P (Outburst)	-	-	1.85 ± 0.92	0.34 ± 0.05	0.54 ± 0.07	2.37 ± 1.09
9P(Pre Impact)	-	-	0.19 ± 0.12	-	0.18 ± 0.06	1.23 ± 0.11
9P(Post Impact)	4.3 ± 1.7	0.54 ± 0.30	0.35 ± 0.03	0.13 ± 0.04	0.21 ± 0.03	0.99 ± 0.17
6P	-	-	0.29 ± 0.12	< 0.05	0.03 ± 0.01	1.61 ± 0.32

Table 1.4: Organic parent volatile abundances in different comets (H$_2$O = 100 %). For each comet, the green indicates whereas the comet is enriched in a particular carbon compound, while the orange if it is depleted; cyan and magenta indicate if the comet is super enriched or super depleted respectively. References, production rates and other interesting values for the listed comets are tabulated in appendix D.
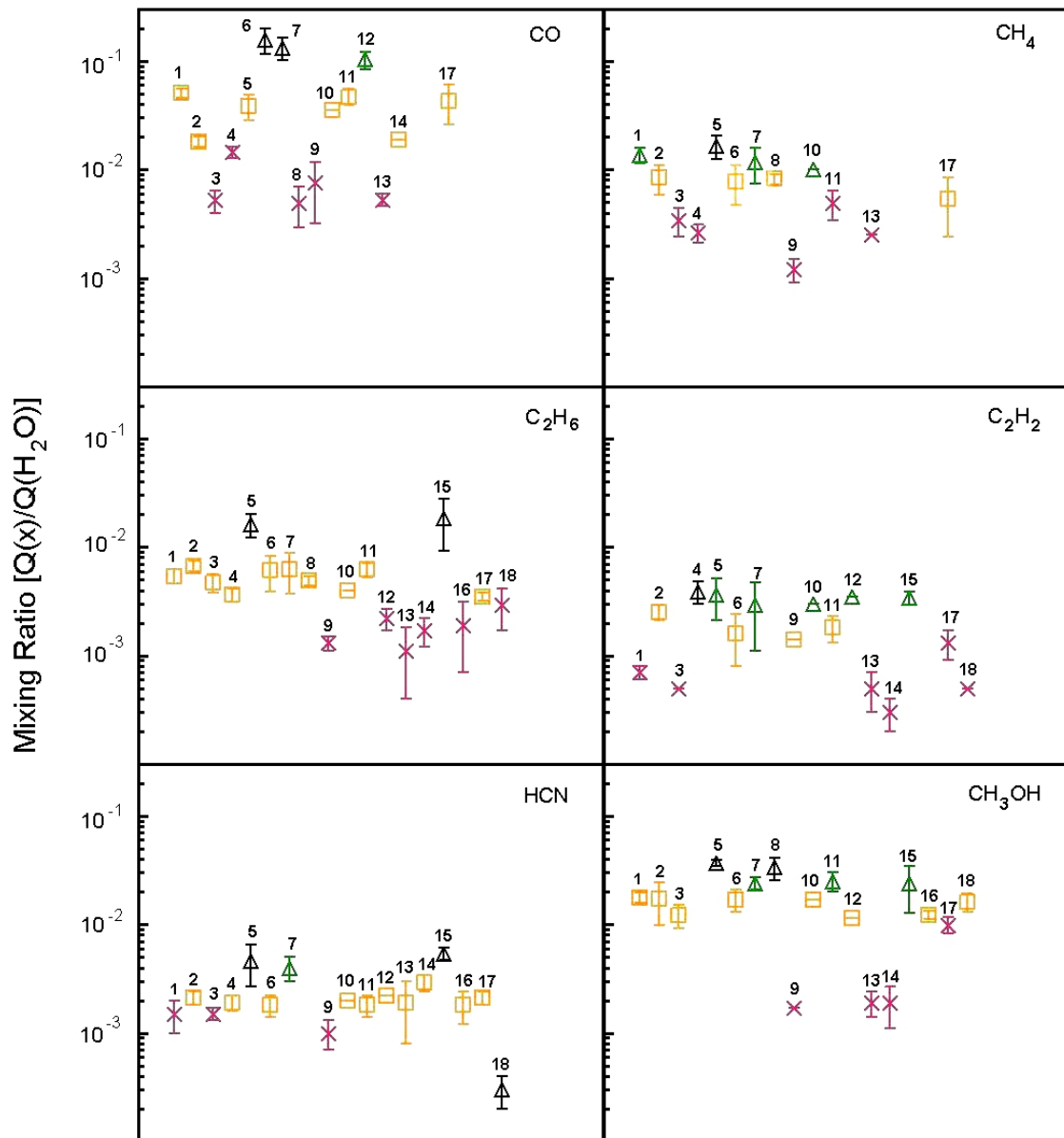
Figure 1.9: Comparison between organic mixing ratios in different comets; for each box different mixing ratios (with respect to the water) relative to a certain species are plotted. For each number, a different comet is represented: 1 = C/2004 Q2(Machholz), 2 = C/1999 H1 (Lee), 3 = C/2000 WM1 (LINEAR), 4 = C/2006 P1 (McNaught), 5 = C/2001 A2, 6 = C/1996 B2 Hyakutake, 7 = C/1995 O1 (Hale-Bopp), 8 = C/2006 M4 (Swan), 9 = C/1999 S4 (LINEAR), 10 = 1P/Halley, 11 = 153P/Ikeya-Zhang, 12 = 21P/Giacobini-Zinner, 13 = 73P/Schwassmann-Wachmann-C, 14 = 73P/Schwassmann-Wachmann-B, 15 = 17P/Holmes, 16 = 9P/Tempel 1 (Pre-impact), 17 = 9P/Tempel 1 (Post-impact), 18 = 6P/D'Arrest, 19 = 8P/ Tuttle (highlighted by a green box). For each of these comets, references, production rates and other interesting values are tabulated in appendix D. For each molecule, green, yellow and red indicate if the comet is organic enriched, normal or depleted respectively; black is used for super enriched and super depleted comets.

1.4   Comets origins: connections with the the Solar System formation and evolution

Comets can be considered among the most primitive objects of our Solar System: they formed relatively far from the Sun, at distances where the relatively cold temperature could preserve the pristine chemical conditions of the proto-planetary nebula. They have been stored in the Kuiper belt and the Oort cloud for a long time, and hence they are less thermally processed compared to other bodies of the Solar System. Cosmic rays, interstellar radiation, and solar radiation in case of a passage within the inner Solar System, probably have modified the original composition of their surface, but still cometary nuclei should preserve information on their origins.

The formation of our Solar System started, most probably, from the collapse of a molecular cloud containing mainly H and He gas, as well as tiny amounts of solid particles (Ehrenfreund et al., 2004). In this scenario, it can be thought that pre-solar material has been chemically and physically processed according to the distance from the proto-Sun: material of the nebula that was entering the proto-planetary disk far out from the proto-Sun is expected to be largely unmodified when first incorporated, while, due to an higher temperature, material infalling the proto-planetary disk closer to the to the proto-Sun is expected to be completely, or in part, re-processed. In the first case, chemical reaction will proceed as this material is transported radially inward, while, in the latter, the reprocessed material can give origin in a second moment to molecules that are then radially mixed out. If comets formed from the debris of the disk material they should contain a mixture of both interstellar and processed material and their composition should differ according to their place of formation.

A recent dynamical model, the "Nice Model" (Gomes et al., 2005), asserts that comets formed all in the same region, between about 15 AU and 35 AU from the Sun. Successively, the migration of the forming giant planets from their initial configuration into the positions that they occupy nowadays produced strong gravitational effects on these bodies: the majority had been scattered in the Oort cloud, while others had been stored in the Kuiper belt. The study of cometary chemical compositions and its comparison with dynamical models can thus represents a unique opportunity to reconstruct the history of the formation of the Solar System and its early evolution. If existing, chemical differences among comets, and heterogeneity of a single nucleus, may argue for a chemical gradient present in the proto-planetary nebula.

Chemical compositions and isotopic ratio values can be used as possible indicators of the temperature that was present in the formation regions: the presence of highly volatile ices (CO, S_2, NH_3) in cometary nuclei may suggest a forming temperature between 20 and 25 K, that correspond to a distance in the solar nebula of about $r_h \geq 20$ AU. Rare gases, also very volatile, are crucial probes of the temperature history, but have not yet been convincingly detected (Bockelée-Morvan et al., 2004).

Isotopic ratios provide severe constraints on the origin of comets: as seen in table 1.2, while the large values found for water and deuterium suggests for a possible incorporation of interstellar material in comets, the values relative to other species appear, in general, to be more consistent with the formation of cometary nuclei in the solar nebula, suggesting for a possible double nature of cometary nuclei.

Species like CO_2, CH_3OH, OCS, NH_3 and CH_4 are observed both in cometary nuclei and in the interstellar medium, and they could provide constraints on a possible link between the origin of comets and the cloud from which our Solar System formed; on the other hand, molecules like C_2H_2, C_2H_6 and HCN have still not been observed in the solid phase of interstellar medium, suggesting a probable reprocessing of the material in the forming proto-planetary nebula.

Radial gradients in the temperature and chemical composition of the solar nebula and the extent of mixing of material between the warm inner regions and cold outer regions of the nebula, at the epoch of comet formation, should be evident today as differences in dust properties among comets related to their place of origin (Hanner and Bradley, 2004).

The overall picture of cometary nuclei formation and evolution is still particular unclear: further improvements have to be done to increase the knowledge of the chemical composition and the physical properties of these bodies and to understand the role that they have played in the formation and evolution of our Solar System.

2 High resolution spectroscopy of comets in the IR

In order to have full understanding of the the origins and nature of comets, it is fundamental to obtain the best possible physical and chemical description of the nucleus; despite space missions, spectroscopy appears to be one of the most suitable tools to reach this goal.

A typical cometary spectrum of the coma consists in a series of emission lines superimposed on a continuum signal (see Fig. 2.1). The continuum signal is due to the presence of dust particles in the coma that reflect the solar radiation in the UV, visible, and infrared spectral regions, and emit thermal radiation for longer wavelengths. The emission lines superimposed on the dust continuum are produced by parent and daughter molecules via the mechanism of **fluorescence**, driven by direct solar radiation (Crovisier and Encrenaz, 1983; Weaver and Mumma, 1984; Yamamoto, 1982). The purpose of this chapter is to describe the mechanism of fluorescence for cometary parent molecules and the best spectroscopic techniques, in the infrared spectral range, used to study the composition of a cometary nucleus. Moreover, the description of the instrument used for the investigations presented in this thesis is given.

2.1 Fluorescence in cometary atmospheres

According to quantum mechanics, molecules are characterized by rotational, vibrational, and electronic states, corresponding to well defined energies[1]. Rotational energy is associated with the rotation of the molecule about its axes, vibrational energy with the vibrations of the atoms that constitute it, and electronic energy is related the arrangement of electrons around its various nuclei. Transitions can occur among rotational levels within a singular vibrational level (pure rotational transitions), among rotational levels of different vibrational bands but in the same electronic state (ro-vibrational transitions), and among ro-vibrational levels in different electronic bands (electronic transitions, see Fig. 2.2).

When a molecule changes from one state to another one, a photon of well define wavelength is emitted or absorbed: every change in the rotational energy will correspond to emission or absorption lines in the radio region of the spectrum, while changes of vibrational states will give rise to infrared lines; the transitions related to a change in the electronic state will produce instead lines in the UV, visible and sometimes in the near infrared (see Fig. 2.3).

---

[1]A description of molecular spectra for diatomic molecules is given in Appendix B
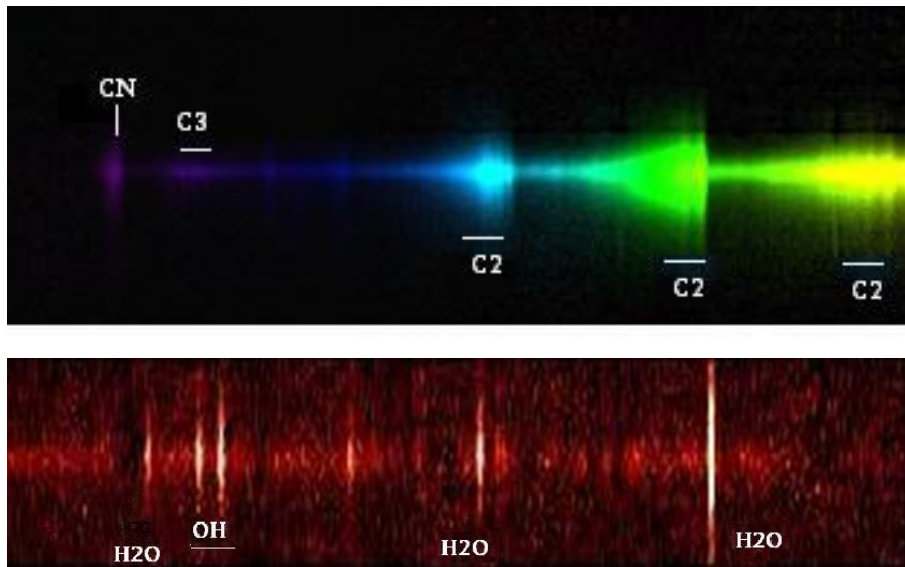
Figure 2.1: Different types of cometary spectra. On the top: low resolution visible spectra in the region between 3600 and 5800 Å, of comet C/2001 Q4 (NEAT); emission of CN, C_3 and C_2 molecules are visible (Source: http://astrosurf.com/buil/us/neat/q4.htm). On the bottom: high resolution spectrum of comet 8P/Tuttle, in the infrared region between 3410 and 3395 cm^{-1}; molecular emission lines from H_2O and OH molecules are visible. In both the spectra it is possible to notice the reflected Sun spectrum (the weak continuum horizontal line).

A change in vibrational energy is always accompanied by a change in rotational energy, so that for a vibrational transition a band comprising several vibrational lines with different intensities will be generated. Similarly, an electronic transition will be accompanied by a change in rotational and vibrational energies, that will produce a system of bands.

Most of the emission lines that are detectable in cometary spectra are the result of a fluorescence process: a molecule in the coma, initially in the ground state level (or in general in a lower energy level), can absorb a solar photon with defined wavelength and energy. The molecule will then change to an excited state, i.e. it will be characterized by a different rotational, vibrational and/or electronic energy level, depending on the energy of the incident photon. Successively, the molecule will de-excite spontaneously, after a certain time, to the initial energy level, in one (resonant fluorescence) or more (non resonant fluorescence) steps, emitting one or several photons, respectively.

Since the molecule can be excited and can decay through various channels, corresponding to different changes of rotational, vibrational and electronic states, a rich and characteristic spectrum will be generated (see Fig. 2.4), and depending on the wavelength range it will be possible to study different properties that characterize the molecules in the coma:

- **radio**: through radio spectroscopy it is possible to study the rotational transitions of cometary parent molecules and some daughter products; in particular, this technique is more sensitive than others in case of cold atmospheres, i.e. for comets observed at high heliocentric distances. Radio spectrometers provide high spectral resolution ($\lambda/\partial\lambda \approx 10^6 - 10^7$): this helps to resolve the emission line profiles and
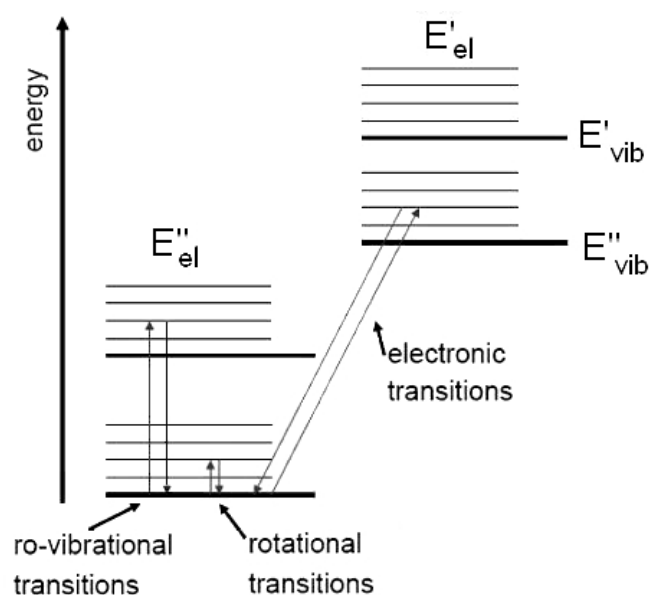
Figure 2.2: Representative scheme of energy levels of a hypothetical molecule. For two different electronic levels (E''_{el} and E'_{el}), the vibrational and rotational energy levels are plotted; rotational, ro-vibrational and electronic transitions are shown.
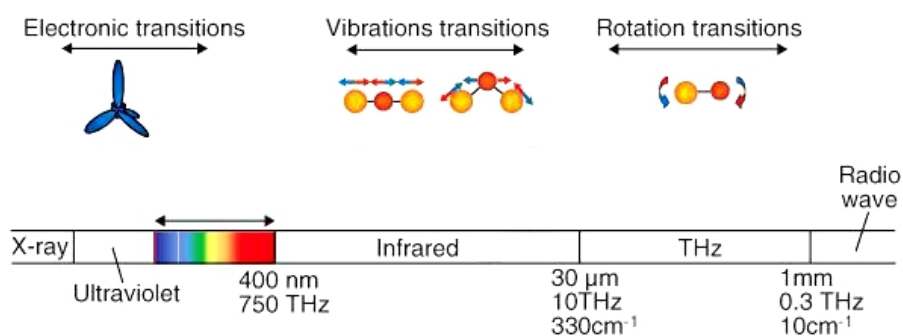
Figure 2.3:   Electromagnetic spectrum compared to rotational, vibrational and electronic transitions of molecules.   (Adapted from: http://images.pennnet.com/articles/lfw/thm/th_0801lfw3f1.gif).

to retrieve expansion velocities from the nucleus; high resolution is also important to eliminate ambiguities related to line blending. Unfortunately, radio emissions of some important parent molecules are not accessible through ground based observations, because strongly absorbed by the terrestrial atmosphere (this is for example the case of the fundamental rotational line of water at 557 GHz), and space observations are needed. Another limit to radio spectroscopy is the impossibility to detect symmetric molecules, such as CH_4, C_2H_2, and C_2H_6: in fact for these molecules, that do not have a permanent electric dipole moment, pure rotational transitions, and consequently corresponding radio emission lines, are forbidden.
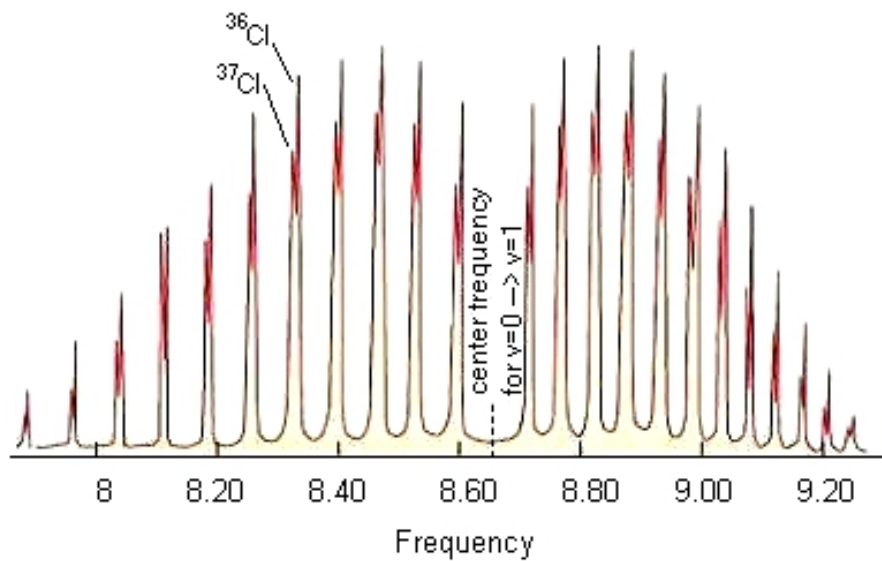
Figure 2.4: Molecular ro-vibrational spectrum for ^{36}Cl and ^{37}Cl molecules. For these two isotopes, the rotational structure of the vibrational band, corresponding to the vibrational transition from the ground state (v = 0) to the first excited state (v = 1), is shown. (Adapted from: http://hyperphysics.phy-astr.gsu.edu/Hbase/molecule/vibrot2.html).

- **Infrared (IR)**: strong emission bands of molecules in the coma are best observed in the near-IR region, between 2 and 5 μm, via fundamental ro-vibrational transitions: in this region, in fact, the molecules present in the coma receive abundant solar flux for exciting infrared fluorescence; moreover, in the same region thermal radiation and reflected sunlight from dust are not very strong (see section 2.1.2). Unlike the UV and part of the radio, this wavelength spectral region is partially accessible from ground based observations and, in principle, it is not necessary to perform space observations[2]. IR observations require very high resolution ($\lambda/\partial\lambda \gtrsim 20000$) to resolve the ro-vibrational spectra and to avoid unambiguously identification of the molecules (see section 2.2); in the past, due to the lack of suitable instruments, the study of cometary chemistry was limited to other spectral regions; in the last twenty years, with the advent of high-dispersion infrared spectrometers, the IR wavelength region have become one of the most important spectral region to investigate the physical and chemical properties of parent molecules in the inner coma. High resolution permits to resolve the rotational structure of the vibrational bands, fundamental to retrieve information about the internal excitation of the molecules; moreover, as in the radio, high resolution permits to unambiguously identify volatile species in spectrally confused regions (a typical example is the region between 3.3 and 3.6 μm, where all the hydrocarbons show features relative to the C-H stretching vibrational mode). IR spectroscopy is also very useful to investigate symmetric parent molecules, fundamental in characterizing cometary chemistry, but not observable in the radio.

---

[2]Even if partially accessible from the ground, the quality of IR observations depends strongly on the presence of water vapor and other molecules in the Earth atmosphere; in this respect, observations from space still represent the better way to study astronomical objects.

- **Visible and ultraviolet (UV)**: absorption of UV sunlight by molecular species in the inner coma leads to their destruction rather than fluorescence, with the consequence that only daughter molecules, like OH, CN, CH, NH, C_2, C_3, and some cometary parent molecules, like CO and S_2, can be observed in these regions. UV emissions coming from the cometary coma are absorbed by the terrestrial atmosphere, so that investigations in this wavelength range has to be carried by space platforms.

Since daughter products give only an indirect, and sometimes ambiguous, evidence of the initial composition of nuclear volatiles, it appears clear that IR and radio spectroscopy are the best ways to retrieve information on parent molecules.

In particular, it is important to concentrate cometary research in the infrared domain because many of the detectable molecular emission lines due to fluorescence of parent molecules, like H_2O, CO, CO_2, CH_4, together with the daughter specie OH, can be found in this region. Emission lines produced by fluorescence of these molecules can be observed easily with high resolution spectrometers, since they are strong with respect to the continuum spectrum of the dust and they are partially accessible from the ground. Moreover, in the IR spectral region it is possible to investigate the relative abundances of symmetric molecules necessary to have a complete picture of the chemical composition of the nucleus and to better understand its origin and evolution.

2.1.1 Fluorescence in the infrared

Since for most of the parent molecules non resonance fluorescence is less probable than resonant fluorescence, many observable infrared bands can be directly modeled through a two vibrational level analysis. Due to the low temperature in the coma, it can be assumed that the ground energy level is the most populated one, and consequently the strongest fundamental vibration bands of cometary parent molecules are the ones between the ground state and other vibrational levels. For the same reason, it is possible to assume a local thermodynamic equilibrium (LTE) in the ground vibrational state[3]; this will translate in a strong temperature dependency of the column density, i.e. the fraction of molecules that are within the instrumental field of view.

Let's consider two vibrational energy levels, v'' and v', with $E_{v''} < E_{v'}$; each of these level will be characterized by a certain number of rotational energy levels (see Fig. 2.5). For an individual ro-vibrational transition between a lower rotational energy state $l \in v''$ and a higher energy state $u \in v'$, the pumping rate, or fluorescence efficiency, g_{lu} (in s^{-1}), due to the solar radiation field, is given by

$$g_{lu} = \frac{c^3}{8\pi h v_{ul}^3} \frac{w_u}{w_l} A_{ul} J(v_{ul}), \qquad (2.1)$$

where w_l and w_u are the statistical weights of the lower and upper levels, respectively v_{ul} is the frequency of the transition, A_{ul} is the Einstein coefficient for spontaneous emission

---

[3]Fluorescence is a non thermal equilibrium process. If LTE is maintained in the coma, then IR fluorescence in the solar radiation field will not occur because of quenching by collisions. Under these circumstances the IR radiation from the molecules in the coma will be primarily thermal in nature (Weaver and Mumma, 1984).
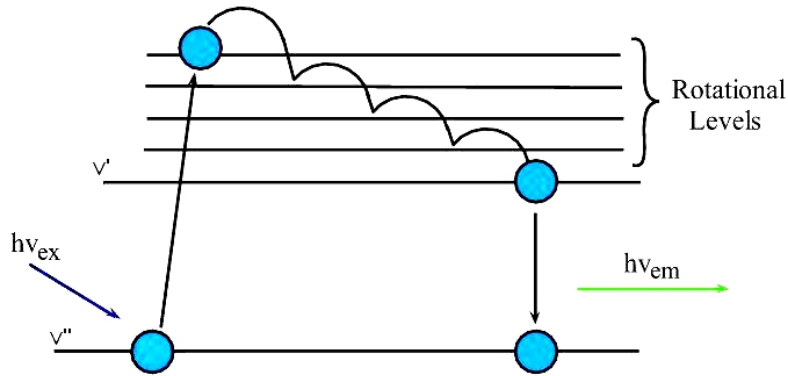
Figure 2.5: A simplified scheme for the fluorescence process is shown: two vibrational levels, v′ and v″, and the rotational levels corresponding to the v′ vibrational level, are indicated.

Molecule	Band	min ν (cm^{-1})	max ν (cm^{-1})	$g_{v''v'}$ 10^{-5}(s^{-1})
C_2H_2	ν_3	3211.6	3358.3	19.09
C_2H_6	ν_7	2843.1	3159.3	60.21
CH_4	ν_3	2701.1	3277.6	35.93
CO	ν_1	1815.6	2316.0	22.28
NH_3	ν_1	3057.9	3565.1	3.32
HCN	ν_1	3159.0	3423.9	19.09

Table 2.1: Molecular fluorescence efficiencies for some vibrational bands of some important parent molecules in comets (G.L. Villanueva, private communication).

and $J(\nu_{ul})$ is the solar flux in the infrared at wavelength ν_{ul}. $J(\nu_{ul})$ can be described approximately by a blackbody of temperature $T_{bb} = 5770$ K; this approximation is valid for continuum flux around ≈ 3000 cm^{-1}, but could introduce important errors when computing pumping rates for individual lines; in this case, the solar Fraunhofer lines should be considered when the fluorescence efficiencies are calculated (see chapter 5).

The band excitation rate $g_{v''v'}$, which is the relative number of molecules undergoing vibrational v″ → v′ excitation through all possible $l \to u$ transitions within the (v″v′) bands at frequency $\nu_{v''v'}$, can be defined in a similar way (see for example Crovisier and Encrenaz (1983)).

The spontaneous emission rates A_{ul}, needed to retrieve individual excitation rates g_{ul}, can be derived in laboratory (see for example HITRAN (Rothman et al., 2009) or GEISA (Jacquinet-Husson et al., 2008) database), or can be calculated using full quantum mechanical models. These models require the computation of the rotational structure for each vibrational level, and involve statistical weights, selection rules, perturbations and band emission rates, and in most of the cases they turn out quite difficult to develop (see chapter 5). Typical values for the Einstein coefficients for spontaneous emission are in the range $10 - 100$ s^{-1}, while typical band excitation rates measure few 10^{-4} s^{-1} (see Tab. 2.1).

Close to the nucleus surface, coma density can be as high as 10^{12} cm^{-3}, and optical depth effects should be considered: optically thick atmospheres can reduce both the amount of solar flux received by the molecules and the flux measured by the observer. In these cases, a radiative transfer treatment of molecular excitation should be used, but the resulting mathematical formulation is quite complicated to solve and usually the g-factors

are calculated treating the atmosphere as optically thin: in this approximation, an upper limit is derived for the fluorescence efficiency. Optical depth effects can usually be more important for abundant molecules (like for example H_2O or CO_2), or for comets that release a high amount of dust during the active phase (in this case the dust is the cause of opacity).

When the vibrational lines are optically thin, the observed infrared line fluxes for a ro-vibrational transition $l \to u$ can be expressed in function of the fluorescence rate as:

$$F_{ul} = \frac{\Omega}{4\pi} h\nu_{ul} g_{ul} \langle N \rangle .$$ (2.2)

Here, Ω is the solid angle corresponding to the field of view and $\langle N \rangle$ is the total molecular column density. It is possible to define, also in this case, the band flux, that is related to the total emission rate of the band $g_{v''v'}$.

Column densities and molecular production rates are directly related and they can be easily converted one into the other, if the spatial distribution of molecules is known. One of the mostly used model is the so called Haser model (Haser, 1957): it assumes that parent molecules sublimate uniformly from the nucleus surface and expand radially outward with constant velocities; in these approximations and for a circular aperture, if all the coma is inside the field of view of the instrument, the relation between column densities and production rates is simply given by:

$$\langle N \rangle = \frac{Q}{\mathrm{v}d},$$ (2.3)

where Q is the production rate, v the expanding velocity of the molecules and d is the aperture diameter. In the majority of the cases these approximations are not applicable, and more complex methods have to be used to relate column density to production rates (see section 5.2). When the atmosphere is optically thick but the g-factor are calculated in the approximation of optically thin atmosphere, the corresponding retrieved production rate will be underestimated.

2.1.2   Other excitation processes

Fluorescence of the fundamental bands due to solar radiation is the main process, but not the only one, through which cometary parent molecules emit lines in the infrared. Hereafter, other excitation mechanisms that can occur in the coma are described. These processes can contribute to the fluorescence emissions or quench them, but it is possible to demonstrate that in the infrared range they can be in first approximation neglected (Crovisier and Encrenaz, 1983).

Fluorescence due to electronic excitation is negligible. In fact, as stated before, electronic excitation in the UV leads mainly to photo-dissociation of the molecules rather than fluorescence. Moreover, owing to the relative weaker solar flux at UV wavelengths, the excitation rates of electronic bands are small compared to vibrational excitation rates.

Non resonant fluorescence is also possible but, due to the low temperature in the coma, high energy vibrational levels are not expected to be significantly populated, and also in this case the strength of the possible bands is quite small compared to the ones of fundamental bands; anyway the contribution of these bands should be considered in second approximation.

In some cases collisional excitation can be important: if collisions are frequent, they can excite and maintain molecules in higher rotational/vibrational levels: this translates in a delay of de-excitation, i.e to a quenching of the fluorescence. Collisions are important especially for pure rotational transitions, in the radio region; for the other wavelength ranges, owing to the low temperatures throughout the inner coma, they do not significantly populate neither the vibrational nor the electronic levels of molecules, and the steady state vibrational and electronic population distributions are determined only by the radiative processes.

Continuous absorption by dust can also be neglected since this effect is only significant near the surface of the nucleus. Excitation due to dust thermal emission can be important in the inner coma of active comets for vibrational bands at wavelengths $\lambda \geq 6.7\ \mu$m (see Crovisier and Encrenaz (1983)).

2.2   High resolution spectroscopy in the infrared

The study of molecules in the gas phase will greatly benefit from the highest possible spectral resolution (Crovisier, 1989): emission lines in the gas phase are distinct and narrow, and it is important to resolve the rotational structure within a vibrational level (see Fig. 2.6) because a detailed comparison between the observed rotational structure and the modeled one can give important clues on the excitation conditions, especially regarding the kinetic temperatures and the ground level populations.

High resolution is needed to avoid possible unambiguous detections in case of spectrally confused regions: in fact, in the same spectral interval it is possible to find vibrational infrared signatures of particular vibrational modes of different molecules. This happens, for example, for the O-H, C-H and C-O bonds, at about 2.8 μm, 3.3 μm and 4.3 μm, respectively. Moreover, rotational lines of isotopes of the same species are quite close to each other in the spectrum (see Fig. 2.4), and it is possible to distinguish them only using the appropriate resolution.

One of the biggest problem that concerns ground based observations is the presence of the terrestrial atmosphere. Depending on its wavelength, the light coming from a celestial source can be absorbed completely, or partially, by molecules present in the terrestrial atmosphere (see Fig. 2.7); moreover, the same molecules can re-emit the absorbed light at various wavelengths and contaminate the light coming from the target. Since comets are moving objects, cometary lines are Doppler shifted with respect to the atmospheric ones and with respect to telluric features, and then they can be partially observed through atmospheric windows. Anyway the shift can be resolved only if the resolution of the used instrument is high enough (see section 4.2.3).

Finally, it is fundamental to reach a high signal to noise ratio: gas outflow speeds in the coma are low (typically 1 km/s) and cometary lines cannot be resolved by near infrared array spectrometers, but to increase the resolving power corresponds to increase the line to continuum contrast, that translates in a better detection of the single lines with respect to the thermal background.

High resolution spectroscopy in the mid-infrared is a relatively recent developed technique in astronomy and for this reason only a few instruments are available worldwide for ground based observations. One of the best way to reach high resolution is to use an
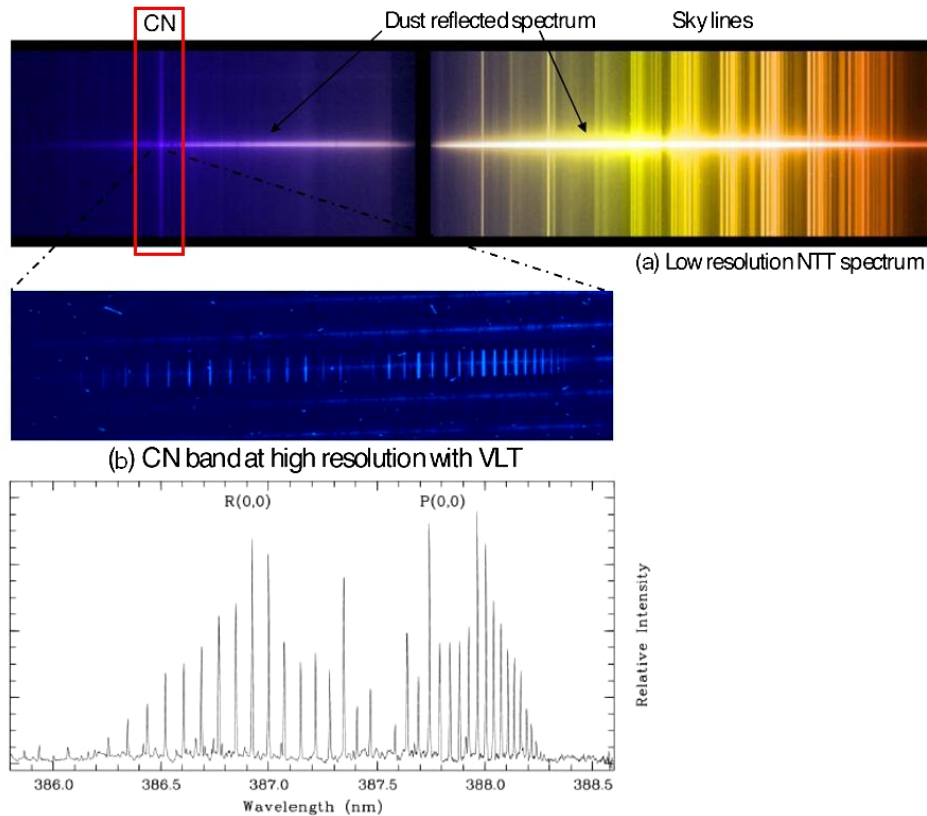
Figure 2.6: Comparison between low resolution spectra (a panel) and high resolution spectra (B panel) of a comet. In the low resolution spectra it is possible to distinguish atmospheric emission lines plus one of the vibrational band of CN molecule (highlighted with a red box); in the low resolution spectra, it is not possible to identify the rotational structure of this molecule, resolved instead in the high resolution spectra (b panel). The lower plot shows the corresponding extracted spectra. (Spectra of comet Tempel 1, adapted from http://www.eso.org/public/events/astro-evt/DeepImpact/Impact/campaign.html).

Echelle grating spectrograph (see Appendix C); modern near infrared Echelle spectrometers feature sufficiently high spectral resolving powers (RP = $\lambda/\Delta\lambda > 10^4$) to measure intensities of individual rotational emission lines with high signal-to-noise. The comparison between the main characteristics of Echelle spectrometers that cover the spectral region between 2 and 5 μm, and that are available worldwide, is shown in table 2.2.

2.2.1 CRIRES at VLT

The data presented in this thesis where obtained using the CRyogenic InfraRed Echelle Spectrograph (CRIRES), situated at the Very Large Telescope (VLT), Unit 1 (Antu), in Atacama desert, Chile [4].

---

[4]The VLT is a four units optical, near- and mid-infrared telescope array. Each unit (named Antu (UT1), Kueyen (UT2), Melipal (UT3) and Yepun (UT4)) has a diameter of 8.2 m and it is equipped with different instruments. VLT was commissioned and built by the European Southern Observatory (ESO); see http://eso.org/public/teles-instr/vlt/ for more details.
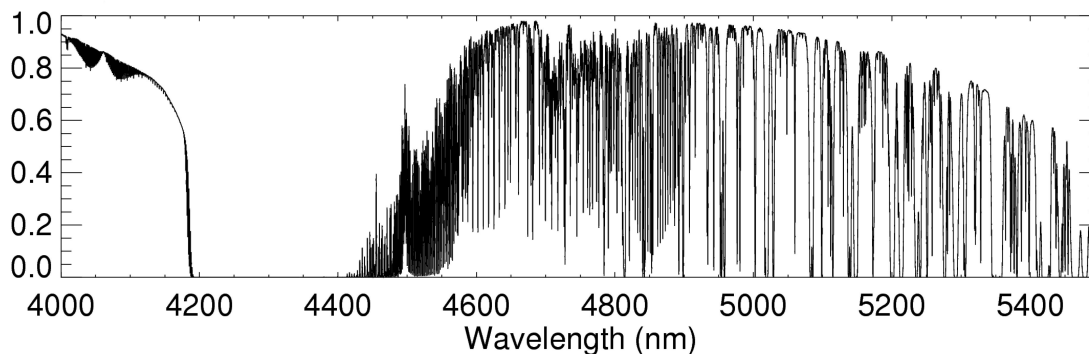
Figure 2.7:   Example of the transmittance spectrum of the Earth atmosphere between 4000 and 5500 nm; Doppler shifted cometary lines have to be detected among atmospheric lines.   In the plot, the value 0 is referred to completely opaque atmosphere, while 1 corresponds to transparent atmosphere.   (Source: CRIRES manual, http://www.eso.org/sci/facilities/paranal/instruments/crires/doc/VLT-MAN-ESO-14500-3486_v85.pdf).

Instrument and Telescope	Telescope Diameter (m)	Covered Wavelength Range (μm)	Resolving Power	Adaptive Optics
NIRSPEC Keck	10	$0.95 \div 5.5$	25000 $(0.43'')$	no
CRIRES VLT-UT1	8	$0.95 \div 5.2$	100000 $(0.2'')$ 50000 $(0.4'')$	yes
CSHELL NASA-IRTF	3	$1 \div 5.5$	30000 $(0.45'')$	no
SUBARU	8.2	$0.9 \div 5.6$	up to 20000 $(0.14'')$	yes

Table 2.2: Comparison between available worldwide telescopes equipped with an Echelle spectrograph, to perform high resolution spectroscopy, in the range 2 to 5 μm. For each telescope and instrument, the diameter of the telescope, the covered wavelength range and the resolving power (corresponding to the slit width indicated into brackets) are listed. Moreover, in the last column the presence or not of an adaptive optics system is indicated.

CRIRES provides high resolution spectroscopy in the spectral range between 1 and 5 μm range, employing the largest available grating for a spectral resolving power of up to 100000 (with a 0.2″ slit). It allows spatial analysis using a 40″ long slit, and it can be combined with an adaptive optics system that permits to reach high signal to noise ratios and high spatial resolution. A technical overview of the instrument is compiled in table 2.3. Functionally CRIRES can be divided into two main parts:

- **the cold part**: the cold part includes the spectrograph (box highlighted in gray, in figure 2.8), that is housed in the vacuum. Light entering the input window is sent first to a cold pupil stop that minimizes the total amount of background entering the high-resolution unit, and then to a pre-dispenser prism spectrometer that select part of the light. Light is then dispersed by an Echelle grating (40 x 20 cm, 31.6 lines/mm, 63.5 blaze Echelle grating) and detected by four Alladin detectors

Adaptive Optics	60-actuator curvature sensing MACAO
Slit Length	$\approx 40''$
Slit Width (variable)	$0.05'' - 3.0''$
Echelle Grating	40×20 cm, 31.6 lines/mm, 63.5 blaze angle
Resolving Power(slit width)	100000 (0.2''), 50000 (0.4'') Slit
Wavelength range	$0.95 \leq \lambda \leq 5.2\ \mu$m
Free Spectral range	from $\lambda/70$ at 1 μm to $\lambda/50$ at 5 μm
Detector Science Array	4096×512 pixels, Using 4 Aladdin III Detectors
Pixel Scale	0.086''(in the spatial direction)

Table 2.3: Technical overview of CRIRES (Source: CRIRES Manual, http://www.eso.org/sci/facilities/paranal/instruments/crires).
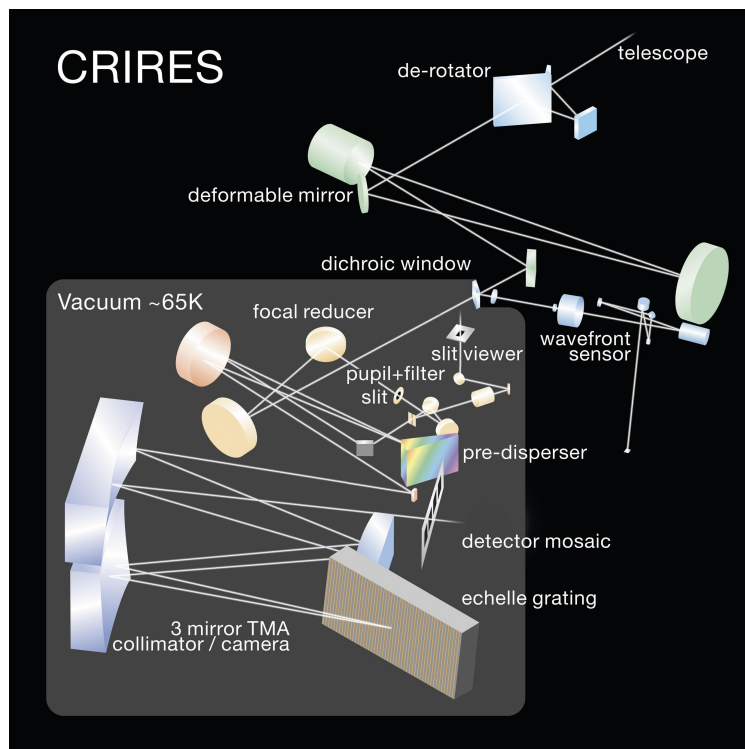
Figure 2.8: Overview of CRIRES optical design (Source: CRIRES Manual, http://www.eso.org/sci/facilities/paranal/instruments/crires).

forming a 4096 x 512 pixels array.

- **The warm part**: the warm part comprises the calibration units (that consist of an integrating sphere illuminated by continuum), halogen lamps for flat fielding, a gas cell for wavelength calibration, and the adaptive optics system. The turbulent wavefronts are corrected by a multi-application curvature optics system (MACAO) situated in front of the spectrograph, outside the cold box. In section 4.2.2, a brief description on how this system works and on the advantages that it can bring, is given.

There are few important differences between CRIRES and other high resolution spectrographs: CRIRES, in fact, can reach a very high spectral resolution compared to the
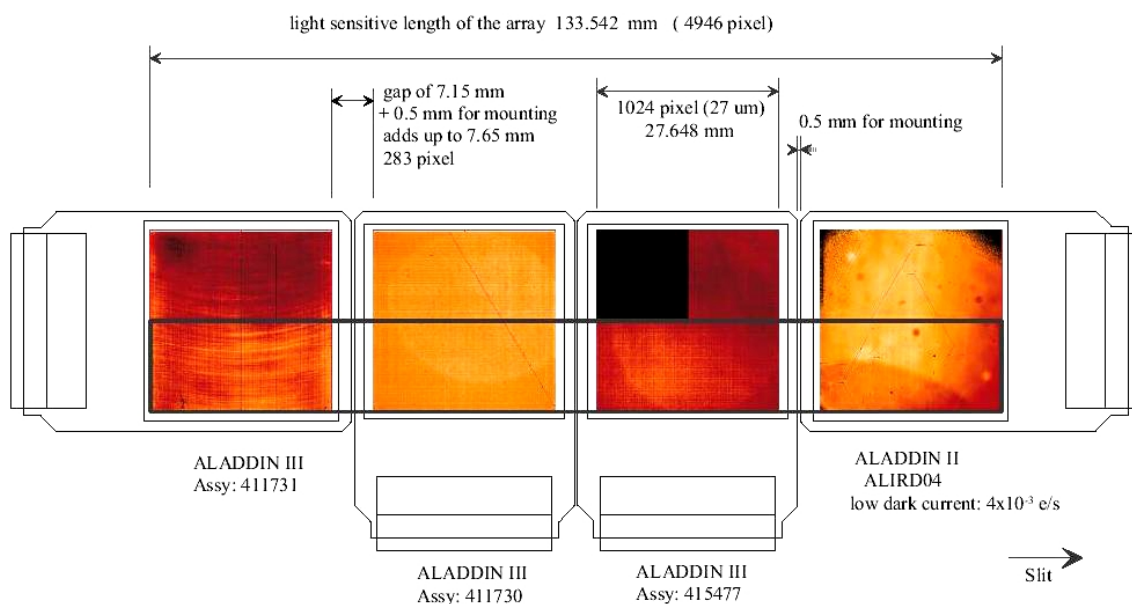
Figure 2.9: Layout of the mosaic of the four Aladdin detectors in CRIRES. Only the half-bottom part of each detector is used and is indicated by the thick black rectangle. It is possible to see the three gaps between the detectors. (Source: CRIRES manual, http://www.eso.org/sci/facilities/paranal/instruments/crires).

other IR spectrometers.

The large telescope aperture provides a narrower point spread function and thus a higher sensitivity, while the spatial resolution and the signal to noise ratio can be maximized by the optional use of the adaptive optics system, MACAO. This system corrects the distorted wavefront from a turbulent atmosphere, and provides significantly improved image quality (narrower PSF, see section 4.2.2).

An important point in cometary research is to try to observe different parent species simultaneously. If more than one species is observed at the same moment with the same instrument setting, systematic errors mainly related to seeing, flux calibration, and drift of the comet along the slit will be the same for every species, so that they will probably affect the determination of individual production rates but they will be canceled out upon determination of mixing ratios. Moreover, production rates vary during time along the cometary orbit: if a certain species is observed in a different day with respect to water, the corresponding mixing ratio could be affected by the temporal variations of both the production rates.

CRIRES lacks this possibility, since the order selection is provided by the pre-disperser prism, before the Echelle grating: in this way CRIRES is optimized for only one order and only few species can be detected simultaneously with the same instrument setting.

Another problem is related with the detector configuration: there is a gap between two neighboring detectors that corresponds approximately to 280 pixels (see Fig. 2.9). Some of the cometary emission lines could fall in the gaps between the detectors, so that the choice of the reference wavelength (that is centered in the middle of the third detector) is crucial to optimize the observations and thus the results.

Despite these last two considerations, CRIRES represents a unique instrument, and it

is the only one in the Southern hemisphere, that can provide the spectral resolution and sensitivity needed for the measurements proposed in this thesis.

More technical information regarding CRIRES can be found in the ESO web page: http://www.eso.org/sci/facilities/paranal/instruments/crires.

3   Motivations and goals of the thesis

In the last century the increasing capabilities of telescopes and instrumentation made it possible to improve the knowledge of cometary nuclei, especially including information regarding chemical composition and physical properties of comets. Nevertheless, still a lot of questions remain without a well defined answer:

- where did comets form, and which dynamical processes populated the two main cometary reservoirs, Oort cloud and Kuiper belt, during our Solar System history?

- Which is the chemical composition of a nucleus and which are the difference in composition, if any, among comets?

- Are dynamical and chemical properties somehow related?

- How pristine is the cometary material? Which are the processes that can transform the cometary material on the surface of a nucleus, and at which level the chemical composition observed in the coma is representative of the whole nucleus composition?

- What is the role that comets had during the formation of our Solar System? And had they played a role also in delivering water and prebiotics to Earth?

The work presented in this thesis intends to describe how it is possible to use high resolution spectroscopy in the infrared as a technique to study the chemical composition of cometary nuclei, and how these results can be used to increase the knowledge that we have on comets; in particular, with the observations of comets 8P/Tuttle and C/2007 W1 (Boattini) performed using CRIRES at VLT, we wanted:

- to detect, in the cometary spectra, emission lines produced by fluorescence of parent molecules, specifically H_2O, CO, CH_4, C_2H_6, C_2H_2, HCN, CH_3OH, H_2CO, and to search for signatures of yet unknown ices;

- to retrieve chemical and physical parameters for each detected species, like molecular production rates, mixing ratios with respect to water molecule and rotational temperatures, using suitable molecular models;

- to support and test theoretical modeling studies of the nucleus (among them the ones developed by Dina Prialnik and her group, at the department of Geophysics and Planetary Sciences, Tel Aviv University), providing realistic values for the initial needed parameters, like temperatures and mixing ratios;

- to obtain a global picture of cometary properties comparing the results obtained for the two observed comets with the ones already present in the literature.

4 IR observations and data reduction

This chapter is dedicated to the description of the steps needed to perform the observations in the best possible way, and to reduce the obtained raw data in order to retrieve line fluxes relative to molecular emission lines in the coma.

4.1 Planning the observations

4.1.1 Selection of the targets

The observed targets were selected, among other bright comets ($m_v > 9$), considering the nightly visibility window and the velocity of the comet with respect to the Earth (see section 4.2.3); if we assume insolation limited production rates ($Q_i \propto r_h^{-2}$, where r_h is the heliocentric distance, in AU), the intensity of the spectral lines relative to a certain parent specie i, is assumed to scale as the **figure of merit** (FM), defined as:

$$\text{FM} = Q(r_h)_{H_2O} 10^{-29} r_h^{-1.5} \Delta^{-1}, \tag{4.1}$$

where Δ is the geocentric distance, in AU, $Q(r_h)_{\text{H}_2\text{O}}$, in molecules s^{-1}, is the expected water production rate at r_h, and 10^{29} is a normalization factor; the FM is then a dimensionless index for the expected flux of cometary gaseous emission collected by a slit width with a fixed size, and therefore, larger FMs indicate better conditions for the observations. For the considered comets, the FM can be calculated and compared to other FMs, relative to already observed comets, and it can help to determine very approximate expected flux levels for various species. Usually the FM is retrieved for the water molecule, since this is the most abundant specie in the nucleus, and the main activity driver for heliocentric distances < 3 AU.

In case the water production rate at r_h is not know, it is possible to calculate the FM assuming a certain production rate at 1 AU. In this case, the exponent for the heliocentric distance in the 4.1 should scale as $r_h^{-3.5}$ (an additive r_h^{-2} factor is needed to properly scale the production rate).

The evaluation of the FM gives also hints for the best observational strategy and for the evaluation of the best exposure times to use. In table 4.1, FMs for the observed comets are listed and compared to others; in figure 4.1 an example of FM is plotted, together with the visibility of the target and the Doppler shift.
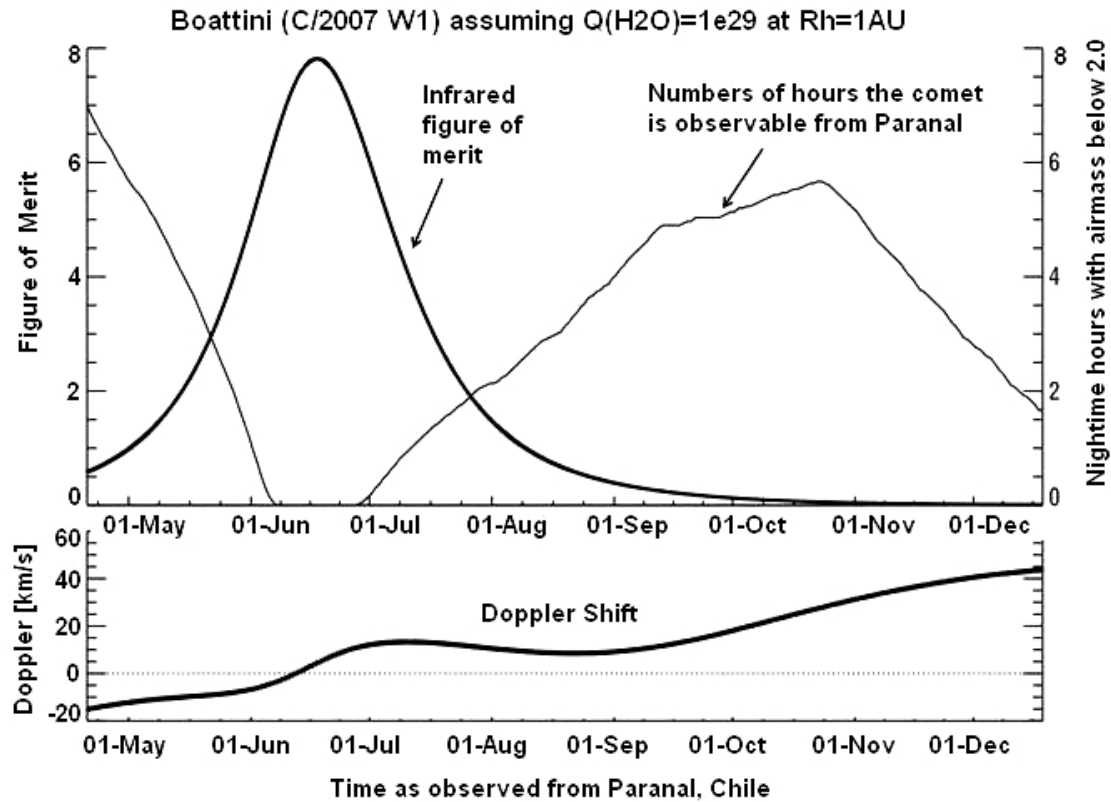
Figure 4.1: Figure of merit and visibility window plot, as obtained for comet C/2007 W1 (Boattini), during the preparation of the relative observing run. The Doppler shift of the comet is also shown.

Comet	Date	r_h (AU)	Δ (AU)	$Q(r_h)_{H_2O}$ (10^{29} mol/s)	FM
8P/Tuttle	January 2008	1.027	0.509	0.597	1.13
C/2007 W1 Boattini	May 2008	1.0	0.26	0.065	0.25
C/1996 B2 Hyakutake	March 1996	1.06	0.106	2.5	22
C/1995 O1 Hale Bopp	April 1997	0.918	1.40	107	87
C/2001 A2 LINEAR	July 2001	1.16	0.275	2.5	0.3
153P/Ikeya-Zhang	April 2002	1.0	0.40	2.5	6.0
C/2004 Q2 Machholz	January 2005	1.2	0.35	2.5	7.0

Table 4.1: Figures of merit for the observed comets, calculated as in equation 4.1 and compared to the ones measured for other comets. Note that for comet C/2007 W1 (Boattini) the FOM in the table differs from the one shown in Fig. 4.1, because the former was calculated assuming a production rate of 10^{29} mol/s at $r_h = 1$ AU, while the latter was computed using the retrieved production rate.

4.1.2   Observing runs preparation

CRIRES is set up according to the content of observing blocks (OBs) that contain all the information necessary for the execution of the observations, and that are prepared in advance using the specific tools offered by ESO. In particular for the preparation
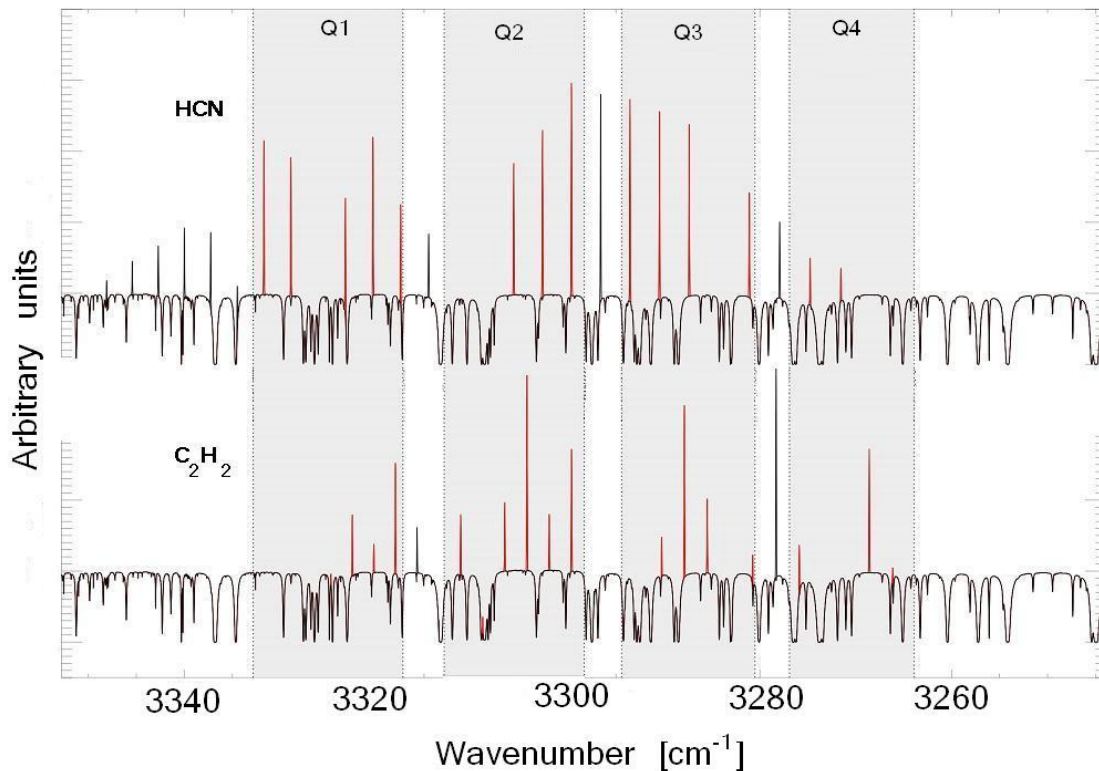
Figure 4.2: Schematic representation of the expected cometary fluxes for two molecules, HCN and C_2H_2, measured with the wavelength setting centered at ≈ 3033 nm (each of CRIRES detectors, Qi, is highlighted by a gray stripe). With this choice it will be possible to observe strong emission lines from both the molecules using only one instrument wavelength setting, even if some of the lines will fall anyway in the gaps between the detectors.

of the OBs we made use of the phase II proposal preparation tool, p2pp, available at http://www.eso.org/sci/observing/phase2/P2PP/P2PPTool.html, and of the exposure time calculator, ETC, available at http://www.eso.org/observing/etc/bin/gen/form?INS.NAME =CRIRES+INS.MODE=swspectr.

Wavelength settings have been chosen carefully to optimize the spectral coverage for each molecule, to take in account the Doppler shift due to the comet-Earth relative velocity, and to avoid at the same time that important and strong lines could fall in the gaps of the instrument, even if unfortunately this last point could not be always satisfied (see Fig. 4.2); these settings are listed, individually for each observed comet, in chapter 6.

Suitable integration times need to be used to avoid the saturation of the frames by the thermal background produced by the telescope and the atmosphere; used integration times will be listed, case by case, in chapter 6.

For each comet, a flux standard star have been observed and used to calibrate in flux the cometary data (see section 4.3.3); to have a reliable calibration, the star has to be observed during the same night and using the same wavelength settings of the comet; moreover, since it is important to know the magnitude of this star in the wavelength range of the observations, when possible, it is better to select stars for which the magnitude is quite constant over a wide range of wavelengths (A or B type stars).
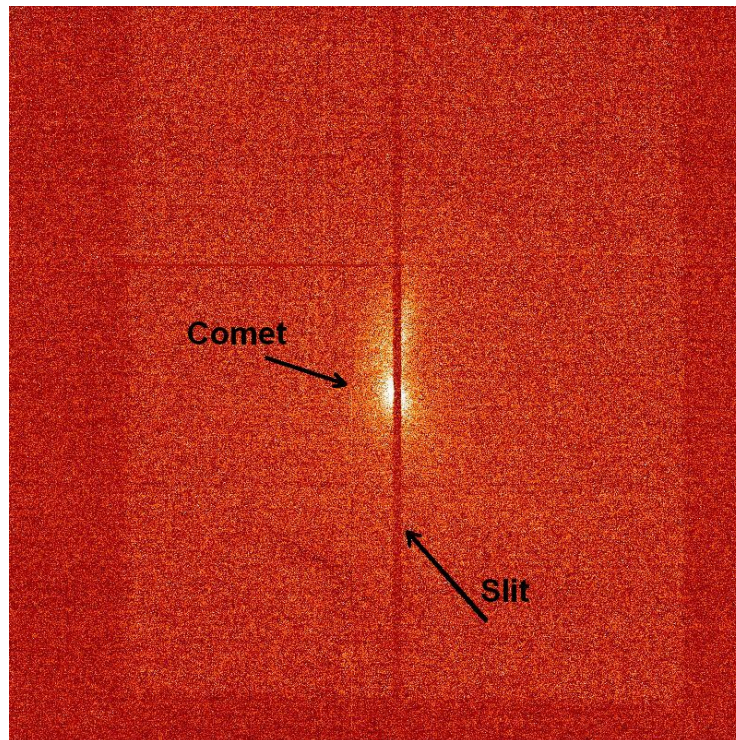
Figure 4.3: Acquisition image of comet 8P/Tuttle, taken in the K band, on January 26th, 2008. The bright spot inside the slit (the faint darker vertical line) is the comet.

4.2   Observations performed with CRIRES at VLT

4.2.1   Data acquisition: the nodding and jittering technique

The first step of the observations is the acquisition of the target. Even if the comet is observed in L, L' and M bands, the acquisition for CRIRES is done in J, H or K bands, where the object is brighter with respect to the background; the aim of the acquisition is to make sure that the target is centered in the slit for the wavelengths for which a spectrum must be obtained. All the targets were observed in "elevation mode", so that the slit is constantly aligned with the parallactic angle, along the atmospheric refraction direction. This is important since differential refraction could cause the comet to be centered in the slit for the acquisition, but off the slit for the observations, but at the same time in this configuration, the slit can slices through different parts of the comet during the same observing night and the corresponding measured spectra may be less comparable, due to possible space variability.

In figure 4.3 an example of an acquisition frame, as obtained from CRIRES, is shown; except for very bright comets, the resulting signal of the comet on the detector is usually weak and hidden by the dominant background radiation of the atmosphere and by atmospheric sky emission lines (see Fig. 4.5, panel A).

Atmosphere, telescope and instrumentation emit in the IR and they constitute a high level spatially rather uniform source of noise background; in addition, different pixels across the detector will be characterized by different quantum efficiencies and bad pixels will be present. The preprocessing techniques used to remove the thermal background and
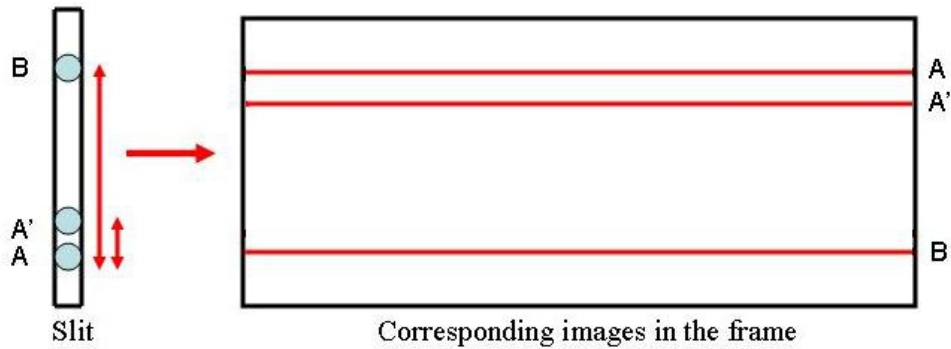
Figure 4.4: Example of nodding plus jittering technique: on the left side, the comet is represented as a light blue circle in the slit, in the positions A, A' and B. On the right side, the spectra corresponding to the mentioned positions are represented by a red line on the detector.

other systematic effects that can affect in the same way all the frames, will be described hereafter, while the operations applied to correct the inhomogeneities due to different sensitivity of pixels will be described in section 4.3.

To override the problem of the thermal background emission, for each wavelength setting exposures of the comet are taken in different positions of the slit, and then recombined together, after being reduced, as it follows (see Fig. 4.4): first an image in the position A of the slit is taken, that will correspond to a spectrum in position A on the detector. Then the telescope is moved such that the comet will fall on the slit at position B, that will correspond to the shift of the spectrum to position B on the detector.

A and B spectra are acquired using the same integration time to obtain the same background levels for each frame: in this way, the successive subtraction between two different frames (A-B) will cancel the high level background but not the signal, and cometary continuum dust emission and molecular emission lines will become visible (see Fig. 4.5, panel B). With this operation, also other systematic effects that occur for each frame, as for example bias and dark current (see section 4.3), will be removed.

Since thermal inhomogeneities affect the atmosphere, the thermal background will change during time[1], from frame to frame, and residual telluric absorption lines will be still visible after the (A-B) subtraction. This residual artifacts can be cleaned, using median filtering, during the first processing steps of the data.

The A and the B beams correspond to two **nodding** positions of the telescope; to maximize observing efficiency, this procedure is repeated for a certain numbers of times, ABBA cycles, and, through a particular combination of the resulting frames (see section 4.3), it (ideally) cancels the thermal sky and telescope emissions.

A small and random offset in slit direction is added to the nodding, for every ABBA cycle, ; this small additional shift is called **jittering**. If δ_i are the random jittering values, a typical observing sequence will then be (A - B - B - A' - A' - B' - B' - A"..., with A'=A+δ_1, A"=A+δ_2, B'=B+δ_3). The jittering permits to avoid that the cometary signal falls always

---

[1]The timescale over which atmospheric variations are frozen is called coherence time, and it is given by r_0/v, where v is the characteristic wind speed in m/s and r_0 is the so called Fried parameter (see section 4.2.2).
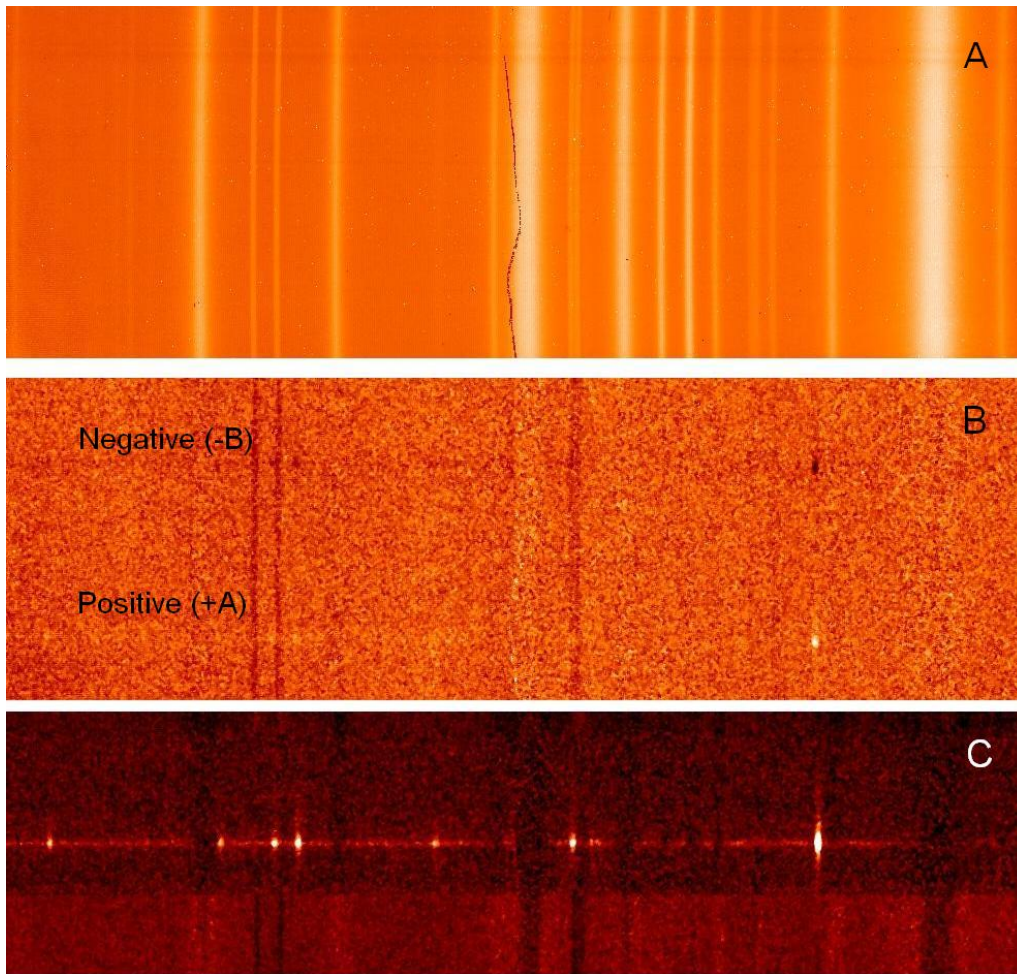
Figure 4.5: Panel A shows a single cometary raw spectrum as obtained with CRIRES during 8P/Tuttle observations on January 26th, 2008, using the 2.9 μm setting. In panel B the difference between two single frames (A-B) is presented: some emission lines are clearly visible, superimposed on a residual atmospheric signal. Panel C shows the frame as it appears when more frames are combined together, after being reduced as described in section 4.3.

in the same pixels of the detector: in this way, if the signal falls in a bad pixel for one frame, it will no do the same for the others, and thus the presence of bad pixels will not interfere much with our measurements. The nodding amplitude along the slit cannot be too small, or the emission lines will be partially deleted in the (A-B) subtraction. In our case, depending on the target, we used different nodding and jittering values. The main reason was related to technical problems with CRIRES, during observations of comet C/2007 W1 (Boattini): in this observing period we were, in fact, obliged to use a smaller area of the detector; the used values are listed, case by case, in chapter 6.

4.2.2   The effect of adaptive optics on the observations

Theoretically, the light distribution in an image of a point source, produced by a telescope with diameter D, is described by the Airy function, whose full width at half maximum (FWHM) is related to the ratio λ/D, with λ as the observing wavelength; the theoretical
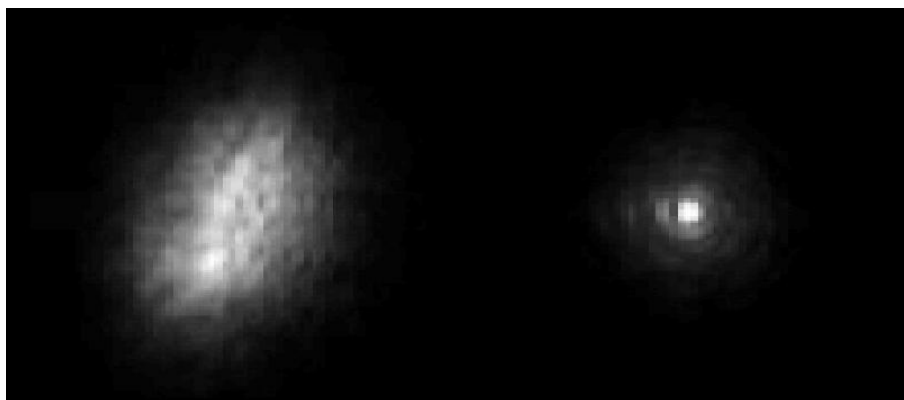
Figure 4.6: Observation of a star without (left panel) and with AO correction (right panel). (Source: CRIRES Manual, http://www.eso.org/sci/facilities/paranal/instruments/crires).

diffraction limit for the VLT ($D = 8.2$ m) is 0.07 arcsec at $\lambda = 2.2$ μm.

In reality, the presence of atmospheric turbulences, due to temperature inhomogeneities and temporal and spatial fluctuations in the air refractive index, produces a distortion of the wavefront of the incoming light. This leads to random phase delays that corrugate the wavefront (WF).

The FWHM of the retrieved images will be then related to the ratio λ/r_0, where r_0 is the so called Fried parameter: this parameter is directly linked to the strength of the turbulence and depends on the wavelength as $\lambda^{6/5}$. For average observing conditions at VLT, r_0 is typically 60 cm at 2.2 μm.

This translates in the fact that the FWHM for a real image is much bigger than the theoretical one, and thus the light coming from an astronomical source spreads over a bigger area of the detector, with the consequent decreasing of S/N and sensitivity in the measurements.

The adaptive optics technique was developed to overcome the degrading effects of atmospheric turbulence: a wavefront sensor (WFS) measures the distortions introduced by the atmosphere and sends this information to a deformable mirror (DM), that can be shaped in such a way to compensate the WF distortions. In this way, images quite close to the diffraction limit can be obtained.

As explained in chapter 2, one of CRIRES's assets is the presence of an adaptive optics system. To highlight the advantage of combining adaptive optics (AO) with CRIRES, a point spread function (PSF) is shown in figure 4.6, as it would appear in AO open loop (uncorrected) and AO closed loop (corrected) observations.

It is clear that in AO closed loop the S/N ratio in the central peak increases, and therefore higher resolution is achieved. Anyway, it is important to keep in mind that the performance of an AO system is also linked to the seeing at the moment of the observations, and to the brightness of the reference source used for the WFS measurement. Moreover, the quality of the correction depends on the distance between the reference source and the object of interest. In case of good conditions and a bright nearby reference source, the correction is good and the resulting PSF is very close to the diffraction limit. Our observations were performed in closed loop using the target itself for the WFS measurements.

4.2.3   The terrestrial atmospheric transmittance and the importance of the Doppler shift

The Earth's atmosphere is composed mainly of O_2 and N_2, and, in a lower amount, by other constituents like $CO_2, CO, CH_4, H_2O, N_2O$; these minor different gas species, that are not necessarily uniformly mixed and whose proportions can vary as a function of the temperature and of the height above the sea level, play an important role in IR observations, since they can absorb totally or partially the light coming from the celestial source, affecting the signal received at the telescope.

Molecules like H_2O, CO and CH_4 are characterized by strong counterparts in the Earth atmosphere: these molecules can be detected only if the telluric band is not too large, and if the comet provides a sufficiently high Doppler shift relative to the observing site on Earth, so that the cometary lines can be identified in the wings of the corresponding atmospheric absorption bands; considering CRIRES, for a resolution of 50000 (with a 0.4″ slit width), this translates in a relative radial velocity of $v_{com} \gtrless 6$ km/s; a favorable comet-Earth Doppler shift can also help to distinguish the cometary emission lines among all the possible emission lines due to the molecules present in the Earth's atmosphere.

Cometary H_2O emission lines are detectable only trough non resonant fluorescence vibrational bands, since the fundamental bands are completely absorbed by the terrestrial atmosphere, but the presence of numerous telluric water lines, mostly associated with the fundamental bands, increases the chance of extinction due to coincidental overlap with an unassociated telluric feature. This is also the case of molecules like C_2H_6, C_2H_2 or HCN: these molecules do not have, or have a weak telluric counterpart in the atmosphere, but their emission lines fall in the absorption bands produced by other molecules, and in particular by water. In all these cases, the number of detectable lines benefits not only from a suitable Doppler shift, but also from a low H_2O vapor content in the Earth atmosphere.

Corrections for telluric absorptions are done using synthetic transmittance spectra based on a rigorous line by line and layer by layer radiative transfer modeling of the terrestrial atmosphere (like, for example, GENLN2 model, see Edwards (1992)).

4.3   Reduction of the data after observations

What follows is a description of the procedures that were used to retrieve our results. Part of these procedures are in standard use in astronomy, while specific algorithms have been developed by the astrobiology group leaded by Michael J. Mumma, at Goddard Space Flight Center, and have been tailored specifically to CRIRES. The same data reduction steps are described also in Bonev (2005).

4.3.1   Basic processing steps

The raw data needs some basic reduction before it is possible to retrieve the production rates. As mentioned in section 4.2.1, a certain number of frames is collected using the nodding plus jittering technique; each frame, that initially measures 1024 x 512 pixels, is reduced selecting only the part of interest; the new dimensions will be the same for all the

A and B frames, and each frame will be reduced separately from the others.

- **Dark current**: in general, a detector can measure a signal even if no sources are observed: this signal is caused by the dark current, a relatively small electric current existing even when the signal is absent. The dark current is usually very stable and it can be reduced decreasing the temperature of the detector. In general, the correction of the dark current effects is done by subtracting a "dark frame" from the science frame; the dark frame is obtained avoiding exposure of the detector to any kind of light, and using the same exposure time and the same instrument setup used for the science frame. When the nodding and jittering technique is used, the subtraction of the dark current, that is the same for every frame, is automatically done through the operation (A-B); with this operation also other possible systematic noise effects are deleted.

- **Flat field**: the response of the pixels to the signal in a detector is not uniform and a "flat-field" correction, to improve the quality of the results, is needed. This correction requires a particular exposure, the flat, obtained illuminating homogeneously the detector. Since the flat frame is subject to dark current, it is necessary to subtract a dark frame from it. The pixel-to-pixel sensitivity variations of the detector will be then removed from the science frame dividing it by the (flat-dark) frame. Flats and darks should have the same integration time, and the flat should be taken with the same slit width and the same wavelength setting used for the science frame. After changing the instrument settings, the original grating position cannot be reproduced exactly: if moved, the difference between the positions of one setting used for the comet and the same setting used for the flat would be very small, but sometimes enough to introduce artifacts like non-properly removed fringe patterns upon flat-field correction; practically, as in the case of data presented in this thesis, this rule is not followed and flats are usually taken at the end of each observing run, sometimes with a different slit width.

- **Cleaning**: cosmic rays and bad pixels are identified and removed from the raw frames using standard sigma filtering. For an (A, B, B, A') sequence, cosmic rays are also identified in the (A-A') and (B-B) frames; a mask reproducing the cosmic rays pixel location is created and then applied to AB pairs ((AB), (A'B), ...).

4.3.2 Spatial and spectral alignment of the frames and spectral calibration

Due to optical aberrations and small alignment errors of the optics, the spectra appear tilted and curved on the detector (see Fig. 4.7): for this reason the frames need to be "registered" in both spectral and spatial dimensions, so that in the final combined frame the spectral dimension falls along the rows while the spatial dimension falls along the columns.

- **Spectral registration**: for each beam, a Gaussian function is fitted column by column to the continuum of the signal. The resulting peak rows are fit with the corresponding column pixel number via a second order polynomial. This fit approximates the tilt of the analyzed half of the frame, and eventually a possible curvature,
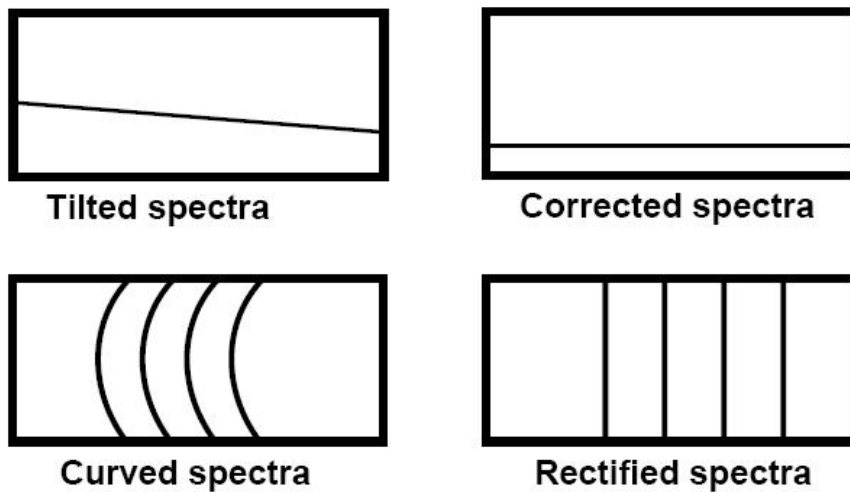
Figure 4.7: Optical (overestimated) aberrations scheme. Tilt and curvature of the spectra are caused by the instrument, and need to be corrected.

along the spectral direction. The resampling procedure essentially takes this dependence out of the data, so that the spectral dimension falls exactly along the rows of the 2D arrays. If the continuum of the comet is not really strong, which happened quite often for our objects, frames of the comet are cropped and cleaned exactly as the one of the star. In this way the resulting parameters obtained for the spectral registration of the standard star can be used reliably for the spectra resampling of the comet.

- **Frequency calibration**: sky emission lines are, in most cases, the strongest signal in the frames. They can be used as a calibrator instead to use an arc-lamp, that usually does not present enough lines to perform a good calibration. A synthetic atmospheric spectrum is created (using the GENLN2 model, see Edwards (1992)) and fitted with the data: in this way each line of the frame can be spectrally registered and calibrated in frequency. The adopted relation between column pixel number x and wavenumber ν is:

$$\nu(x) = \nu_{(\mathrm{cent})} + \mathrm{disp}_1 \times |x - x_0| + \mathrm{disp}_2 \times |x - x_0|^2 \,, \qquad (4.2)$$

where x_0 is the central pixel in the frame and disp_1 and disp_2 are the first and second order dispersion terms. Varying disp_1 and disp_2 corresponds to stretching or to shortening the frame spectra with respect the synthetic spectra in spectral direction to find the better match between the two; this is not an exact functional relationship, but just an approximation, which however leads to an adequate straightening of the sky lines. The fit is only in frequency, not in intensity space, since in principle an exact match in intensity is not strictly required for frequency calibration purposes; it is preferable to calculate the dispersion terms stacking all the frames together before to apply the procedure, since the resulting frame will have a better signal to noise ratio for the object. The calculated dispersion terms can be then applied to the single frames. To refine the calibration, a residual analysis can be done: the spectrum

extracted from the final combined frames is compared to the synthetic atmospheric spectrum and the dispersion terms are refined; in this way the straightening, the wavelength calibration and then the final results are improved.

- **Combining the frames**: the reduced and calibrated frames can be finally combined together. The subtraction (A-B) produces a frame in which a positive (A) plus a negative (B) spectra are present (see Fig. 4.5, panel B); the frames are combined together in such a way that the peak rows of the A beams and the ones of the inverted B beams coincide. In this way the S/N is higher and the residual sky signal can be better removed (see Fig. 4.5, panel C).

4.3.3   Flux calibration

In addition to the comet a standard IR flux star is always observed during the same night, with the same wavelength settings used for the comet. This star is needed, primarily, to calibrate the spectra in flux, but as seen before, in case of a faint continuum of the comet it can be used also to retrieve the parameters needed for the spectral and the spatial registrations.

Flux standard stars are selected depending on the target, from on-line catalogs (see for example http://www.iac.es/telescopes/tcs/estandares-eng.htm) which publish the flux standards magnitudes for a given IR band. The star is usually chosen to have a similar declination as the target, but to precede or trail it in right ascension by some hours, generally depending on whether the target comet is rising or setting. It is also desirable (though not strictly required) to use an early-type star because it would have a clean IR continuum, without absorption features. Frames of the standard stars are reduced using the same algorithms used for the comet.

The stellar flux at a given frequency is estimated in two steps: the published magnitude m for the effective center frequency ν_0 of a given IR band is converted to flux density units using the standard magnitude flux relation of Vega (α-Lyrae) as the zero magnitude reference:

$$f_{\text{star}}(\nu_0) = f_{\text{m=0}}(\nu_0) \times 10^{-0.4m}. \tag{4.3}$$

The flux density at the desired frequency $f_{\text{star}}(\nu)$ is derived from $f_{\text{star}}(\nu_0)$ via the Plank function at a temperature approximating the stellar spectral class (T_{star}):

$$f(\nu) = f(\nu_0)\frac{B_\nu(T_{\text{star}})}{B_{\nu_0}(T_{\text{star}})}. \tag{4.4}$$

The conversion factor Γ (measured in $\text{Wm}^{-2}(\text{cm}^{-1})^{-1}(\text{ADU/sec})^{-1}$) between directly measured instrumental counts per unit time at a certain frequency and their corresponding flux density is obtained from the following relation:

$$\Gamma = \frac{f_{\text{star}}(\nu)}{\text{counts}(\nu)/t}\frac{\tau_\nu}{F_{\text{cor}}}, \tag{4.5}$$

where counts is the detector photon counts in ADU, $f_{\text{star}}(\nu)$ is the predicted flux density for the observed IR flux standard star at frequency ν (cm^{-1}), τ_ν is the atmospheric transmittance and t the integration time in seconds. F_{cor} is the correction factor used to

compensate for slit losses, and it corresponds to the ratio between the predicted counts for an infinitely wide slit and the measured counts at the real slit; the predicted counts for an infinitely width slit are calculated assuming a stellar Gaussian profile.

The Γ factors are used to transform directly measured instrumental counts per unit time, at a certain frequency, in the corresponding flux density ($Wm^{-2}[cm^{-1}]^{-1}$). For CRIRES, Γ factors vary depending on the quadrants, and on the wavelength settings; these variations are probably related to instrumental effects or to not proper flat-fielding, and they are expected to affect in the same way both the comet and the calibration star data.

5 From fluxes to production rates: the HCN case

Molecular models that compute fluorescence emission efficiencies are necessary to convert measured line fluxes in comets, to molecular column densities. These models require the precise knowledge of the rotational structure for every vibrational level involved, statistical weights, selection rules, perturbations (e.g. Coriolis effects, splittings, tunneling), and band emission rates. The complexity of the task has limited the development of new models, in particular for those molecules having a complex symmetry structure, and consequently only a restricted set of line-by-line fluorescence emission models are currently available.

In this chapter we present the development of a model that describes the ν_1 vibrational transition of the HCN molecule, and the steps needed to retrieve the production rates from measured line intensities. The presented methodology can be adapted to other linear molecules and to more complex molecules, by including the necessary parameters and assumption.

5.1 A model for the ν_1 emission band of HCN

The hydrogen cyanide molecule

Hydrogen cyanide (HCN) is a linear molecule with a triple bond between carbon and nitrogen; in table 5.1 some of the properties of this molecule are listed.

Hydrogen cyanide represents a key intermediary for synthesis of biochemical compounds on Earth: HCN deposited by comets, meteorites and interplanetary dust particles, could have given rise to essential polymeric structures, and its presence in liquid water may have leaded to amino acid formation, to protein ancestors and then to life as we know it (Matthews and Minard, 2008). HCN is a known parent molecule in comets, and is also present in interstellar clouds. Its abundance relative to other nitrogen bearing molecules, like NH_3 or N_2, can indicate the formation temperature and the kind of degree of processing experienced by precometary material, whether in the natal cloud or in the solar nebula, while its spatial distribution in the coma may indicate the nature of its sources. Moreover its abundance can provide limits for production of the CN daughter species observed extensively at optical wavelengths.

HCN can vibrate in three normal vibration modes[1]: $C - H$ stretching mode (ν_1), that

---

[1]A normal mode is a collective motion of all the atoms in the molecule where each atom in the molecule moves in phase with each other at a particular frequency.
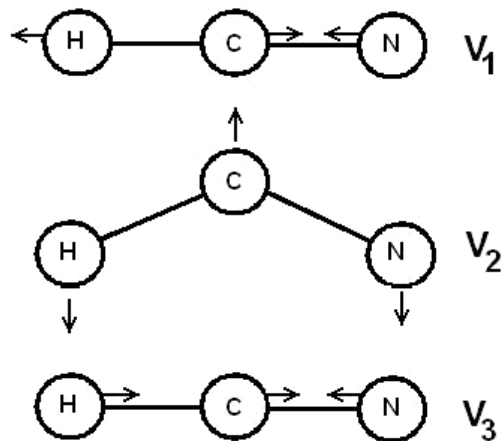
Figure 5.1: Schematic representation of the normal modes for the HCN molecule: $C - H$ stretching on the top, $H - C - N$ bending in the middle, $C - N$ stretching on the bottom.

$H - C \equiv N$	
Molecular Weight	27.03 amu
Boiling Temperature	299 K (at 1 Atm)
Freezing Temperature	260 K
Density	0.715 g/ml (at 273 K)
Dipole Moment	2.98 D

Table 5.1: Basic physical properties for the HCN molecule.

corresponds to an emission band around 3311 cm^{-1}, $C - N$ stretching mode (v_3) that corresponds to an emission band around 2097 cm^{-1}, and $H - C - N$ bending mode (v_2) that corresponds to an emission band around 712 cm^{-1} (see Fig. 5.1); in table 5.2 the band strengths relative to these modes are listed.

The rotational structure of the normal vibrational transition related to the $C - H$ stretching mode is described by a two components spectrum, a R-branch and a P-branch, so that it was possible to develop a simple model to fit to our data.

The model development can be summarized in:

- calculation of the rotational energy distribution of the two considered vibrational levels;

- calculation of the initial or equilibrium population, in the ground vibrational state.

- Pumping rates are calculated from all rotational levels in the ground vibrational state to the excited state, respecting the selection rules.

- Emissions from the excited to the equilibrium ground state are calculated, considering the correct rotational branching ratios.

Hereafter, these steps are described more in detail.

Mode	Frequency (cm^{-1})	Band Strength (cm^{-2}atm^{-1})
ν_1	3311	236.2 (at 296K)
ν_2	712	234 (at 300K)
ν_3	2097	0.1 (at 300K)

Table 5.2: Band strengths for the HCN normal modes (values from Rao and Mathews (1972)).

Constant	Value	Dimension	Ref
B_{low}	1.478221840	cm^{-1}	(Maki, 1996)
D_{low}	2.91047 10^{-6}	cm^{-2}	(Maki, 1996)
H_{low}	3.40 10^{-12}	cm^{-3}	(Maki, 1996)
B_{up}	1.4677983422	cm^{-1}	(Maki, 1996)
D_{up}	2.8856236 10^{-6}	cm^{-2}	(Maki, 1996)
H_{up}	3.6215 10^{-12}	cm^{-3}	(Maki, 1996)
ν_0	3311.476834	cm^{-1}	(Maki, 1996)
A_1	-0.001509119		(Malathy Devi et al., 2003)
h	6.626068 10^{-34}	J/s	
k	1.380650 10^{-23}	J/K	
k_e	6.955844 10^{-1}	cm^{-1}/K	
c	2.997324 10^{8}	m/s	
Q_v	1.0676		(Malathy Devi et al., 2003)
S_v	0.9062 10^{-17}	cm/molecule cm^{-2}	(Malathy Devi et al., 2003)
I_a	0.98511		(Šimečková et al., 2006)

Table 5.3: List of the constants used for the model.

5.1.1   Rotational levels and partition function

The first step to create the model consists in computing the possible energies of all the rotational levels within the two vibrational levels, for the considered transition. If we indicate with the subscripts low and up the quantities related to the lower and upper vibrational levels respectively, we can approximate the energies of the levels as:

$$
\begin{aligned}
E_{\text{low}} &= B_{\text{low}}J(J+1) - D_{\text{low}}J^2(J+1)^2 + H_{\text{low}}J^3(J+1)^3, \\
E_{\text{up}} &= B_{\text{up}}J(J+1) - D_{\text{up}}J^2(J+1)^2 + H_{\text{up}}J^3(J+1)^3,
\end{aligned}
\tag{5.1}
$$

where B_{low} and B_{up} are the rotational constants relative to the lower and upper vibrational levels respectively, and J is the rotational quantum number, that can take integer positive numbers ($J = 0, 1, 2, ...$); D_{low}, H_{low}, D_{up} and H_{up} are the second and third rotational constants for the second order and third order corrections respectively (see appendix B). Rotational structure of each vibrational level can be described in a more complex manner to include other perturbations, but these are negligible and we have restricted our analysis to three constants per vibrational level (see equation 5.1 and table 5.3). Retrieval of the rotational constants is achieved by performing highly precise spectral measurements of several ro-vibrational bands in the laboratory.

Knowledge of the initial population in the ground vibrational state is fundamental when computing the pumping rates into individual rotational levels in the upper vibrational state of interest.

The population of the levels is described by the partition function[2]. The total partition function for a molecule, can be represented by the product $Q_{\text{tot}} = Q_e Q_v Q_r$, where Q_e, Q_v and Q_r are the electronic, vibrational and rotational partition functions, respectively. In general, the computation of molecular total partition functions is particularly complex, requiring the complete knowledge of all electronic/vibrational/rotational modes, and not only of the two vibrational levels involved in a band-system. Anyway, since cometary atmospheres are particularly cold ($T < 200$ K), for most molecules only the lowest vibrational level is populated, meaning that the total partition function can be approximated to the rotational partition function of the lower state:

$$Q_r = \sum_J w_J e^{\left(\frac{-c_2 E_{\text{low}}^J}{T} \right)},$$
(5.3)

where E_{low}^J are the energies of the rotational levels in the lower vibrational state, T is the considered temperature, $c_2 = hc/k = 1.4388$ cm K; $w_J = (2J + 1)$ represents the degeneracy of the rotational level characterized by the rotational quantum number J.

5.1.2   Computation of fluorescence pumping factors and fluorescence efficiencies

Selection rules define which transitions are allowed among the rotational levels, and the structure of the resulting ro-vibrational spectra is directly connected with them. For diatomic and linear molecules in the lower state energy, dipole allowed transitions obey to the selection rule $J_{\text{up}} - J_{\text{low}} = \Delta J = \pm 1$, where J_{up} and J_{low} are the rotational quantum numbers of the involved rotational levels, upper and lower ones, respectively. This means that the considered vibrational transition band will present two branches: a P-branch for $\Delta J = -1$ and a R-branch for $\Delta J = +1$ (see Fig. 5.2).

The frequencies of the possible transitions are given by

$$\nu_J = E_{\text{up}}(J_{\text{up}}) - E_{\text{low}}(J_{\text{low}}) + \nu_0,$$
(5.4)

where ν_0 is the frequency of the pure vibrational transition, without taking account of rotations. The intensity of individual lines is directly proportional to the rotational population in the initial state of the molecule, that is given by the partition function; following Malathy Devi et al. (2003) we calculated the intensities of the rotational lines using:

$$S_J = \frac{\nu_J}{\nu_0} L_J \frac{S_v}{Q_r} e^{c_2 E_{\text{low}}/T} \left[1 - e^{c_2 \nu_J / T} \right] F,$$
(5.5)

---

[2]According to the Maxwell-Boltzmann distribution law, in thermal equilibrium the number of molecules N_n in a state of total energy E_n and of total statistical weight (degeneracy) w_n is proportional to $w_n e^{-E_n/kT}$, where k is the Boltzmann's constant and T is the absolute temperature in degrees Kelvin. The total number of atoms or molecules N in a given volume is therefore proportional to

$$Q = \sum w_n e^{-E_n/kT}.$$
(5.2)

The quantity Q is the partition function of the gas, and all thermodynamic quantities can be expressed in terms of it (Herzberg, 1939).
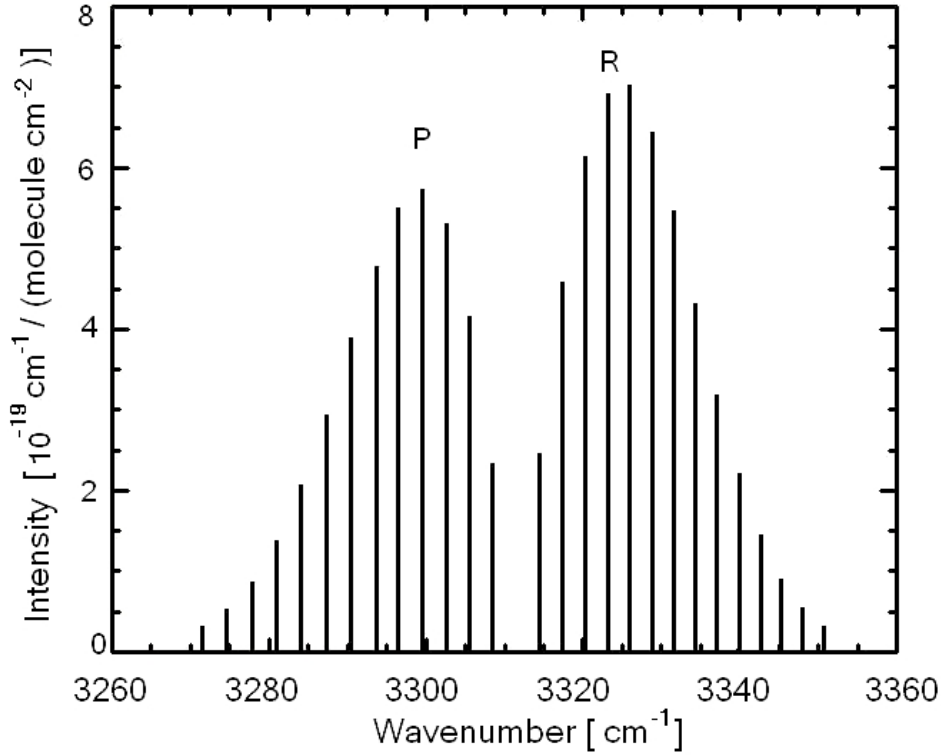
Figure 5.2: Structure of the HCN spectrum, generated with the developed model, assuming an initial temperature $T = 80$ K; P and R branch are indicated.

where S_ν is the vibrational band intensity, L_J is the rotational line intensity, or Hoenl-London factor, F is the non-rigid rotor factor, or Herman-Wallis factor; it can be demonstrate that for diatomic and linear molecules in the lower state energy, the Hoenl-London factor is given by $L = m^2/|m|$, with $m = J + 1$ for the R-branch and $m = -J$ for the P-branch, while the Hermann-Wallis factor can be approximated by $F = (1 + A_1 m)^2$, with m defined as before (see Herzberg (1939)). The parameters S_ν, A_1, and ν_0, are measured in the laboratory, and the values used for our model are listed in table 5.3.

Computation of cometary pumping g-factors requires the knowledge of the Einstein coefficients for spontaneous emission, A_{ul}, and for absorption, B_{lu}. For each line, Einstein A coefficients can be calculated following Šimečková et al. (2006):

$$A_{ul} = \frac{8\pi c \nu^2 Q_r(T) S_J}{e^{-c_2 E_{\text{low}}/T}(1 - e^{-c_2 \nu/T}) I_a w_{\text{up}}}, \tag{5.6}$$

where I_a, listed in table 5.3, is the isotopic ratio for the HCN molecule, considered as a non pure gas. Einstein B coefficients are related to Einstein A coefficients by the simply relation $A_{ul} = 8\pi h\nu^3 B_{lu}$.

If J_ν is the solar flux at frequency ν, the total pumping g-factor is:

$$g_{\text{pump}} = \sum g_{lu} = \sum \frac{J_\nu B_{lu} w_{\text{low}} e^{-c_2 E_{\text{low}}/T}}{Q_r(T)}. \tag{5.7}$$

It is really important to use a realistic solar spectrum: the black body approximation
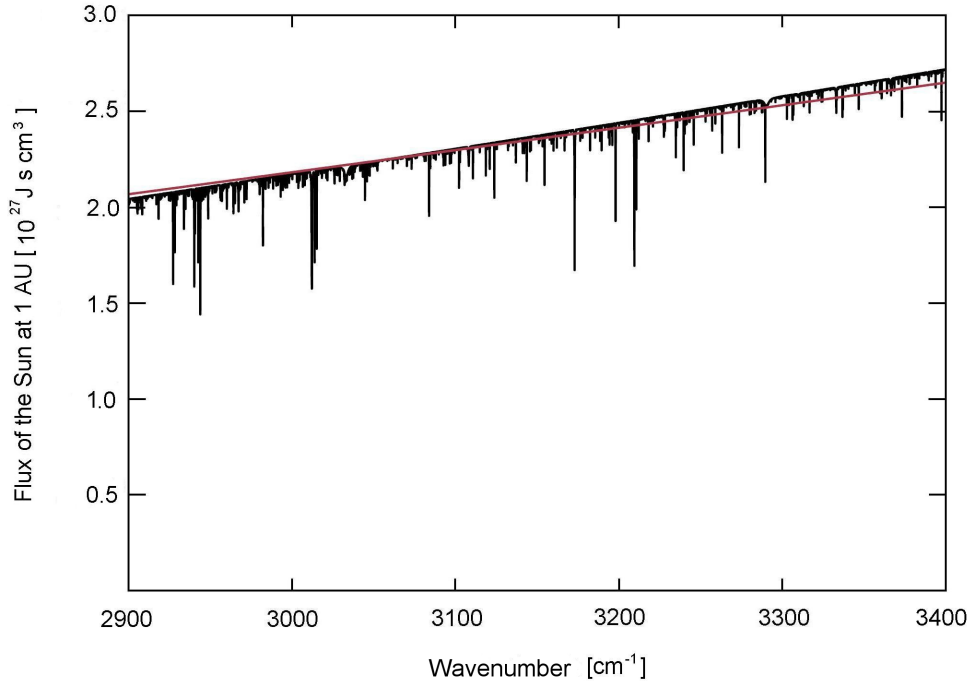
Figure 5.3: Comparison between the solar spectrum generated considering the Sun as a black-body (red line) and the solar spectrum generated as described in section 5.4, for the spectral region relevant for the HCN $- \nu_1$ transition.

is not correct for our purposes, since it can lead to wrong g-factor calculations (see Fig. 5.3); moreover the presence of Fraunhofer absorption lines in the solar spectrum requires the calculation of g-factors at the corresponding heliocentric velocity of the comet (see section 5.4).

Once all pump factors have been computed, the branching ratios for each line are simply calculated as A_{ul}/A_{tot}, where $A_{tot} = \sum A_{ul}$ is the sum of all probabilities accessing this ro-vibrational level. Finally, cometary fluorescence rates, i.e. the g-factors, are calculated as following:

$$g_{ul} = g_{pump} \frac{A_{ul}}{A_{tot}}. \tag{5.8}$$

5.2   Retrieving the production rates

After the reduction steps, the obtained two dimensional spectrum is extracted within 15 rows in the spatial direction ($\approx$ 1.29 arcsec), centered in the nucleus (± 7 pixel from the central bright peak)[3].

The modeled spectrum is spectrally shifted, affected by atmospheric extinction, convolved to the instrumental resolving power and ultimately compared to the extracted one. In this way, the lines produced by the HCN molecules can be identified among other lines

---

[3]This correspond to sample a radius of $\approx$ 233.90 km for comet 8P/Tuttle, observed in January 2008 ($\Delta \approx 0.5$ AU), and $\approx$ 140.34 km for comet Boattini, observed in May and July 2008 ($\Delta \approx 0.3$ AU).
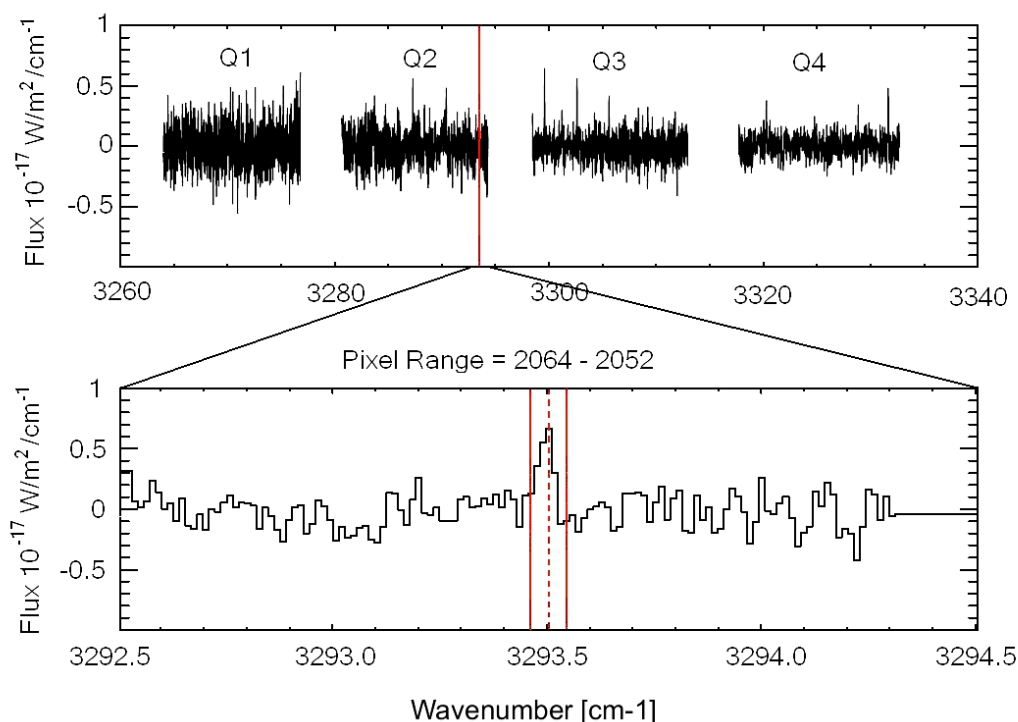
Figure 5.4: Identification of one of the HCN lines in the measured spectra. In the upper panel, all the four CRIRES quadrants are shown; the red line is drown for the Doppler shifted model line. In the lower panel an enlargement of the upper panel is shown. The dashed line represent the central wavelength from the model, while the lateral continuous line represent the limits used in the integration of the line.

produced by different molecules. For each line we measure the flux F_i, by integrating over nine spectral pixels (see Fig. 5.4), and we then divide the results by the (fully resolved) terrestrial transmittance at the exact Doppler shifted position of the cometary line, to obtain the corresponding fluxes at the top of the atmosphere.

The fluxes can now be converted into column densities, that represent the number of molecules in the field-of-view of the observation, and in production rates, i.e. the number of molecules released per second from the nucleus. As seen in chapter 2, if the whole coma can be covered in the field-of-view, and if resonance fluorescence is the main excitation mechanism, the column densities can be derived from the measured flux by the simple relation 2.2; this is usually the case, but for some emissions (e.g. hot-bands or prompt emission) other important considerations come into play.

5.2.1   The f(x) function and the Q-scale factor

For our computations, we assume that the production rate of a molecule is constant over its lifetime, and that molecules after being released, are distributed with a spherical symmetry in the coma. Moreover we assume that the outflow velocity from the nucleus is constant. These assumptions are usually acceptable, except for special cases like the Deep impact

event or natural outbursts when time variability on a very short time scale characterizes the outflow and the production of the gas.

With the above assumptions, if we observe the nucleus with a circular diaphragm s, the emission line flux integrated over the band from molecules having sublimation rate Q is given by

$$F_i = \frac{g_i Q \tau f(x)}{4\pi\Delta^2},\tag{5.9}$$

where Δ is the geocentric distance, τ is the photo dissociation lifetime of the considered molecule, g is the fluorescence efficiency and $x = s/\gamma$; γ represents the scale length, defined as $\gamma = \mathrm{v}\tau$, where $\mathrm{v} = 0.8r_h^{-0.5}$ is the velocity in km/s and τ is the lifetime in seconds of the considered parent molecule (we use a value of $1.75\ 10^4$ sec for HCN). The quantity $f(x)$ is a geometrical factor that represents the fraction of relevant molecules within the observed diaphragm: for diaphragms smaller than the scale length, the flux expected in the sampled region of the coma will be reduced by the factor of $f(x)$. Values of the $f(x)$, considering a circular aperture, are already tabulated and can be found in the literature (see Yamamoto (1982)). In our case, the aperture is described by square pixels and herewith the $f(x)$ was calculated using a Monte-Carlo model (see also the appendix in Hoban et al. (1991)).

Production rates obtained using the 5.9 are called **Spherical Production Rates** (SPR). A SPR calculated from the flux measured at the region in the spatial profile closest to the nucleus is referred as **Nucleus-Centered** Production Rate (NCPR); in our case, the nucleus centered region was considered to cover $\approx 1.3''$ along the slit, corresponding to 15 spatial pixels. For each molecule, NCPR are calculated from each individual detected emission line, and the weighted mean of individual measurements is considered to be the representative NCPR for that species.

To calculate the NCPR offers the advantage to sample the region with the highest S/N ratio, but at the same time, in this way we risk to underestimate it systematically, since the measured flux is affected by atmospheric seeing and comet drifting off the slit (slit losses, Dello Russo et al. (1998)), while $f(x)$ is a modeled parameter, always assuming perfectly centered and focused target. The flux affected by the seeing or by slit losses, will be smaller than the real one, as well as the resulting $F/f(x)$ ratio, and hence the derived production rates.

To avoid this problem, we introduce a correction factor in the following way (see also Bonev (2005))[4]: we first build a spatial profile containing the summed flux of most (or all) the considered molecular lines. We divide this spatial profile in an odd number of $n \times n$ pixel boxes, and for each of them we calculate the spherical production rate (see Fig. 5.5). The boxes dimension n is related to the slit width and to the pixel scale of the instrument; in our case, 5 x 5 pixels boxes were chosen.

With this method, for each box i we can define **symmetric production rates**, Q_i, away from the nucleus region (note that this can be done if the spatial profile has adequate S/N). These production rates are significantly less sensitive to seeing compared to the nucleus-centered value and the resulting error in the ratio $F/f(x)$ would be much smaller than in the nucleus-centered case. Moreover, since we are testing symmetric regions with respect

---

[4]This criterion was initially developed for CSHELL and then adapted to NIRSPEC data, but it is applicable also to other instruments, as CRIRES.
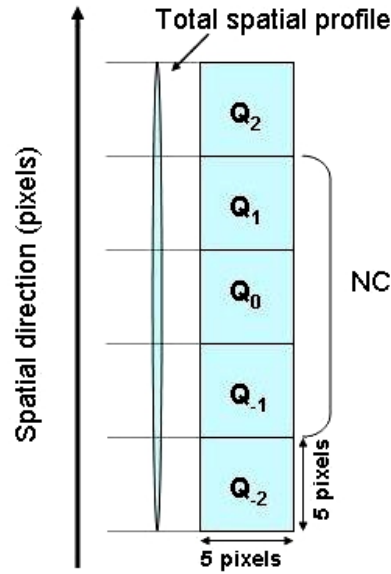
Figure 5.5: Sampling method used for the evaluation of symmetric production rates. The lines of interest in the 2D reduced spectra are summed up to create a total spatial profile, that is then sampled and analyzed in different 5 x 5 pixel boxes, as explained in the text. The pixel region used to determine the nucleus centered production rate is also indicated.

to the center, a slight image off-centering would produce opposite changes on both sides on the spatial profile, and therefore the overall effect is reduced by in the symmetric production rate. The symmetric spherical production rates will reach, at a certain distance from the nucleus, a terminal value named **global** or **terminal Q** (see Fig. 5.6).

The ratio between the terminal production rate value, Q_{term} and the nucleus-centered production rate value, Q_{nc}, both deduced from the combined spatial profile, is called **growth factor**:

$$GF = \frac{Q_{\text{term}}}{Q_{\text{nc}}}. \tag{5.10}$$

The NCPRs retrieved for each line, are finally multiplied by the growth factor to be corrected for the atmospheric seeing effect, and the final production rate is calculated as a weighted mean of the obtained line production rates.

5.2.2 Uncertainties for the production rates

For each line flux, the error is evaluated simply as a standard deviation; the line production rates are calculated as described before, and the corresponding error is just calculated with the normal rules for the propagation of the error. The final production rate is defined as the weighted mean of the single line production rates, and in this last passage we calculated in parallel two types of error: the **stochastic error** and the **standard error** (see also Bonev (2005)).

The stochastic error can be defined as:
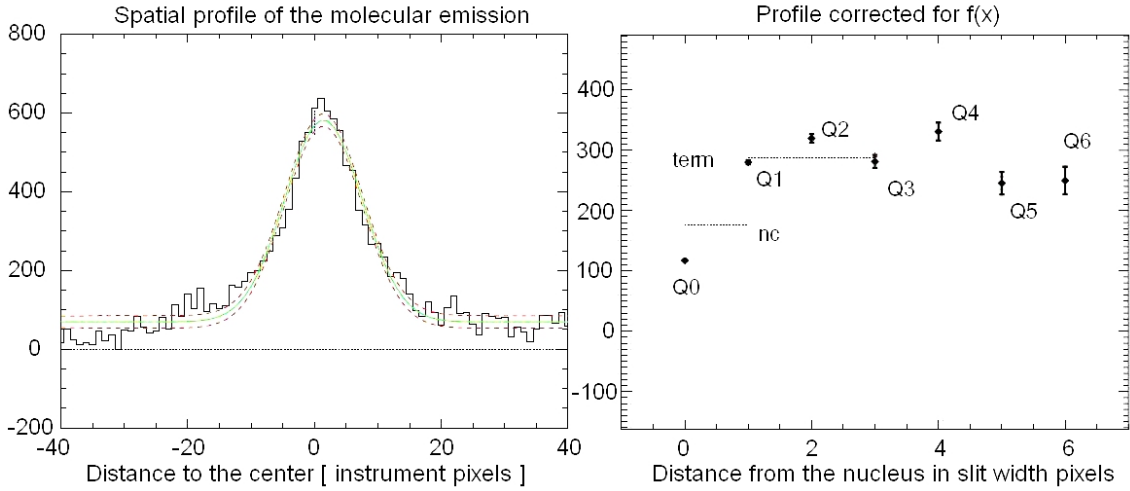
Figure 5.6: Combined C_2H_6 spatial profiles for comet 8P/Tuttle (in the left panel). The spatial profile is fitted with a Gaussian (green line), $\pm 1\sigma$ (red dashed lines). For $i > 0$ the measured flux is averaged over two five-pixel extracts equidistant from the nucleus on both sides. The resulting symmetric production rate are plotted in the right graph; NCPR and terminal production rate are also indicated.

$$\sigma_{\mathrm{stoch}} = \sqrt{\frac{1}{\sum_i \frac{1}{\sigma_{Q_i}^2}}}; \tag{5.11}$$

in the above formula, Q_i is the production rate derived from the ith individual line; σ_{Q_i} is its uncertainty, derived from photon noise. The stochastic noise depends on the individual error bars of the quantities involved, that are in our case the fluxes F_i and the g-factors. The term stochastic comes from the fact that the uncertainty in the flux is dominated by the stochastic photon noise. Low stochastic error means high S/N in the data, but not necessarily consistency between line-by-line measurements of the same quantity.

The standard error depends mainly on the spread of the individual values of F_i and g-factors around the best-fit line. This error can have various origins but the most important source of uncertainty is likely inaccuracies in the fluorescence models, resulting in over- or underestimated g-factors; it can be calculated as

$$\sigma_{\mathrm{stand}} = \frac{s}{\sqrt{N}}, \tag{5.12}$$

where

$$s^2 = \frac{1}{N-1} \frac{\sum \frac{(Q_i - Q_{\mathrm{mean}})^2}{\sigma_{Q_i}^2}}{\frac{1}{N} \sum \frac{1}{\sigma_{Q_i}^2}} \tag{5.13}$$

is the variance for the sample of production rate measurements, and N is the number of sampled lines.
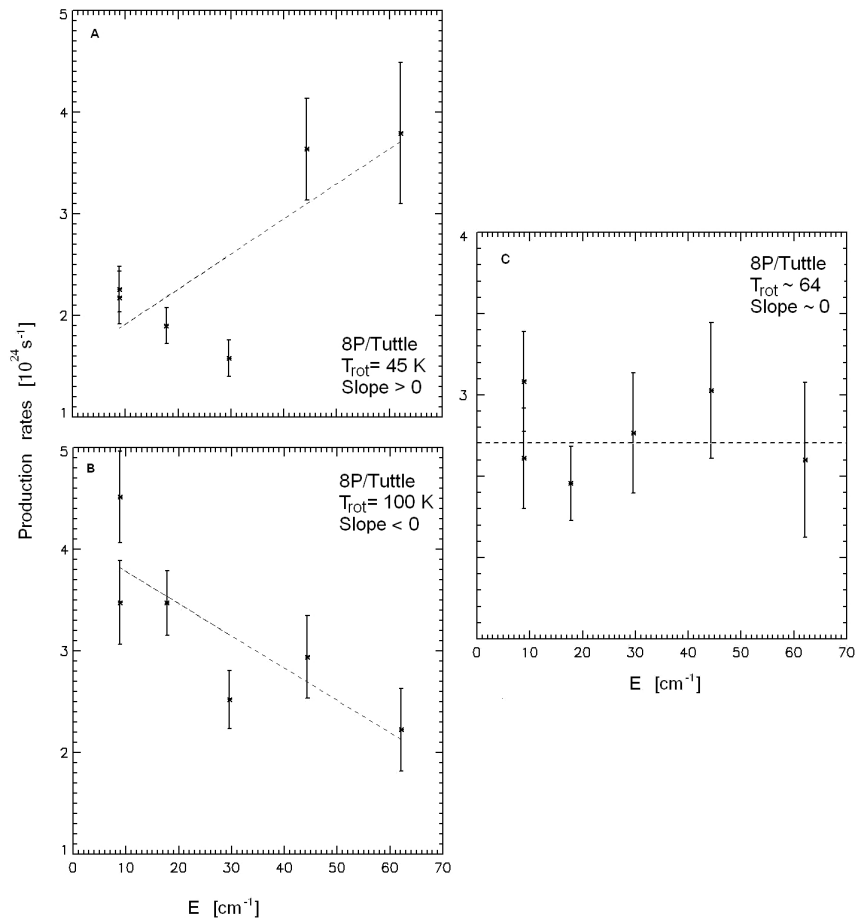
Figure 5.7: Illustration of the variation of the slope of Q vs E: the transition from positive to negative slopes around the optimal temperature is shown.

Other factors include errors in the solar Fraunhofer spectrum and variations in rotational temperature along the sampled line-of-sight in the coma, and unrecognized blends with lines of other coma species.

The standard error usually dominates the stochastic error at the current level of analysis; in all the cases the larger of the two uncertainties is accepted as representative for the measurement error.

5.3   Determination of the rotational temperature

Knowledge of the rotational temperature, T_{rot}, is needed to determine the total production rates from individual line intensities. Conversely, the temperature dependence of the g-factors for individual ro-vibrational lines is needed to obtain an effective rotational temperature from the measured line intensities.

We first assume that a single rotational temperature characterizes all rotational levels in the ground vibrational state. We then estimate the rotational temperature in the ground vibrational state by comparing the transmittance corrected line fluxes with their calculated g-factors.

The relative intensities of the observed lines reflect the population of the rotational levels in the upper vibrational state, that in turn reflect the temperature dependent distribution in the ground state. At the correct rotational temperature, the quantity $F/g(T_{rot})$ should be independent of the upper state energy, E_{up} (Dello Russo et al., 2004)[5].

The correct rotational temperature will therefore produce a diagram F/g vs E_{up}, with slope of zero (within errors). By comparing the measured fluxes F to modeled emission fluxes at different T_{rot}, one can retrieve the mean temperature in the coma.

This is also a way to verify the reliability of the retrieved g-factors: in fact, the fit will have a positive slope if T_{rot} is lower than its optimal value (see Fig. 5.7, panel A), meaning that for lines with relatively low rotational excitation the g-factors are overestimated, while for high-values of E_{up} the g-factors are underestimated.

Conversely, when T_{rot} exceeds its optimal value the slope is reversed to negative because the g-factors for the low excitation lines are underestimated (see Fig. 5.7, panel B), while the modeled emission rates from high-excitation lines are larger than observed (see Fig. 5.7, panel A).

The retrieved rotational temperature is most accurate when a wide range of rotational energies are sampled. In certain cases, such as when the observed emission lines are weak relative to the continuum or blended with the ones of other species, it is more difficult to determine a reliable measurement of the rotational temperature, and that theoretical values has to be used.

5.4   Solar flux effects and Swings effect

The fluorescence excitation of a ro-vibrational band depends on the absolute solar flux that excites the molecule, and it is function of the heliocentric velocity of the comet. Thus, the retrieved g-factors can be strongly affected by the countless Fraunhofer absorption lines in the solar spectrum, lines that are shifted from day to day, depending on the Sun-comet relative velocity.

Indeed, the Doppler shift has two contributions: the heliocentric velocity component of the comet's orbital velocity (**Swings effect**, (Swings, 1941)), and the motion of the molecules with respect to the nucleus (Greenstein effect, (Greenstein, 1958)). Since the latter is important only for fast moving atoms, such as Na, or ions, we will consider it negligible.

Once we had developed the HCN model, we tested the influence of the Swings effect on the emission g-factors, and this on the final production rates for this molecule.

To reproduce the solar spectrum we used an empirical model (Hase et al., 2006) multiplied by a stellar flux model (continuum only, Kurucz (1997)). This choice is determined by the fact that the Hase model consists of an empirical line-by-line list model of the solar transmittance spectrum, that includes intensities and identifications for each line and a parameterization of the line shape. It also accounts for the broadening due to solar rotation, and the extent of center-to-limb variation of lines and continuum brightness temperature. By multiplying the highly realistic transmittance spectrum by Hase with the

---

[5]In a strict sense, one should show the ratio F_{line}/g_{line} as a function of the weighted average of rotational energies in the lower state, however this is less straightforward and makes no significant difference in the retrieved rotational temperature (Dello Russo et al., 2004).
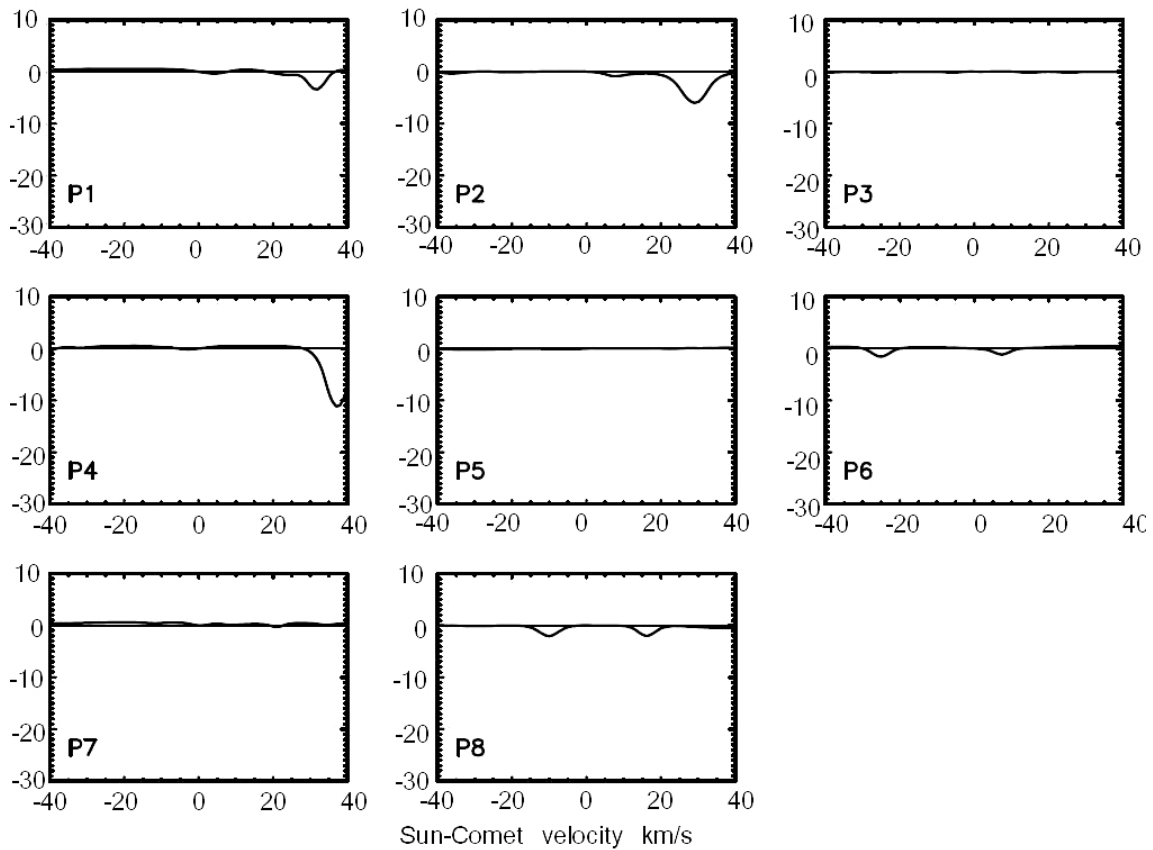
Figure 5.8: Percent differences between emission g-factors calculated considering the Swings effect and considering Sun-comet velocity equal to zero, for the P branch of the spectrum. For each panel the corresponding label for the considered line, Pi, is shown.

8P/Tuttle, Jan 28th, 2008, v_{sc} = 0.5 km/s				
v (cm^{-1})	Transition	$Q_D(10^{25}$mol/s)	$Q_{ND}(10^{25}$mol/s)	$\Delta\%$
3331.58	R6	2.37 ± 0.43	2.36 ± 0.43	1
3328.77	R5	2.70 ± 0.37	2.71 ± 0.37	1
3325.95	R4	2.48 ± 0.33	2.45 ± 0.33	3
3305.54	P2	2.70 ± 0.27	2.67 ± 0.26	3
3302.55	P3	2.16 ± 0.20	2.13 ± 0.20	3
total		2.82 ± 0.25	2.81 ± 0.25	1

Table 5.4: Comparison between HCN lines and total production rates, calculated considering the Swings effect (Q_D) and considering Sun-comet velocity equal to zero (Q_{ND}), for comet 8P/Tuttle. In the first column the wavenumber of the transition is indicated, while in the second the label of the line is indicated.

highly accurate continuum model by Kurucz, we generated a high quality flux-calibrated solar spectrum in the region of interest (see Fig. 5.3).

In the case of the HCN model the effect of the Doppler shift was analyzed in detail. Line pumping g-factors and line emission g-factors were calculated for different comet-Sun velocities, from -40 km/s to $+40$ km/s, with a step of 1 km/s. In figures 5.8 and 5.9

71
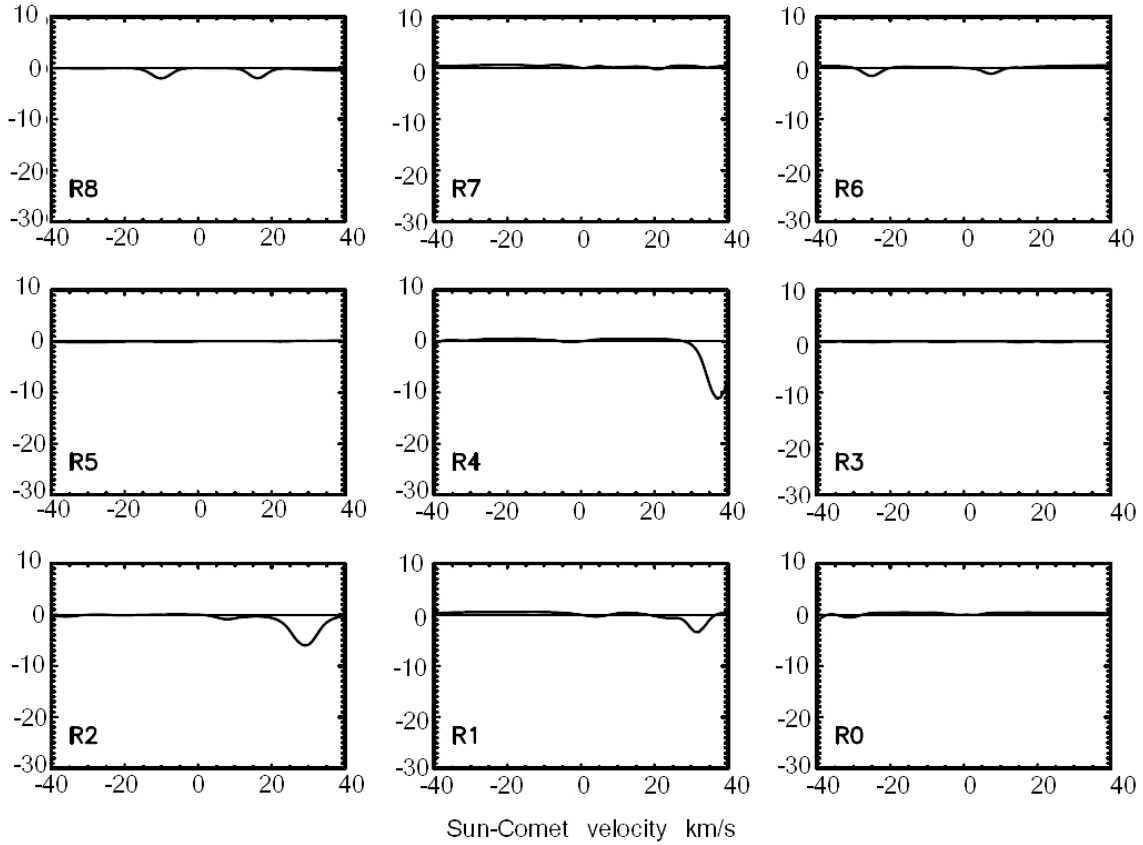
Figure 5.9: The same as in figure 5.8, but for the R-branch.

C/2007 W1 (Boattini), May 30th, 2008, v_{sc} = 0.97 km/s				
v (cm^{-1})	Transition	$Q_D(10^{25}$mol/s)	$Q_{ND}(10^{25}$mol/s)	$\Delta\%$
3331.58	R6	6.97 ± 0.58	6.93 ± 0.58	4
3328.77	R5	4.18 ± 0.66	4.23 ± 0.67	5
3305.54	P2	4.81 ± 0.45	4.76 ± 0.45	5
3302.55	P3	6.21 ± 0.37	6.12 ± 0.36	9
3293.44	P6	4.04 ± 0.35	3.99 ± 0.34	5
total		5.16 ± 0.55	5.11 ± 0.54	5

Table 5.5: Comparison between HCN lines and total production rates, calculated considering the Swings effect (Q_D) and considering Sun-comet velocity equal to zero (Q_{ND}), for comet C/2007 W1 (Boattini). In the first column the wavenumber of the transition is indicated, while in the second the label of the line is indicated.

the effects of the comet-Sun relative velocity on the values of the single line g-factors of our model are shown. The figures show that not all the g-factors are affected in the same way by the Fraunhofer lines. To quantify the Swings effect for the HCN-v_1 transition the production rates for the observed comets were evaluated in case of v = 0 km/s (no-Doppler shift) and in the real case; the results are compared in tables 5.4 and 5.5.

For comet 8P/Tuttle we can see that the difference in line production rates can be up to 3%, but the total effect in the retrieved total production rate is only 1%; for comet C/2007 W1 (Boattini), the effect is a bit higher ($\approx$ 5%), since the difference in line produc-

tion rates can be up to 9%; for both comets, the effect on the g-factor values is negligible, and it is well in the errorbar. In general, the Swings effect for the ν_1-HCN band is not really strong, but it can become important for other ro-vibrational bands, and for other molecules: this is for example the case case of the $1 - 0$ band of CO, where the difference can be up to 15% (see for example Kawakita et al. (2008)). Estimations similar to the ones presented here for the HCN-ν_1 transition should be done for each molecule, and for each comet, to avoid incorrect production rate estimates.

6 Production rates for observed comets: results and discussion

In chapter 5 we have described the steps necessary to build a molecular model for the HCN-ν_1 transition. We used the developed model to retrieve the production rates and, where possible, the rotational temperatures, for the HCN molecule, for the observed comets; these results are described below. The results obtained for other molecules, that will be presented in this chapter, were analyzed and retrieved using already well developed models, by Geronimo L. Villanueva, Michael A. DiSanti, and Boncho P. Bonev, at Goddard space flight center, in Washington DC, under the supervision of Michael J. Mumma.[1]

6.1 Comet 8P/Tuttle

Comet information and observing conditions

Periodic comet 8P/Tuttle (hereafter, 8P) was discovered independently by Tuttle in Cambridge/USA (on January 4th, 1858) and by Bruhns in Berlin/Germany (on January 11th, 1858). An orbital period of 13.6 years, an inclination of about 55 deg and a Tisserand's parameter $T_J < 2$ identify the orbit of 8P as "Halley-type".

Comet 8P/Tuttle has been observed on 13 returns to perihelion, but conditions for study were especially favorable during the 2007/2008 apparition, when 8P came close to Earth (minimum distance 0.25 AU on January 2nd, 2008; maximum visual brightness $M_v \approx 5.3$ mag) with perihelion passage at 1.02 AU a few weeks thereafter on January 27th, 2008. These conditions are highly favorable for infrared detections of parent volatiles from cometary ices and the direct measurement of abundance ratios in the evaporating material.

Observations of 8P and the respective flux calibration standard star (BS718, RA = 02 04 29.4, DEC = 08 27 36.0, type = B9III, $M_v = 4.28$, $M_L = 4.43$), were performed in service mode near perihelion (UT 27.02 Jan. 2008), spanning the UT dates 26th - 29th January 2008; during this period the seeing varied between about 0.4" and 1.5".

A slit width of 0.4" (resulting in a spectral resolving power of $\approx 50,000$) was used for the comet, for all wavelength settings reported here; for the star a slit width of 0.8" was used, for all the wavelength settings.

---

[1]For comet 8P/Tuttle data are published in Böhnhardt et al. (2008) and Villanueva et al. (2009), while, for comet C/2007 W1 Boattini, results were communicated in private form, by M. DiSanti, before publication.

Settings (cm^{-1})	Molecules	DIT (s)	NDIT	AB Cycles	Total integration time (s)	Slit width (arcsec)
8P/Tuttle						
D1 = 3483.59 – 3463.86 D2 = 3458.41 – 3439.67 D3 = 3434.72 – 3416.96 D4 = 3412.33 – 3395.40	H$_2$O, OH*	30	4	8	960	0.4
D1 = 3313.99 – 3316.43 D2 = 3312.14 – 3297.44 D3 = 3293.57 – 3279.74 D4 = 3276.15 – 3263.17	HCN, C$_2$H$_2$	30	4	8	960	0.4
D1 = 3031.60 – 3016.27 D2 = 3012.04 – 2997.54 D3 = 2993.71 – 2980.01 D4 = 2976.44 – 2963.55	C$_2$H$_6$, CH$_4$	30	4	8	960	0.4
D1 = 2884.80 – 2869.51 D2 = 2865.28 – 2850.79 D3 = 2846.96 – 2833.25 D4 = 2829.68 – 2816.75	CH$_3$OH, H$_2$CO	30	4	8	960	0.4
D1 = 2179.86 – 2167.94 D2 = 2164.65 – 2153.34 D3 = 2150.36 – 2139.65 D4 = 2136.87 – 2126.76	H$_2$O, CO	15	8	8	960	0.4
BS718						
All the settings except CO		5	4	6	120	0.8
CO setting		4	5	6	120	0.8

Table 6.1: Observing parameters for 8P and for the flux standard star observations. The range in wavenumbers corresponding to each of the four detectors (Di) are listed. In the second column the molecules expected to be detected are indicated. For each setting, a nodding of 15 arcsec and a jittering of 5 arcsec were used.

Date	R_h(AU)	$v_\odot$(km/s)	Δ (AU)	$v_\oplus$(km/s)
25-26 Jan, 2008	1.027	−0.383	0.494	24.695
26-27 Jan, 2008	1.027	0.015	0.508	24.741
28-29 Jan, 2008	1.028	0.802	0.536	24.710

Table 6.2: Ephemeris information for 8P, for CRIRES observations. In the table, R_h and Δ, both in AU, are the heliocentric and geocentric distances, respectively, $v_\odot$ is the comet-Sun relative velocity and $v_\oplus$ is the comet-Earth relative velocity.

Date	Air Mass	Seeing (")	Humidity %	Telescope Report
25-26 Jan, 2008	$1.198 - 1.425$	$0.7 - 3.2$	$30 - 50$	Clear+some thick clouds+windy
26-27 Jan, 2008	$1.207 - 1.870$	$0.4 - 1.4$	$4 - 16$	Clear-Photometric
28-29 Jan, 2008	$1.225 - 1.235$	$0.5 - 1.1$	$5 - 11$	Clear

Table 6.3: Observing conditions for 8P, for the executed observations. Air mass and seeing ranges during the observations are indicated, together with the humidity ranges and the telescope weather report.

We used various instrument settings to sample molecules in the wavelength range $\approx 2.9 - 4.7\,\mu$m (Tab. 6.1). These settings encompassed emission lines of multiple parent volatiles, specifically H_2O, CH_4, CH_3OH, C_2H_6, CO, HCN, C_2H_2, NH_3, NH_2 and H_2CO, and the daughter product OH^* (prompt emission).

For all observations, the telescope was nodded along the slit in an ABBA sequence with the two beams separated by 15" (one-half the length of the slit); in addition to this standard nodding, the comet was jittered along the slit by adding a small random (but well known) offset of up to $\approx \pm 5$.

In table 6.1 we summarize integration times and other used observing parameters, in table 6.2 we report the astronomical information for the selected target and in table 6.3 we list the parameters that describe the quality of each night for the observing time.

6.1.1   Results and discussion for 8P/Tuttle

Data were reduced and analyzed using the procedures described in chapters 4 and 5.

Figures from 6.2 to 6.8, show the detection of six parent volatile species (H_2O, CH_4, C_2H_6, CH_3OH, CO and HCN), and one daughter specie (OH, prompt emission). An upper limit for H_2CO was also obtained (3σ upper limit); in the same figures it is possible to recognize the presence of the dust continuum level: this is represented for each figure, in the upper spectra, by a red line that corresponds to the convolution of the synthetic atmospheric spectra and the dust continuum of the comet. The extracted production rates and mixing ratios for 8P/Tuttle are listed in table 6.4.

The water production rate was retrieved from the measurements of January 27th, 2008: this night was particularly good in terms of atmospheric quality (low seeing and low humidity values), so that the result can be considered highly reliable. During the same night H_2O was observed using two different wavelength settings (the one covering the spectral range between 3483.59 and 3395.40 cm^{-1}, and the one covering the spectral range between 2179.86 and 2126.76 cm^{-1}), that gave production rates of $(597 \pm 27)10^{26}$ mol/s and $(544 \pm 38)10^{26}$ mol/s, respectively; the obtained results agree within the error.

Species	Mean ν (cm^{-1})	Time start (UT)	Time end (UT)	Q (10^{26}mol s^{-1})	Mixing Ratio (%)	T_{rot} (K)
			26 Jan 2008			
C_2H_6	2988	01:40	02:18	1.77 ± 0.18	0.30 ± 0.03	(60)
CH_4	3014	01:40	02:18	2.12 ± 0.50	0.36 ± 0.09	(60)
			27 Jan 2008			
H_2O	3445	01:28	02:06	597 ± 27	100	60^{+8}_{-9}
H_2O	2160	02:59	03:53	544 ± 38	100	(60)
C_2H_6	3000	02:13	02:52	1.68 ± 0.36	0.28 ± 0.06	(60)
CH_4	3012	02:13	02:52	2.20 ± 0.47	0.37 ± 0.08	(60)
CH_3OH	2999	02:13	02:52	20.0 ± 1.90	3.36 ± 0.40	(60)
CO	2156	02:59	03:53	2.43 ± 0.43	0.45 ± 0.09	(60)
			28 Jan 2008			
HCN	3308	01:28	02:47	0.28 ± 0.03	0.05 ± 0.02	64^{+6}_{-5}
			29 Jan 2008			
CH_3OH	2844	01:14	02:00	19.4 ± 1.61	3.24 ± 0.32	(60)
H_2CO	2834	01:14	02:00	< 0.5	< 0.1	(60)

Table 6.4: The parent volatile composition of comet 8P/Tuttle as measured with CRIRES/VLT. All mixing ratios are based on the high-quality water production rate measured on January 27th, 2008, 01:28 - 02:06 UT, except for CO for which H_2O was measured simultaneously. The formaldehyde value represents the 3σ upper limit, based on stochastic error. Temperatures in brackets are assumed ones. Except for HCN, molecular production rates presented here have been published in Böhnhardt et al. (2008).

A rotational temperature of 60^{+8}_{-9} K was retrieved for the 3445 cm^{-1} measurement, and was adopted for all other species, except for HCN for which a rotational temperature of 64^{+6}_{-5} K has been obtained; the rotational temperatures for H_2O and HCN are consistent within their uncertainties.

The CH_4 production rate measured on successive dates (January 26th and 27th, 2008), are consistent ($(2.12 \pm 0.50)10^{26}$ mol/s and $(2.20 \pm 0.47)10^{26}$ mol/s, respectively), as are the production rates for C_2H_6 ($(1.77 \pm 0.18)10^{26}$ mol/s and $(1.68 \pm 0.36)10^{26}$ mol/s, respectively); methane and ethane have been detected during the same observing nights and using the same wavelength setting (covering the spectral range between 3031.60 and 2963.55 cm^{-1}).

CO and water were measured in the same setting on January 27th, 2008: in some comets CO is the second most abundant volatile, after water, but in 8P/Tuttle it shows a very low mixing ratio (0.45 ± 0.09), if compared with the results from other volatiles in the same comet, and in other comets (see tables 6.4 and 6.5).

On the other side, CH_3OH, measured on January 27th and 29th, 2008, using the wavelength setting covering the spectral region between 2884.80 and 2816.75 cm^{-1}, seems to be the most enriched among the C-bearing molecules, with a mixing ratio of (3.36 ± 0.40) derived from a production rate of $(20 \pm 2)10^{26}$ mol/s.

HCN has been measured using the wavelength setting given in table 6.1, with a resulting production rate of $(0.28 \pm 0.03)10^{26}$ mol/s, that corresponds to a low mixing ratio (0.05 ± 0.02) if compared to other species. For the H_2CO molecule, measured the same night and with the same wavelength setting used for methanol, an upper limit for the

production rate has been obtained ($< 0.5 \ 10^{26}$ mol/s).

6.1.1.1   Comparison between 8P/Tuttle and other comets

Table 6.5 shows the comparison between comet 8P and other comets already studied[2].

For comet 8P, CO (0.45%) falls below the majority of the Oort cloud (OC) comets (mixing ratios ranging from 0.49% to 15.7%), and is much lower than in either 1P/Halley (3.5%) or 153P/Ikeya-Zhang (4.7%), two comets in Halley-type orbits, like 8P; it agrees instead with comets C/1999 S4 (0.75%) and 73P/Schwassmann-Wachmann-C (0.53%), both characterized by fragmentation and disintegration processes, and with C/2006 M4 (0.49%) and C/2000 WM1 (0.52%).

CH_4 (0.37%) is compatible with Jupiter family comets (JF) (0.54% for 9P/Tempel 1 , $< 0.25\%$ for 73P/Schwassmann-Wachmann-C), with 153P/Ikeya-Zahng (0.49%) and with part of the OC comets (namely, C/2006 P1 (0.26%) and C/2000 WM1 (0.34%)).

C_2H_6 in 8P (0.30%) is in average lower than OC comets, even if it is similar to C/2006 P1 (0.36%). It is much lower than in C/2001 A2 (1.7%), and marginally lower than the abundance in 1P/Halley (0.4%); except for 9P/Tempel 1 after impact (0.35%) and 17P/Holmes (1.85%, outburst); it is almost two times the average values found for JF comets (0.17%).

HCN (0.05%) is much lower than in other comets, except for 6P/D'Arrest (0.03%).

The abundance ratio for methanol in 8P (3.3%) is higher by almost a factor of two than the value for 1P/Halley (1.7%) and it is higher than OC comets, except for C/2001 A2, C/1995 O1 and C/2006 M4, that present similar abundances(3.68%, 2.4%, 3.35% respectively). It is higher than the average values of JF comets, except for comet 17P/Holmes (2.37%), that experienced an outburst.

C_2H_2 (0.05%, as measured by Kobayashi et al. (2010) and Bonev et al. (2008)) is compatible with C/2004 Q2 (0.07%), but it is much lower than the values for the other OC comets. It is much lower than in Halley type comets, but, except for 17P/Holmes (0.34%), it is compatible with JF comets.

Except for the high content of methanol, we can regard 8P/Tuttle as a carbon depleted comet[3] (see Fig. 6.1).

There are different hypotheses that can explain the high content of methanol in 8P. An explanation addressed in Bonev et al. (2008), is that comet 8P could be a double comet: radar images (on January 2nd - 4th) show a strongly bifurcated nucleus, possibly a contact binary, with two roughly spherical lobes measuring 3 and 4 km in diameter ($\pm25\%$) that rotates with a rotational period of (7.7$\pm$0.2) hrs (Harmon et al., 2008). The possible binary nature of the nucleus raises the question of heterogeneity. If truly a contact binary, the two components might have formed in chemically dissimilar nebular regions and later been brought together through gravitational mixing processes in the proto-planetary nebula. On the other hand, an objection to this hypothesis comes from the fact that binary comets are

---

[2]Except for the comets presented in this thesis, mixing ratios listed in this table have been already published: for each of these comets, references, production rates and other interesting values are tabulated in appendix D.

[3]It is interesting to notice that previous studies of the production rates of the daughter products C_2 and CN at optical wavelength do not agree with this conclusion, since they reveal a typical composition (A'Hearn et al. (1995)).

expected to be quite unstable objects, and that consequently the two components should separate easily.

If heterogeneous, a nucleus is expected to show temporal variations in the retrieved mixing ratios of a single comet. Comet 8P was observed in the infrared spectral region by three groups, spanning in total the dates December 22nd, 2007 - February 4th, 2008. In table 6.6 all the results are listed. It is possible to notice that all the mixing ratios are quite constant over time, except for CH_3OH, that varies from a minimum of (2.18 ± 0.07) (measured on December 22nd, 2007, Bonev et al. (2008)) to a maximum of (3.36 ± 0.40) (measured on January 27th, 2008, Böhnhardt et al. (2008)) (percent variation $\approx 54\%$), and CH_4, that, in the observation of February 4th, is twice higher as in the previous ones. For other observed comets, for example C/2001 A2, the variation of mixing ratios during time, was much higher (up to a factor of 4); the relative small variation present in 8P could be related more to different data retrieving methods, even if a possible hetereogeneity of the nucleus cannot totally be excluded and further measurements should be taken in order to verify this hypotesis.

Due to the lack of data on parent molecules, in cometary research is still not clear if dynamical and chemical classes could be somehow correlated. In our case, except for the high amount of methanol, comet 8P presents some similarities both with depleted OC comets and with JF comets (in particular with 73P/Schwassmann-Wachmann-C, C/1999 S4 (Linear), C/2000 WM1 and 6P/D'Arrest), and less similarity with comets from the same dynamical class. In this respect, we may deduce that comet 8P formed in a different proto-planetary region with respect other comets, and experienced dynamical processes that turned it, after a certain time, into an Halley type comet. This hypothesis could explain the high enrichment in methanol for this comet: CO can transform in CH_3OH from H-atom addiction reaction on surfaces of icy interstellar grains prior to their incorporation into the nuclei of comets (Watanabe et al. (2004)); this process is efficient only for low temperatures (10 to 20 K), and thus a depletion in CO coupled with an enrichment in CH_3OH should suggest highly efficient conversion of CO and thus low formation temperature. Following Herbst et al. (1983), CH_4 can de-hydrogenate in the methyl radical CH_3; these radicals can react among themselves, forming C_2H_6 molecules, but they can also react with OH molecules, forming CH_3OH; thus, an enrichment in methanol may coincide with a depletion in methane and ethane. Indeed, comet 8P/Tuttle is depleted in all the carbon compounds, except for methanol, so that it could be possible that it formed from planetesimals that originated in a certain region of the proto-planetary nebula, where and when these kind of reactions were highly efficient.

Finally, the orbital period of comet 8P is about 14 years, and the surface of the comet could have experienced surface losses of volatile material during its lifetime, but its interior could be still pristine: in this respect, one should also consider the hypothesis that a new layer of the nucleus could be exposed for the first time to the solar radiation, showing an increase in the volatile production rates. This growth is anyway expected to involve all the elements and not only the methanol content, unless the nucleus is heterogeneous.

Comet	CO	CH_4	C_2H_6	C_2H_2	HCN	CH_3OH
			8P/Tuttle			
Our results	0.45 ± 0.09	0.37 ± 0.06	0.30 ± 0.03	-	0.05 ± 0.02	3.3 ± 0.26
From table 6.6	0.45 ± 0.09	0.37 ± 0.14	0.26 ± 0.08	0.05 ± 0.02	0.07 ± 0.03	2.29 ± 0.65
			Oort Cloud comets			
C/2004 Q2	5.07 ± 0.51	1.36 ± 0.22	0.54 ± 0.08	0.07 ± 0.01	0.15 ± 0.05	1.77 ± 0.19
C/1999 H1	1.8 ± 0.2	0.84 ± 0.26	0.67 ± 0.07	0.25 ± 0.04	0.21 ± 0.03	1.72 ± 0.73
C/2000 WM1	0.52 ± 0.12	0.34 ± 0.10	0.47 ± 0.09	< 0.05	0.15 ± 0.02	1.22 ± 0.30
C/2006 P1	1.45 ± 0.18	0.26 ± 0.05	0.36 ± 0.05	0.39 ± 0.09	0.19 ± 0.03	-
C/2001 A2	3.86 ± 1.02	1.65 ± 0.40	1.61 ± 0.38	0.36 ± 0.15	0.46 ± 0.19	3.68 ± 0.25
C/1996 B2	15.7 ± 4.24	0.78 ± 0.31	0.61 ± 0.22	0.16 ± 0.08	0.18 ± 0.04	1.7 ± 0.4
C/1995 O1	13.26 ± 3.16	1.16 ± 0.42	0.63 ± 0.26	0.29 ± 0.18	0.40 ± 0.10	2.4 ± 0.3
C/2006 M4	0.49 ± 0.20	0.82 ± 0.09	0.49 ± 0.05	-	-	3.35 ± 0.79
C/1999 S4	0.75 ± 0.43	0.12 ± 0.03	0.13 ± 0.02	< 0.14	0.10 ± 0.03	< 0.17
			Halley Type comets			
1P/Halley	3.5	< 1	0.4	0.3	0.2	1.7
153P/I.Z.	4.7 ± 0.8	0.49 ± 0.15	0.62 ± 0.09	0.18 ± 0.05	0.18 ± 0.04	2.5 ± 0.5
			Jupiter Family comets			
21P	10.3 ± 1.87	-	0.22 ± 0.05	< 0.35	< 0.22	1.15
73P-B	< 1.9	-	0.17 ± 0.05	$< 0.03 \pm 0.01$	0.29 ± 0.05	0.19 ± 0.08
73P-C	0.53 ± 0.07	< 0.25	0.11 ± 0.07	0.05 ± 0.02	0.19 ± 0.11	0.19 ± 0.05
17P (Outburst)	-	-	1.85 ± 0.92	0.34 ± 0.05	0.54 ± 0.07	2.37 ± 1.09
9P(Pre Impact)	-	-	0.19 ± 0.12	-	0.18 ± 0.06	1.23 ± 0.11
9P(Post Impact)	4.3 ± 1.7	0.54 ± 0.30	0.35 ± 0.03	0.13 ± 0.04	0.21 ± 0.03	0.99 ± 0.17
6P	-	-	0.29 ± 0.12	< 0.05	0.03 ± 0.01	1.61 ± 0.32

Table 6.5: Comparison between 8P/Tuttle organic composition (mixing ratios), and other already observed comets. For each of these comets, references, production rates and other interesting values are tabulated in appendix D.

Date	R_h (AU)	v_h (km/s)	Δ (AU)	v_Δ (km/s)	Molecule	λ (cm^{-1})	Q (10^{25} mol/s)	M.R. %	Instrument
22 Dec, 2007	1.16	-11.80	0.32	-19.20	H_2O	3429	2280 ± 50	100	NIRSPEC
					C_2H_6	2982	5.49 ± 0.65	0.24 ± 0.03	
					CH_3OH	2852	49.65 ± 1.22	2.18 ± 0.07	
23 Dec, 2007	1.115	-11.56	0.309	-18.2	H_2O	3429	2384 ± 61	100	NIRSPEC
					C_2H_2	3297	< 0.922	< 0.04	
					HCN	3297	1.74 ± 0.13	0.07 ± 0.01	
					CH_4	3037	8.71 ± 0.50	0.37 ± 0.07	
					H_2CO	3037	< 0.96	< 0.04	
					H_2O	2148	2128 ± 111	100	
					CO	2148	< 7.92	< 0.37	
26 Jan, 2008	1.027	-10.82	0.494	24.73	C_2H_6	2988	17.7 ± 1.8	0.30 ± 0.03	CRIRES
					CH_4	3014	21.2 ± 5.0	0.36 ± 0.09	
27 Jan, 2008	1.027	-10.56	0.509	24.76	H_2O	3445	5970 ± 270	100	CRIRES
					C_2H_6	3000	16.8 ± 3.6	0.28 ± 0.06	
					CH_4	3012	22.0 ± 4.7	0.37 ± 0.08	
					CH_3OH	2999	200 ± 19	3.36 ± 0.40	
					H_2O	2160	5440 ± 380	100	
					CO	2160	24.3 ± 0.43	0.45 ± 0.09	
28 Jan, 2008	1.027	0.66	0.53	24.23	HCN	3308	2.80 ± 0.03	0.05 ± 0.02	CRIRES*
					H_2O	3445	4600 ± 400	100	CRIRES
					HCN	3308	3.4 ± 1.1	0.07 ± 0.02	
					C_2H_2	3308	2.1 ± 0.7	0.05 ± 0.02	
29 Jan, 2008	1.028	1.05	0.537	24.76	CH_3OH	2844	194.0 ± 16.1	3.24 ± 0.32	CRIRES
					H_2CO	2834	< 5	< 0.1	
04 Feb 2008	1.036	3.39	0.63	23.61	H_2O	3445	3000 ± 200	100	CRIRES
					CH_4	3012	17 ± 11	0.6 ± 0.4	
					C_2H_6	3000	6.7 ± 1.3	0.23 ± 0.04	
					CH_3OH	2999	97 ± 13	3.3 ± 0.4	

Table 6.6: Comparison between 8P mixing ratios from different observation dates and campaigns. Data from December 22nd to December 23th, 2007, are from Bonev et al. (2008), data from January 26th to January 29th, 2008, are from Böhnhardt et al. (2008) and this work, except for the values related to January 28th that are partly from Böhnhardt et al. (2008) and this work (indicated with an asterisk) and partly from Kobayashi et al. (2010); data related to February 4th are from Kobayashi et al. (2010).

6.1.1.2   Other results obtained for 8P/Tuttle in other observational campaigns

In 2008, comet 8P/Tuttle has been among the most suitable targets for the research of parent volatiles in comets. In the same period this comet has been observed by different groups and different telescopes. In table 6.7 we report the comparison between our results and other published results for the same comet.

For C_2H_6 molecule we can see a good agreement between our results and the results by Kobayashi et al. (2010) obtained using CRIRES at VLT and the ones obtained by Bonev et al. (2008), using NIRSPEC at Keck.

Bonev et al. (2008) obtained an upper limit for the CO mixing ratio (3σ) that formally agrees with our measurement, but seems a bit too small; they also report a mixing ratio for CH_3OH that is significantly smaller than the values reported by us and Kobayashi et al. (2010).

On the other hand CH_4 is the same as the one measured by Bonev et al. (2008), but it is almost half of the value presented in Kobayashi et al. (2010).

HCN is comparable (within the error limit) with the other two observations, even if, in our case, it is a bit lower.

These differences are surprising, since simultaneous observations of parent volatiles and determination of rotational temperatures correct for many systematic errors; they
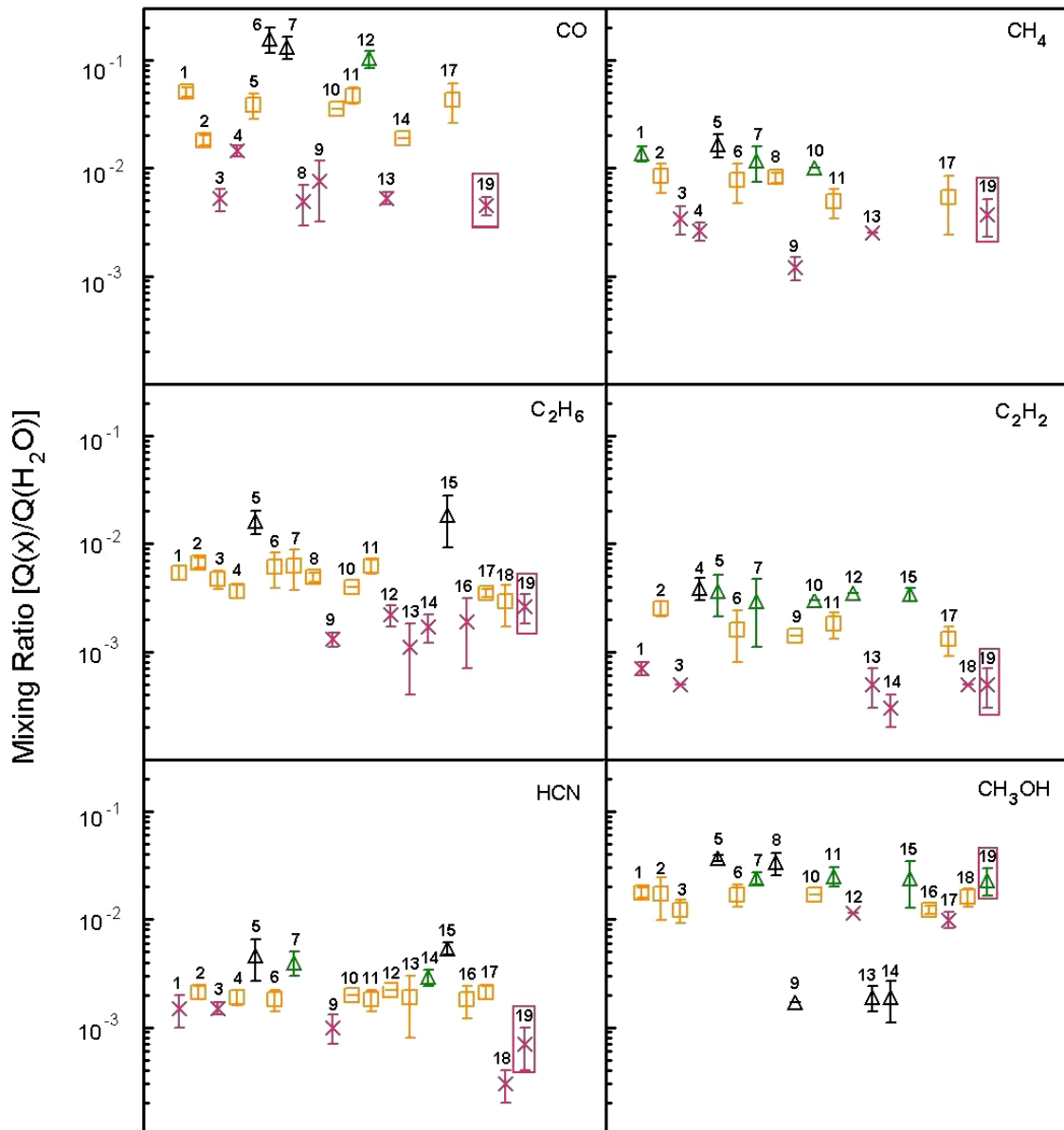
Figure 6.1: Comparison between organic mixing ratios in different comets; for each box, a different molecular mixing ratio with respect to the water is plotted. For each number a different comet is represented: 1 = C/2004 Q2(Machholz), 2 = C/1999 H1 (Lee), 3 = C/2000 WM1 (LINEAR), 4 = C/2006 P1 (McNaught), 5 = C/2001 A2, 6 = C/1996 B2 Hyakutake, 7 = C/1995 O1 (Hale-Bopp), 8 = C/2006 M4 (Swan), 9 = C/1999 S4 (LINEAR), 10 = 1P/Halley, 11 = 153P/Ikeya-Zhang, 12 = 21P/Giacobini-Zinner, 13 = 73P/Schwassmann-Wachmann-C, 14 = 73P/Schwassmann-Wachmann-B, 15 = 17P/Holmes, 16 = 9P/Tempel 1 (Pre-impact), 17 = 9P/Tempel 1 (Post-impact), 18 = 6P/D'Arrest, 19 = 8P/ Tuttle (highlighted by a green box). For each of these comets, references, production rates and other interesting values are tabulated in appendix D. For each molecule, green, yellow and red indicate if the comet is organic enriched, normal or depleted respectively; black is used for super enriched and super depleted comets.

may depend on several factors: first, the comet was observed with different instruments (NIRSPEC for Bonev et al. (2008), CRIRES in our case and for Kobayashi et al. (2010))

Molecule	Mixing Ratios (This work)	Mixing Ratios (Kobayashi et al., 2010)	Mixing Ratios (Bonev et al., 2008)
CO	0.45 ± 0.09	-	< 0.37
C_2H_6	0.29 ± 0.04	0.23 ± 0.04	0.24 ± 0.03
C_2H_2	-	0.051 ± 0.02	< 0.04
CH_4	0.37 ± 0.08	0.6 ± 0.4	0.37 ± 0.07
CH_3OH	3.30 ± 0.36	3.3 ± 0.4	2.18 ± 0.07
HCN	0.05 ± 0.02	0.07 ± 0.02	0.07 ± 0.02
H_2CO	< 0.1	-	< 0.04

Table 6.7: Comparison between 8P mixing ratios from different observation campaigns.

and during different nights: the observing approach, the beam size, the night quality (presence of higher or lower water vapor amount in the Earth atmosphere), can influence the final results. Another reason that could explain the observed differences can be related to different modeling parameters: the use of different constants (like rotational constants in the model, life time of the molecules, slit loss corrections, ...) can lead to different results.

In particular, the inferred total production rates, and consequently the calculated mixing ratios, are quite sensitive to the value assumed for the rotational temperature, especially if only a few ro-vibrational lines are sampled; moreover, the corresponding mixing ratios are dependent on the retrieved (or assumed) water production rates for that night.

For H_2O molecule, we selected 19 lines, and we retrieved a rotational temperature of 60^{+8}_{-9} K; in Bonev et al. (2008) the number of lines that were used is not mentioned, but the retrieved and applied rotational temperature is the same as the one that we retrieved (60 ± 15) K, while Kobayashi et al. (2010) retrieves the water production rate from the analysis of 25 lines, with a rotational temperature of 70 K.

In case of the HCN molecule, we retrieved a rotational temperature of 64^{+6}_{-5} K, using 6 of the 11 detected lines, while (Bonev et al., 2008) and Kobayashi et al. (2010) retrieved a rotational temperature lower than our $(51 \pm 10$ K and 54 K respectively).

Usually, for all other molecules, it is more difficult to retrieve the rotational temperatures, and for these molecules T_{rot} is assumed equal to the water one (i.e. 70 K in Kobayashi et al. (2010), 60 K for (Bonev et al., 2008), 60 K in our work).

If we run our HCN model using the rotational temperature of Kobayashi et al. (2010), we obtain as result a production rate of (0.38 ± 0.03) 10^{26} mol/s, corresponding to a mixing ratio of (0.07 ± 0.01) with respect to water, completely in agreement with the other two results; we anyway compared our measured line fluxes with the ones published in Kobayashi et al. (2010), and we found that our retrieved line fluxes tends to be systematically higher; the different measured fluxes are related by the models to different population of the rotational levels, and this reflects in turns, a different optimal rotational temperature; in this sense, our model gives a correct result for the input line fluxes that we determined, and we can conclude that the difference in the final result may be mainly due to a different reduction of the frames and to a different flux calibration.

Other researcher do not specify which solar model they used for the computation of the g-factors; we have demonstrated in chapter 5 that for the HCN molecule, to consider or not the presence of the Fraunhofer lines, and the Swings effect, should not introduce

Line Flux 10^{-20}W m^{-2}	ν cm^{-1}	ν_D cm^{-1}	Transition	g factor 10^5ph/s/mol	Q_{line} 10^{25} mol/s	Transmittance
3.63 ± 0.86	3331.58	3331.30	R6	1.14	2.37 ± 0.43	0.97
6.21 ± 0.85	3328.77	3328.49	R5	1.60	2.70 ± 0.37	0.94
6.92 ± 9.23	3325.95	3325.67	R4	2.04	2.48 ± 0.33	0.90
6.78 ± 0.80	3320.23	3319.95	R3	2.30	2.15 ± 0.25	0.97
6.86 ± 0.98	3317.32	3317.05	R1-B	1.90	2.64 ± 0.38	0.85
7.16 ± 0.71	3305.54	3305.27	P2	2.18	2.70 ± 0.27	0.97
7.60 ± 0.70	3302.55	3302.28	P3	2.85	2.16 ± 0.20	0.96
6.50 ± 0.74	3299.53	3299.26	P4-B	3.07	1.56 ± 0.18	0.93
7.33 ± 0.68	3290.35	3290.07	P7-B	1.86	2.90 ± 0.27	0.91
3.01 ± 0.61	3287.24	3286.97	P8-B	1.30	1.72 ± 0.34	0.95

Table 6.8: Identified HCN emission lines for comet 8P/Tuttle. For each transition (indicated in the fourth column), the wavenumber (ν_D considering the Doppler effect, and ν not considering the Doppler effect), and the corresponding measured flux (at the top of the atmosphere) are listed. Moreover, modeled line g-factors and retrieved line production rates (Q_{line}), with the relative error, are given. In the last column the values of the terrestrial atmospheric transmittance is shown. The values of this table refer to a retrieved rotational temperature of T = 64^{+6}_{-5} K. The B letter in the fourth column indicates if a detected HCN emission line is blended with emission lines coming from other molecules.

big differences among the results; anyway, the use of a different solar model, combined with other little differences as mentioned before, can sum up to a larger difference in the final results.

6.1.1.3   HCN and CN production rates in comet 8P/Tuttle

For the HCN molecule, using the model described in chapter 5, a total of ten emission lines were identified; for each detected line, the wavenumber of the transition (ν_D considering the Doppler effect, and ν not considering the Doppler effect), and the corresponding line fluxes and line g-factors are listened in table 6.8, together with the retrieved line production rates. In this spectral region, some of the detected HCN lines are blended with emission lines of other molecules: in particular the line at 3317.32 cm^{-1} overlaps with a line produced by NH$_3$, the lines at 3299.53 and 3290.35 cm^{-1} with C$_2$H$_2$, the one at 3287.24 cm^{-1} with C$_2$H$_2$, NH$_3$ and OH*; these lines were omitted from the final computation of HCN production rate.

The corresponding retrieved rotational temperature was 64^{+6}_{-5} K; in figure 6.9 the relative rotational analysis is shown.

The results obtained from the developed HCN model were compared with published CN production rates. As explained already in the introduction, the origin of CN radical in comets is not well understood: it is believed that CN is produced by photolysis of HCN, but this does not find correspondence in some of the observations. Production rates of HCN and CN are, in fact, quite similar for high heliocentric distances of the comet, but as soon as the heliocentric distance decreases, CN production rates increase with respect HCN, suggesting the existence of another source, or other processes involved (Fray et al., 2005).
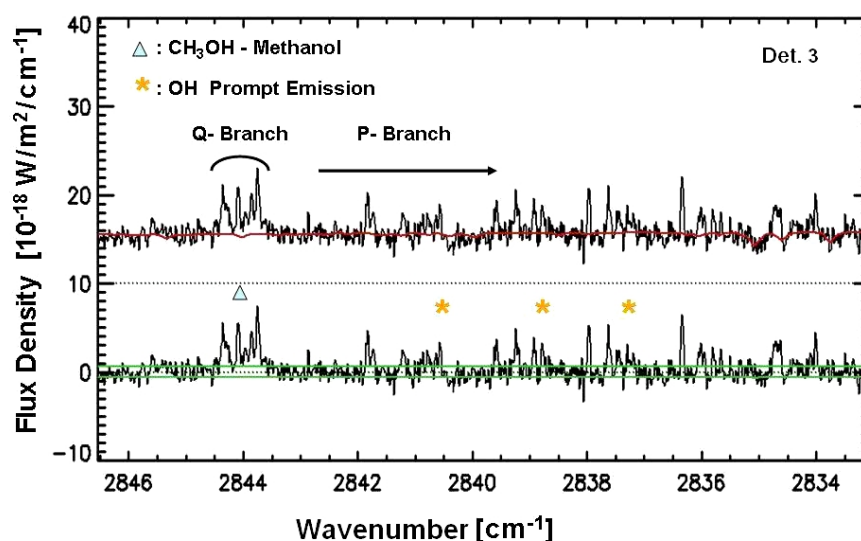
Figure 6.2: Detection of CH$_3$OH (methanol) and OH (prompt emission) in comet 8P/Tuttle, on January 26th, 2008, using the wavelength setting centered at $\approx$ 2857 cm^{-1}. In the upper spectrum the cometary continuum convolved with a synthetic transmittance spectrum of the terrestrial atmosphere is shown by the red line. The lower spectrum is obtained after the subtraction of this contribution; here, the two green lines are the $\pm 1\sigma$ noise envelope. CH$_3$OH Q- and P- branch, and some OH emission lines are indicated. In the upper right corner the corresponding detector number is shown.

For comet 8P/Tuttle the CN radical was measured on December 14th, 2007 by Schleicher (Schleicher and Woodney, 2007) using narrow band photometry; in this date, the comet was at 1.21 AU from the Sun and 0.42 AU from the Earth.

A production rate of $\approx$ 1.66 10^{25} mol/s was obtained, for a mixing ratio (CN/OH, with OH production rate $\approx$ 631 10^{25} mol/s) of 0.26%. Based on this comparison, our results in 8P do not support HCN molecule as the only parent of the CN radical.

In many comets there is evidence that much of the measured CN is produced from grains in the coma rather than from nuclear ices (Combi and Delsemme, 1980; A'Hearn et al., 1995), and this could be the reason why we see an higher production rate of CN with respect to HCN in comet 8P.
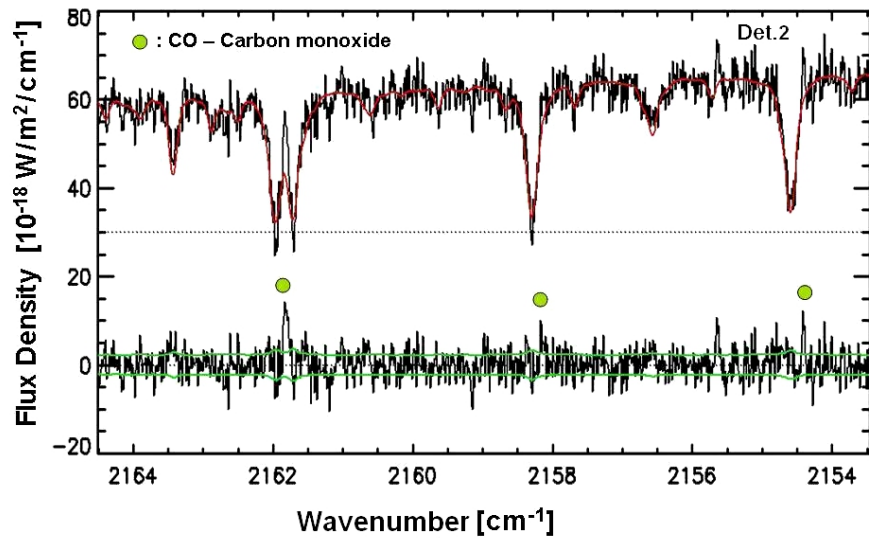
Figure 6.3: Detection of CO (carbon monoxide) in comet 8P/Tuttle, on January 27th, 2008, using the wavelength setting centered at ≈ 2174 cm^{-1}. Some of the CO lines are indicated. For an explanation of the colors, the lines and the labels in the plot, see Fig. 6.2.
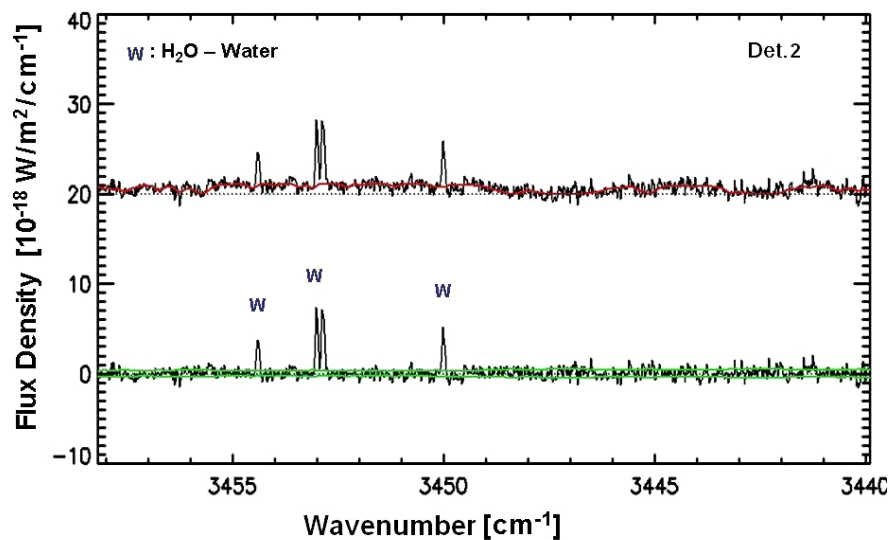
Figure 6.4: Detection of water molecule (H$_2$O) in comet 8P/Tuttle, on January 27th, 2008, using the wavelength setting centered at ≈ 3445 cm^{-1}. Some of the H$_2$O lines are indicated. For an explanation of the colors, the lines and the labels in the plot, see Fig. 6.2.
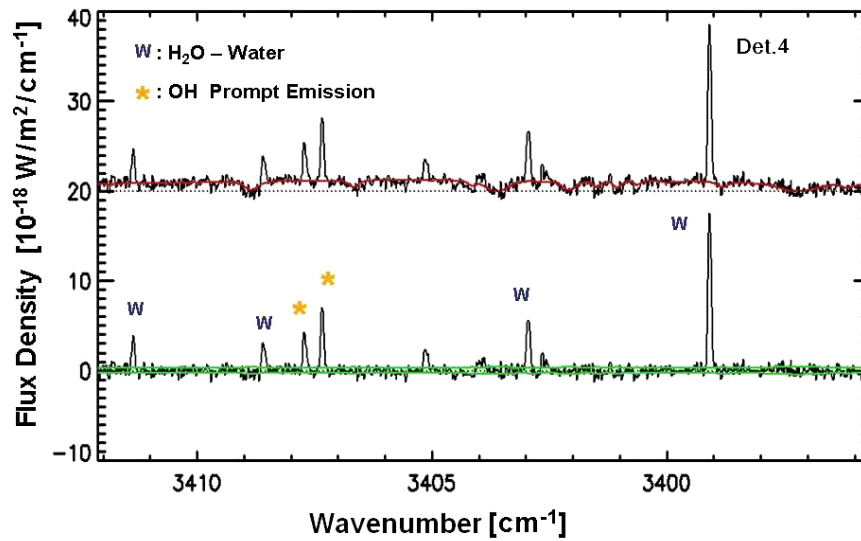
Figure 6.5: Detection of water molecule (H_2O) and OH in comet 8P/Tuttle, on January 27th, 2008, using the wavelength setting centered at ≈ 3445 cm^{-1}. Some of the H_2O and OH emission lines are indicated. For an explanation of the colors, the lines and the labels in the plot, see Fig. 6.2.
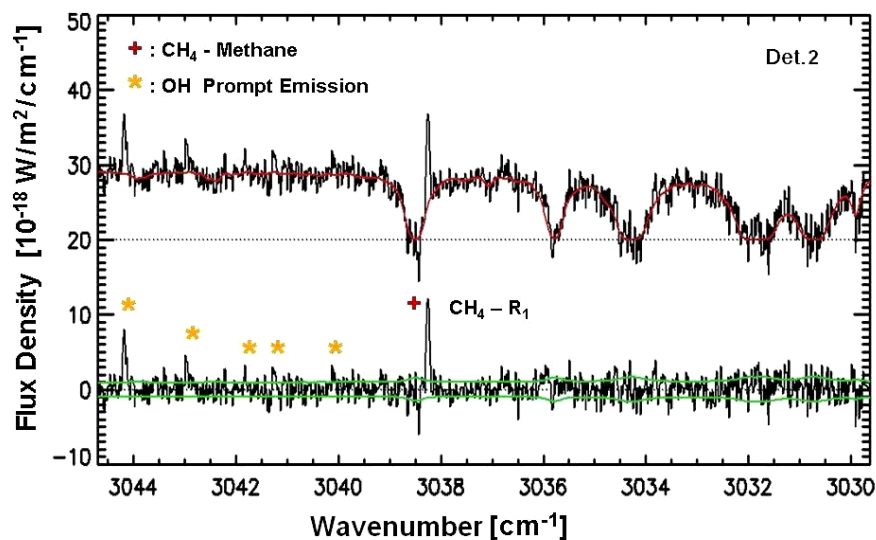
Figure 6.6: Detection of methane (CH_4) and OH in comet 8P/Tuttle, on January 27th, 2008, using the wavelength setting centered at ≈ 3030 cm^{-1}. Some of the CH_4 and OH emission lines are indicated. For an explanation of the colors, the lines and the labels in the plot, see Fig. 6.2.
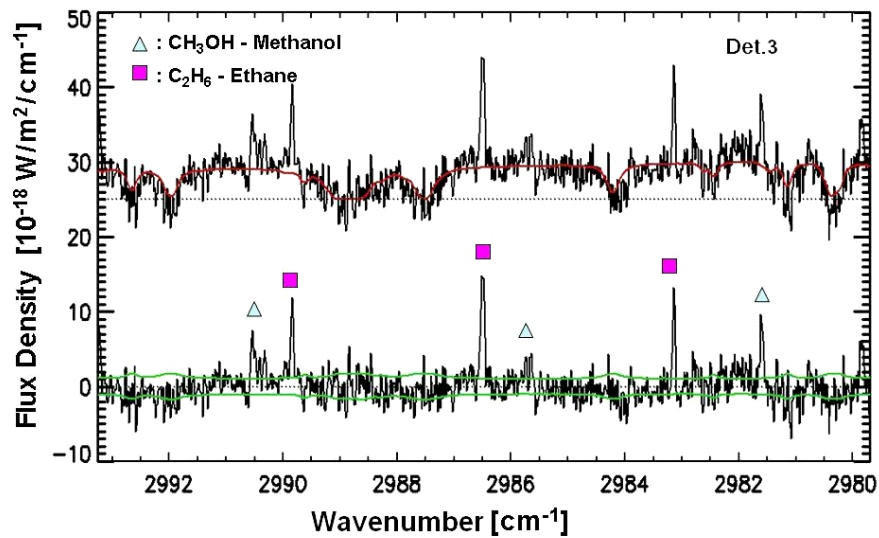
Figure 6.7: Detection of ethane (C_2H_6) and methanol (CH_3OH) in comet 8P/Tuttle, on January 27th, 2008, using the wavelength setting centered at ≈ 3030 cm^{-1}. Some of the C_2H_6 and CH_3OH emission lines are indicated. For an explanation of the colors, the lines and the labels in the plot, see Fig. 6.2.
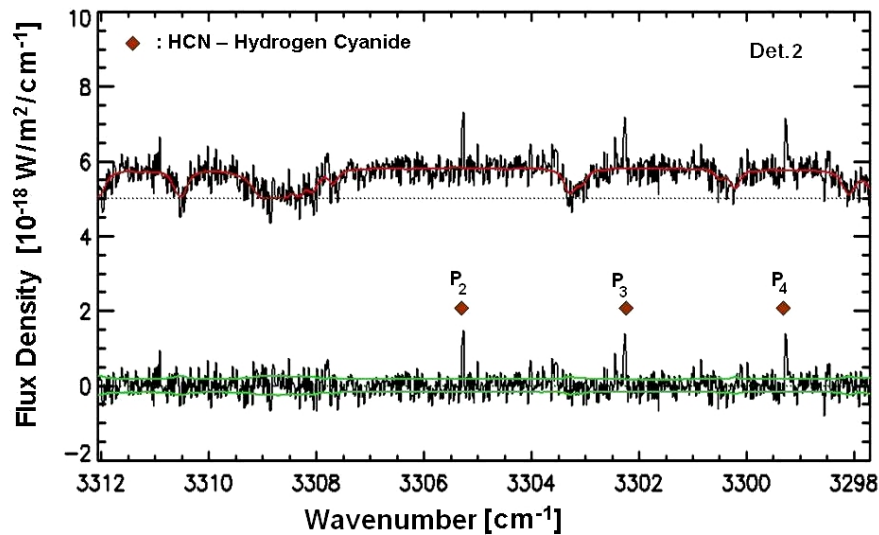
Figure 6.8: Detection of hydrogen cyanide (HCN) in comet 8P/Tuttle, on January 28th, 2008, using the wavelength setting centered at ≈ 3333 cm^{-1}. Some of the HCN emission lines are indicated. For an explanation of the colors, the lines and the labels in the plot, see Fig. 6.2.
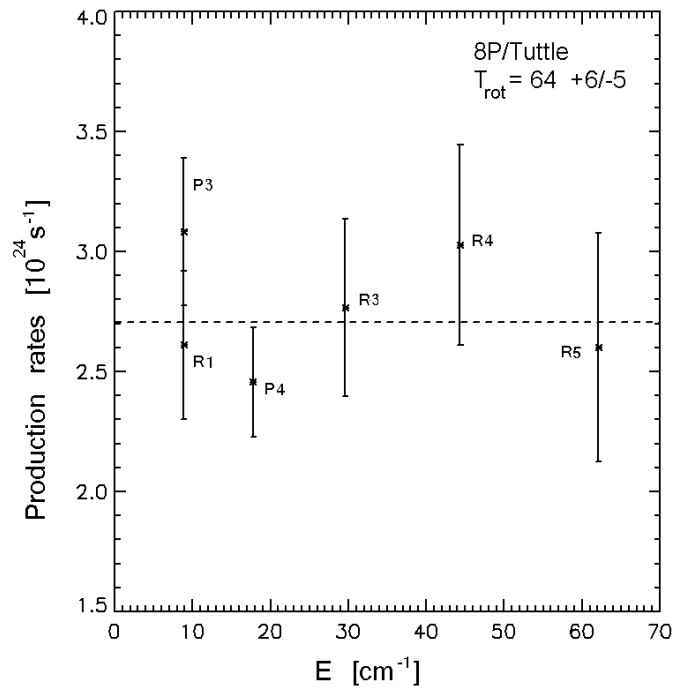
Figure 6.9: Excitation analysis for HCN in comet 8P/Tuttle.

6.2 Comet C/2007 W1 (Boattini)

6.2.1 Comet information and observing conditions

Comet C/2007 W1 (Boattini), hereafter, C/2007 W1, is a dynamically new comet discovered by Andrea Boattini on November 20th, 2007. During 2008, comet C/2007 W1 came close to the Earth (minimum distance 0.21 AU on June 11th, 2008), enough to perform successfully our research.

Comet C/2007 W1 was observed in two different time periods: the first observing run covers the period from May 11th, 2008 to May 30th, 2008, before perihelion, while the second observing run was performed during the first week of July 2008, after perihelion (the minimum heliocentric distance was 0.8497 on June 24th, 2008). In the period of the observations the visible brightness M_v varied from 5 to 7 mag.

Observations of C/2007 W1 and the respective flux calibration standard stars (HR4689 for the first period, BS740 for the second) were performed in service mode. A slit width of 0.4" (resulting in a spectral resolving power of $\approx 50,000$) was used for the comet, for all wavelength settings reported here, while for the star a slit width of 0.8" was used.

As for comet 8P, we used various instrument settings to sample wavelengths in the range $\approx 2.9 - 4.7$ μm, to search for emission lines of multiple parent volatiles, specifically H_2O, CH_4, CH_3OH, C_2H_6, CO, HCN, C_2H_2 and H_2CO, and the daughter product OH^* (prompt emission). For all observations, the telescope was nodded along the slit in an ABBA sequence with the two beams separated by 12". In addition to this standard nodding the comet was jittered along the slit by adding a small random (but well known) offset of up to $\approx \pm 3$".

Settings (cm^{-1})	Molecules	DIT (s)	NDIT	AB Cycles	Total integration time (s)	Slit width (arcsec)
C/2007 W1 (Boattini)						
D1 = 3520.49 – 3503.76	H_2O, OH^*	30	4	8	960	0.4
D2 = 3499.18 – 3483.37						
D3 = 3479.17 – 3464.27						
D4 = 3460.42 – 3446.43						
D1 = 3332.77 – 3317.19	HCN, C_2H_2	30	4	8	960	0.4
D2 = 3312.93 – 3298.22						
D3 = 3294.32 – 3280.48						
D4 = 3276.90 – 3263.91						
D1 = 3050.65 – 3034.80	C_2H_6, CH_4	30	4	8	960	0.4
D2 = 3030.45 – 3015.43						
D3 = 3011.44 – 2997.25						
D4 = 2993.57 – 2980.01						
D1 = 2847.67 – 2833.41	CH_3OH, H_2CO	30	4	8	960	0.4
D2 = 2829.51 – 2816.01						
D3 = 2812.43 – 2799.69						
D4 = 2796.39 – 2784.40						
D1 = 2183.07 – 2171.08	H_2O, CO	15	8	8	960	0.4
D2 = 2167.79 – 2156.41						
D3 = 2153.38 – 2142.60						
D4 = 2139.81 – 2129.63						
HR4689 and BS740						
All the settings except CO		5	4	6	120	0.8
					120	
CO setting		4	5	6	120	0.8

Table 6.9: Observing parameters for C/2007 W1 and for the flux standard star observations. The range in wavenumbers corresponding to each of the four detectors (Di) are listed. In the second column the molecules expected to be detected are indicated. For each setting, a nodding of 12 arcsec and a jittering of 3 arcsec were used.

Date	R_h(AU)	$v_\odot$(km/s)	Δ (AU)	$v_\oplus$(km/s)
11 May 08	1.175	−20.45	0.344	−10.47
26 May 08	1.011	−16.75	0.261	−8.052
30 May 08	0.974	−15.26	0.243	−7.040
01 Jul 08	0.859	4.723	0.289	12.337

Table 6.10: Ephemeris for C/2007 W1 for the executed observations. In the table, R_h and Δ, both in AU, are the heliocentric and geocentric distances, respectively, $v_\odot$ is the comet-Sun relative velocity and $v_\oplus$ is the comet-Earth relative velocity.

Date	Air Mass	Seeing(")	Humidity %	Telescope reports
11 May 08	1.000 − 1.653	0.35 − 1.18	2	Clear-Photometric
26 May 08	1.150 − 1.819	0.4 − 2.4	14 − 24	Some thin clouds
30 May 08	1.300 − 1.984	0.6 − 2.47	2 − 10	Clear
01 Jul 08	1.319 − 1.965	0.5 − 1.4	2	Clear

Table 6.11: Observing conditions for C/2007 W1, for the executed observations. Air mass and seeing ranges during the observations are indicated, together with the humidity ranges and the telescope weather report.

In table 6.10 we report the astronomical information, for the comet, for the observing time, in table 6.11 we list the parameters that describe the quality of the nights for the observing time, while in table 6.9 we provide information on integration times and other observing parameters.

6.2.2   Results and discussion

Data were reduced and analyzed using the procedures described in chapters 4 and 5.

Figures from 6.11 to 6.15, show the detection of six parent volatile species, specifically H_2O, C_2H_6, CH_3OH, CH_4, CO and HCN. Contrary to 8P, comet C/2007 W1 does not show a very strong dust continuum. The extracted production rate and mixing ratio for the HCN molecule in comet C/2007 W1 are listed in table 6.12, together with the results for water molecule in the same observing period (May 26th - 30th, 2008, Michael A. DiSanti, private communication); results relative to other molecules are reported in table A.2.

We detected emission lines from water molecule during the observations performed on May 11th, between May 26th and 30th, and on July 1st, 2008, using the wavelength setting covering the spectral range between 3520.49 and 3446.43 cm^{-1} for all the nights except for the night of the 27th, when water was detected using the same setting as used for the CO molecule (spectral range between 2183.07 and 2129.63 cm^{-1}); for this night the obtained production rate, $(75.98 \pm 12.25)10^{26}$ mol/s, is in agreement with the results obtained for the other observing nights, $(35.64 \pm 4.50)10^{26}$ mol/s (11 May 2008), $(65.42 \pm 4.87)10^{26}$ mol/s (26 May 2008), $(104.2 \pm 13.96)10^{26}$ mol/s (30 May 2008), $(138.2 \pm 5.8)10^{26}$ mol/s (1 July 2008); note that the water production rate (and all the production rates in general) increases as the comet get closer to the Sun, as one should expect; the evolution of water production rate with the heliocentric distance is described in appendix A.

Species	Mean ν	Q	Mixing Ratio	T_{rot}
	(cm^{-1})	$(10^{26}mol\ s^{-1})$	$(\%)$	(K)
26-30 May 2008				
H_2O (26 May)	3445	65.42 ± 4.87	100	(88)
H_2O (27 May)	2160	75.98 ± 12.25	100	(88)
H_2O (30 May)	3445	104.2 ± 13.98	100	88^{+2}_{-3}
HCN (30 May)	3290	0.52 ± 0.06	0.49 ± 0.06	89^{+30}_{-18}

Table 6.12: HCN molecular production rate and mixing ratios (for water molecule, results have been retrieved by Michael A. DiSanti (paper in preparation)).

HCN has been measured on May 30th, 2008, using the wavelength setting covering the spectral region from 3332.77 to 3263.91 cm^{-1}; the retrieved production rate was $(0.52 \pm 0.06)10^{26}$ mol/s corresponding to a mixing ratio of (0.49 ± 0.06); a corresponding rotational temperature of 89^{+30}_{-18} K was retrieved, and this result is in agreement, within the uncertainties, with the one obtained for the water molecule (88 K, Michael A. DiSanti, private communication).

6.2.2.1 Comparison between C/2007 W1 and other comets

In figure 6.10 and table 6.14, we compare results obtained for comet C/2007 W1 (see appendix A) with other results obtained for other comets that are present in the literature.

The abundance ratio for carbon monoxide (6.8%) falls well below the values of comets C/1996 B2 (15%) and C/1995 O1 (12%), but it is similar to other two OC comets, in particular to C/2004 Q2 (5.07%) and C/2001 A2 (3.86%), and to 21P/Giacobini-Zinner ($\approx$ 10%); it is similar to the JF comet 9P/Tempel 1 (4.3%, after impact), and to the Halley type comet 153P/Ikeya-Zahng (4.7%); it is higher with respect all the other comets. CH_4 mixing ratio (1.9%) is similar to comets C/2004 Q2 (1.36%), C/2001 A2 (1.65%), and C/1995 O1 (1.16%), and it is higher with respect other observed comets.

The amount of C_2H_6 (2.35%) is significantly higher than the values found in other comets; in general ethane mixing ratios are less than 1%, except for comet C/2001 A2 (1.7%) and 17P/Holmes (1.85%). C_2H_2 (0.24%) is in general comparable with the majority of OC comets and with two JF comets (17P/Holmes (0.34%) and 21P/Giacobini-Zinner ($< 0.25\%$)).

HCN content (0.36%) is higher than in other Oort cloud comets, except for comets C/2001 A2 (0.46%) and C/1995 O1 (0.40%); it is twice the value found in comet C/1996 B2 and in comet 153P/Ikeya-Zhang (0.18% for both the comets).

Methanol (2.52%) is compatible with other OC comets abundances (mean value $\approx$ 2.38%), it is similar to the one found in 153P/Ikeya-Zhang (2.5%) and 17P/Holmes (2.37%, outburst).

Comet C/2007 W1 shows a high amounts of volatile material and similarities with other Oort cloud comets, in particular with comet C/2001 A2; we can thus classify it as an organic enriched comet, with an high content of ethane.

Considering its volatile content, comet C/2007 W1 (Boattini) could have formed in a cold region of the proto-planetary nebula, where highly volatile species, like CO and CH_4, could exist in their icy form (T< 30 K).

Line Flux (10^{-20}Wm^{-2})	ν (cm^{-1})	ν_D (cm^{-1})	Transition	g factor (10^5ph/s/mol)	Q_{line} (10^{25} mol/s)	Transmittance
29.71 ± 2.47	3331.58	3331.66	R6	1.41	6.97 ± 0.58	0.95
20.98 ± 3.33	3328.77	3328.85	R5	1.74	4.18 ± 0.66	0.71
24.92 ± 2.28	3320.22	3320.29	R2	1.91	4.56 ± 0.42	0.93
19.70 ± 1.86	3305.54	3305.62	P2	1.66	4.81 ± 0.45	0.94
34.84 ± 2.06	3302.55	3302.63	P3	2.24	6.21 ± 0.37	0.86
32.31 ± 1.94	3299.52	3299.60	P4-B	2.55	4.46 ± 0.27	0.92
26.25 ± 2.25	3293.44	3293.51	P6	2.39	4.04 ± 0.35	0.74
22.54 ± 2.25	3290.35	3290.42	P7-B	2.03	3.92 ± 0.39	0.74
20.90 ± 1.67	3287.25	3287.32	P8-B	1.61	4.59 ± 0.37	0.91

Table 6.13: Identified HCN emission lines for comet C/2007 W1 (Boattini). For each transition (indicated in the fourth column), the wavenumber (ν_D considering the Doppler effect, and ν not considering the Doppler effect), and the corresponding measured flux (at the top of the atmosphere) are listed. Moreover, modeled line g-factors and retrieved line production rates (Q_{line}), with the relative error, are given. In the last column the values of the terrestrial atmospheric transmittance is shown. The values in this table refer to a retrieved rotational temperature of T = 89^{+30}_{-18} K. The B letter in the fourth column indicates if a detected HCN emission line is blended with emission lines produced by other molecules.

Since it is a dynamically new comet, it might be the first time that this comet visit the inner Solar System, and its surface could still contain pristine and highly volatile material. In this respect, it is particularly interesting to notice the similarity between this comet and comet 17P/Holmes (17P) that experienced a strong outburst during 2007. Outburst are explosive events, sometimes quite strong, that can happen suddenly in comets; the reasons for these explosions are still not well understood, but, in the moment in which an outburst occurs, new material coming directly from the nucleus interior is expelled by the comet. The similar internal composition of 17P and C/2007 W1, may suggest that these two comets could have formed under the same conditions in the proto-planetary disk, and that, after their formation, they could have experienced different dynamical histories.

In table A.1 we present all the measurements obtained for comet C/2007 W1 in the period May 11^{th}2 - July 1st, 2008; no other inferred measurements have been found in the literature till now. No strong variations in the production rates of the various species within different days are noted in our results, suggesting that comet C/2007 W1 might have an homogeneous nucleus.

6.2.2.2   HCN and CN production rates in comet C/2007 W1

For comet C/2007 W1 nine emission lines of HCN were identified for each the observations; for each detected line the wavenumber of the transition (ν_D considering the Doppler effect, and ν not considering the Doppler effect) and the corresponding line fluxes and line g-factors are listened in table 6.13, together with the retrieved line production rates. Again, in the final computation of HCN production rates we avoid HCN lines that are expected to be blended with other emission lines ($\approx$ 3299 and $\approx$ 3290 cm^{-1} with C_2H_2, $\approx$ 3287 cm^{-1} with NH_3, C_2H_2 and OH^*). The corresponding retrieved rotational temperature was 89^{+30}_{-18} K; in figure 6.16 the relative rotational analysis is shown.
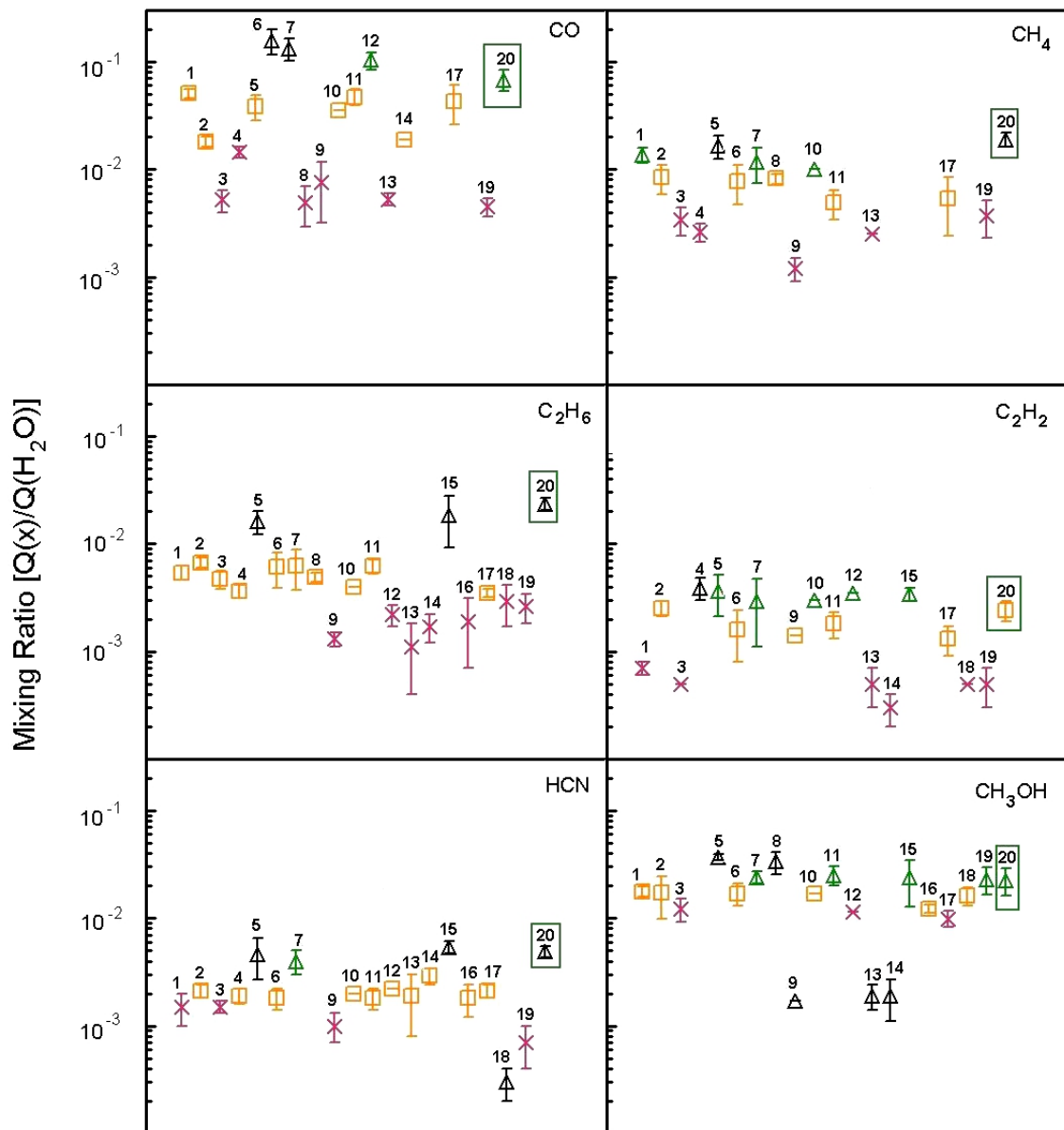
Figure 6.10: Comparison between organic mixing ratios in different comets; for each box, a different molecular mixing ratio with respect to the water is plotted. For each number a different comet is represented: 1 = C/2004 Q2(Machholz), 2 = C/1999 H1 (Lee), 3 = C/2000 WM1 (LINEAR), 4 = C/2006 P1 (McNaught), 5 = C/2001 A2, 6 = C/1996 B2 Hyakutake, 7 = C/1995 O1 (Hale-Bopp), 8 = C/2006 M4 (Swan), 9 = C/1999 S4 (LINEAR), 10 = 1P/Halley, 11 = 153P/Ikeya-Zhang, 12 = 21P/Giacobini-Zinner, 13 = 73P/Schwassmann-Wachmann-C, 14 = 73P/Schwassmann-Wachmann-B, 15 = 17P/Holmes, 16 = 9P/Tempel 1 (Pre-impact), 17 = 9P/Tempel 1 (Post-impact), 18 = 6P/D'Arrest, 19 = 8P/ Tuttle, 20 = C/2007 W1 (Boattini) (highlighted by a green box). For each of these comets, references, production rates and other interesting values are tabulated in appendix D. For each molecule, green, yellow and red indicate if the comet is organic enriched, normal or depleted respectively; black is used for super enriched and super depleted comets.
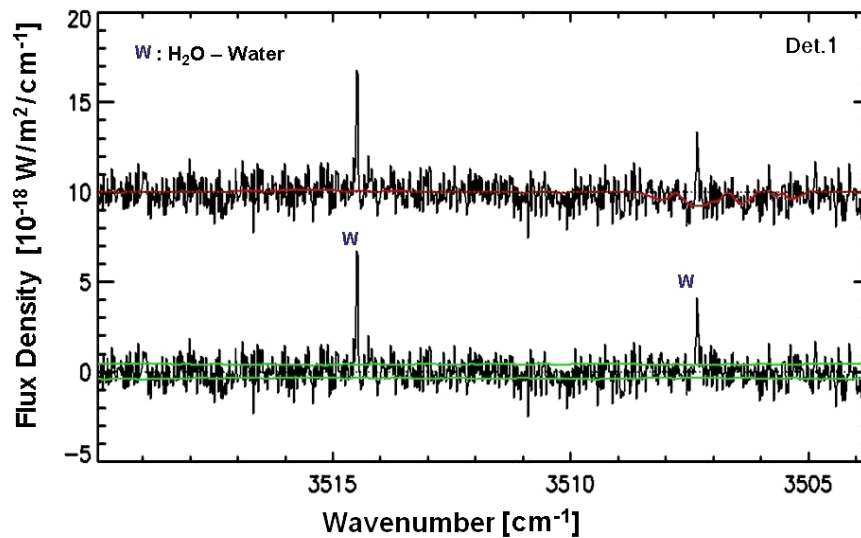
Figure 6.11: Detection of H_2O (water) in comet C/2007 W1, on May 30th, 2008 (see Fig 6.2 for a description).

Narrow band photometry of comet Boattini, observed on July 30th-31st, 2008, gives the following results: OH production rate $\approx 6.16\ 10^{27}$ mol/s, CN production rate $\approx 2.34\ 10^{25}$, C_2 production rate $\approx 4.04\ 10^{25}$ (Schleicher, IAUC 7342). In that period the comet was at 1.07 AU from the Sun and 0.50 AU from the Earth. If we scale the retrieved production rate for HCN ($0.52\ 10^{26}$ mol/s, for an heliocentric distance $r_h = 0.97$ AU and a geocentric distance $\Delta = 0.24$ AU) we obtain a production rate of $\approx (0.25 \pm 0.03)10^{26}$ mol/s, that seems to be in agreement with a CN production rate of $0.23\ 10^{26}$ mol/s; unlike in the case of 8P/Tuttle, this result would be compatible with the assumption that HCN is the only parent species of CN.

The different correlation that we found for HCN and CN in comets 8P and C/2007 W1 may depend on different compositional properties of the two comets and/or on different processes that can be present in the coma. In particular, these two comets have shown a different behavior regarding the dust production rates: comet 8P showed in our spectra an higher dust continuum signal with respect comet C/2007 W1: it is then possible that for comet C/2007 W1 CN was produced only from photolysis of HCN, while in comet 8P/Tuttle this radical was also released from dust grains in the coma.
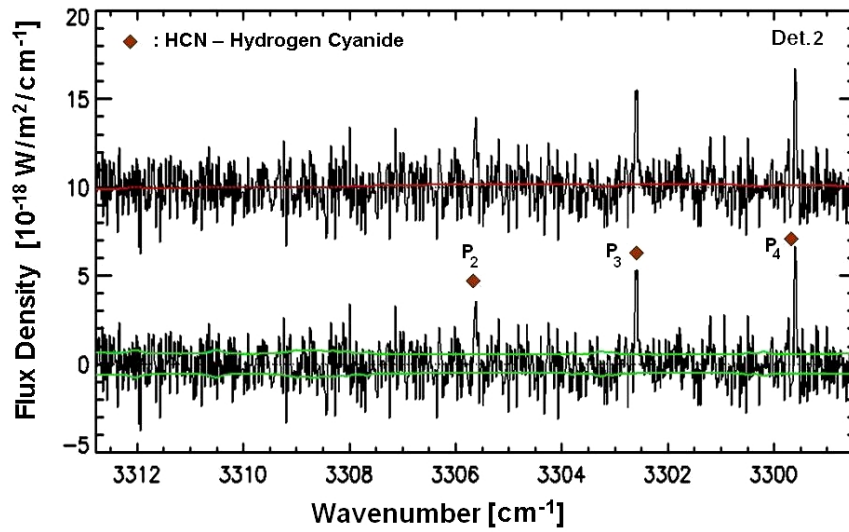
Figure 6.12: Detection of HCN (hydrogen cyanide) in comet C/2007 W1, on May 30th, 2008 (see Fig 6.2 for a description).
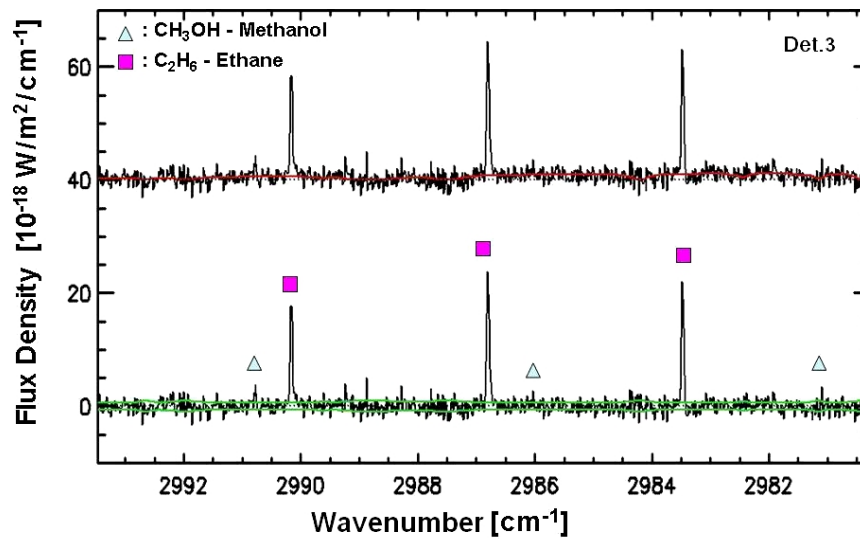
Figure 6.13: Detection of C_2H_6 (ethane) and CH_3OH (methanol) in comet C/2007 W1, on May 26th, 2008 (see Fig 6.2 for a description).

97
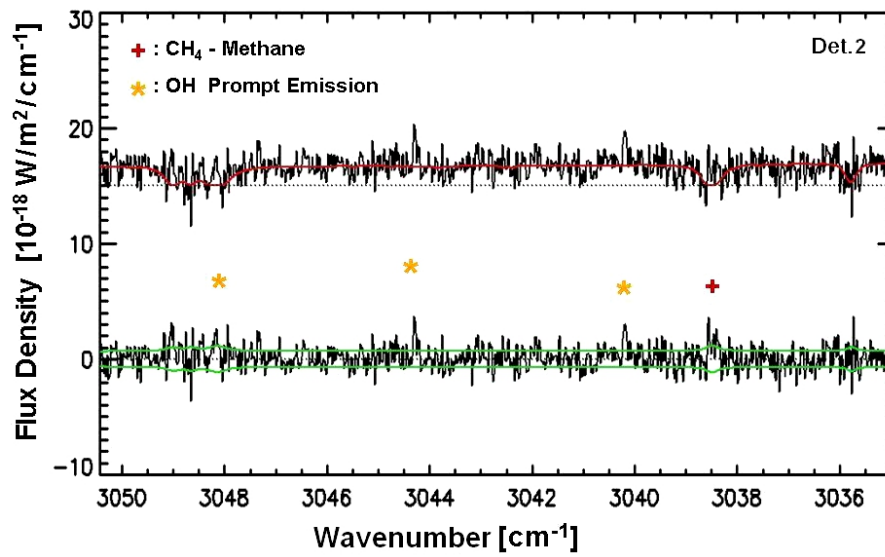
Figure 6.14: Detection of CH$_4$ (methane) and OH (prompt emission) in comet C/2007 W1, on July 1st, 2008 (see Fig 6.2 for a description).
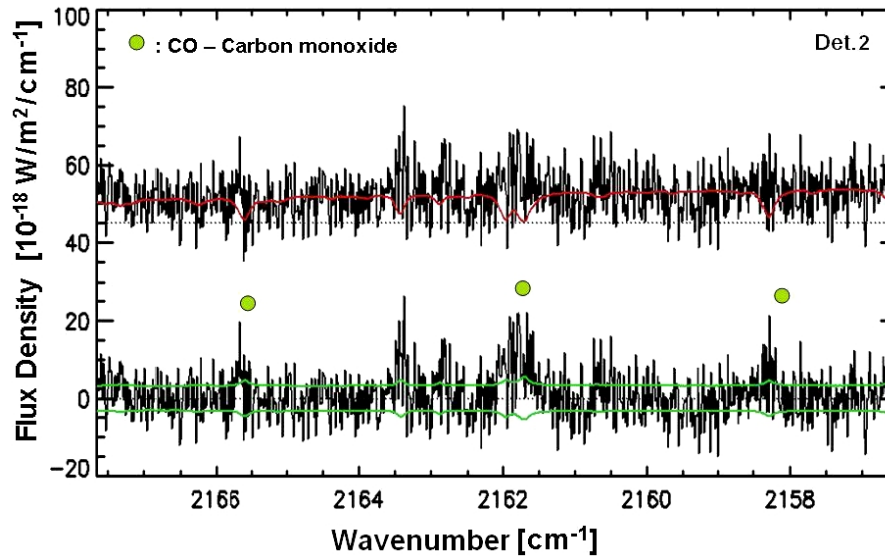
Figure 6.15: Detection of CO in comet C/2007 W1, on May 27th, 2008 (see Fig 6.2 for a description).
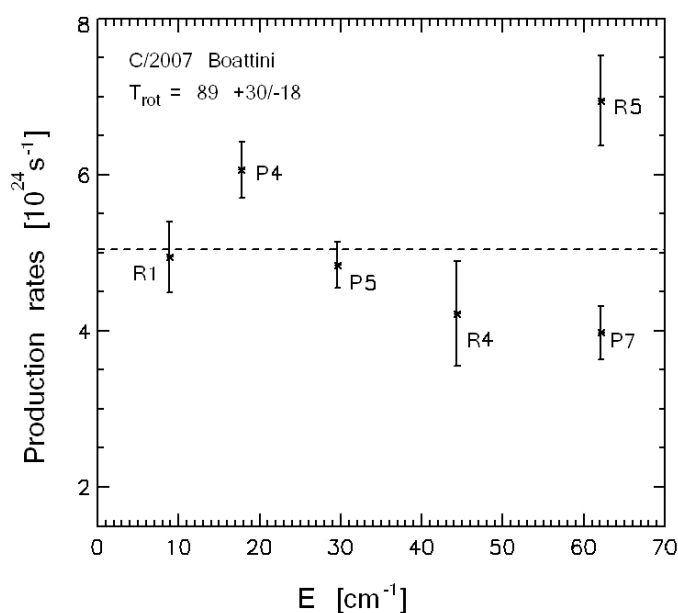
Figure 6.16: Excitation analysis for HCN in comet C/2007 W1 (Boattini).

6.3   Dynamical classes vs chemical classes

The interpretation of cometary chemistry is not straightforward: in fact, the composition of a nucleus can depend on the composition and temperature of the solar nebula where comets formed and on possible radial mixing present in the proto-planetary disk, or even in the proto-solar nebula, before the planetesimal started to aggregate. Moreover, a nucleus can evolve in time since it is subject to various processes during close passages to the Sun (especially in case of short period comets) as well as during their long storage within the Oort cloud and the Kuiper belt. All these possible evolutionary processes make it difficult to separate primitive and evolved chemistry in a diverse comet population. The relative abundances of carbon compounds in a single comet can give clues about the place and the time of its origins, and in particular:

- CO and CH_4 have similar sublimation temperatures: if the temperature was the dominant factor controlling the volatile fraction in the cometary nucleus we would expect their relative abundance to be similar. In table 6.15 we can see that this correlation is visible only for some of the observed comets, so that we may conclude that thermal processes alone did not control the cometary chemistry for all the comets.

- CO can transform in H_2CO and CH_3OH from H-atom addition reaction on surfaces of icy interstellar grains prior to their incorporation into the nuclei of comets. From laboratory analysis, this process is efficient only for low temperatures $(10 - 20$ K$)$. Depleted CO coupled with enriched CH_3OH should suggest highly efficient conversion of CO and thus low formation temperature, even if this assumption is not valid anymore in the inner proto-solar nebula, where elements can be thermally processed prior to their final incorporation into the nucleus (Watanabe et al., 2004).

- Ethane cannot be created by gas phase ion-molecule reactions at low temperatures since most of the relevant reactions are endothermic (Herbst et al., 1983). A process analogous to the previous one is the formation of C_2H_6 from H addition reaction on C_2H_2 ice; ethane can also form from radiation processing of CH_4 (Hiraoka et al., 2000). Thus, if a comet shows a higher abundance of C_2H_6 relative to C_2H_2 and CH_4, it can be possible that these two reaction happened in the proto-planetary nebula. The efficiency of H-addiction reaction for the formation of C_2H_6 from C_2H_2 probably varied greatly with heliocentric distance and/or with time (Herbst et al., 1983).

- Similar hydrogenation of mixed $CO - H_2O$ ice could produce both H_2CO and -CH_3OH, so that a depletion in CO could correspond to an enrichment in the other two species. Also in this case, the efficiency of this process probably varied greatly with heliocentric distance and/or with time.

Organic depleted comets may have formed in the Jupiter - Saturn region, where infalling ices vaporized and chemical processing of sublimated gases modified their composition in the nebula before they later re-condensed. Jupiter family comets are typically depleted, but this depletion could be simply related to the fact that with our technique we sample only the nucleus surface, which could be preferentially depleted of volatile composition relative to the pristine one, as a result of volatile losses from multiple solar passages: good examples are given by the composition of short period comet 17P/Holmes that, after its outburst, showed a composition similar to the one of organic enriched OC comets, and comet 9P/Tempel 1 that showed a different composition before and after the impact.

Organic normal comets and enriched comets show similar signatures (although not identical) to those observed in dense interstellar clouds (DiSanti and Mumma, 2008; Bockelée-Morvan et al., 2004), suggesting that the ices incorporated in comets experienced processing at low temperatures.

In table 6.15 we compare dynamical properties and classes to the organic compositions to understand if connections are present. To build chemical classes is not an easy task: there is not a sharp division among comets, and considering different molecules in the same comet, can lead to two different classifications.

It is possible to compare results and to create, for each molecule separately, five main chemical classes: super-enriched (SE), enriched (E), normal (N), depleted (D) and super-depleted (SD); the criteria used to define this separation are described in appendix D, where also the respective references are given. Looking at table 6.15 it can be seen that some trends are presents: similarities are present among JF comets: this dynamical class seems to contain comets that are chemically more depleted in carbon compounds than other comets.

Halley type comets show also a depletion in organic material, even if for these comets some volatile mixing ratios are quite high with respect to the mean value for all comets.

Regarding Oort cloud comets a certain diversity is present: while the majority of these comets shows a normal or a high amount of carbon compounds, comet C/1999 S4, a dynamically new comet, was depleted in all volatiles and experienced destruction of the nucleus.

The differences that we can test among these comets can be perhaps a sign of possible connections between chemical and dynamical classes; the variations in composition among Oort cloud comets can be related to heterogeneity in the proto-planetary nebula composition, and the diversity among Oort cloud, Halley type and Jupiter family comets can be due to the different dynamical history that the nuclei had experienced.

Unfortunately, the sample of observed comets is still too small to retrieve firm conclusions and further observations and studies are needed.

Comet	CO	CH$_4$	C$_2$H$_6$	C$_2$H$_2$	HCN	CH$_3$OH
C/2007 W1	6.8 ± 1.5	1.9 ± 0.3	2.35 ± 0.28	0.24 ± 0.05	0.49 ± 0.06	2.52 ± 0.63
			C/2007 W1 (Boattini)			
			Oort Cloud comets			
C/2004 Q2	5.07 ± 0.51	1.36 ± 0.22	0.54 ± 0.08	0.07 ± 0.01	0.15 ± 0.05	1.77 ± 0.19
C/1999 H1	1.8 ± 0.2	0.84 ± 0.26	0.67 ± 0.07	0.25 ± 0.04	0.21 ± 0.03	1.72 ± 0.73
C/2000 WM1	0.52 ± 0.12	0.34 ± 0.10	0.47 ± 0.09	< 0.05	0.15 ± 0.02	1.22 ± 0.30
C/2006 P1	1.45 ± 0.18	0.26 ± 0.05	0.36 ± 0.05	0.39 ± 0.09	0.19 ± 0.03	-
C/2001 A2	3.86 ± 1.02	1.65 ± 0.40	1.61 ± 0.38	0.36 ± 0.15	0.46 ± 0.19	3.68 ± 0.25
C/1996 B2	15.7 ± 4.24	0.78 ± 0.31	0.61 ± 0.22	0.16 ± 0.08	0.18 ± 0.04	1.7 ± 0.4
C/1995 O1	13.26 ± 3.16	1.16 ± 0.42	0.63 ± 0.26	0.29 ± 0.18	0.40 ± 0.10	2.4 ± 0.3
C/2006 M4	0.49 ± 0.20	0.82 ± 0.09	0.49 ± 0.05	-	-	3.35 ± 0.79
C/1999 S4	0.75 ± 0.43	0.12 ± 0.03	0.13 ± 0.02	< 0.14	0.10 ± 0.03	< 0.17
			Halley Type comets			
8P/Tuttle	0.45 ± 0.09	0.37 ± 0.06	0.30 ± 0.03	< 0.35	0.05 ± 0.02	3.3 ± 0.26
1P/Halley	3.5	< 1	0.4	0.3	0.2	1.7
153P/I.Z.	4.7 ± 0.8	0.49 ± 0.15	0.62 ± 0.09	0.18 ± 0.05	0.18 ± 0.04	2.5 ± 0.5
			Jupiter Family comets			
21P	10.31 ± 1.87	-	0.22 ± 0.05	< 0.35	< 0.22	1.15
73P-B	< 1.9	-	0.17 ± 0.05	< 0.03 ± 0.01	0.29 ± 0.05	0.19 ± 0.08
73P-C	0.53 ± 0.07	< 0.25	0.11 ± 0.07	0.05 ± 0.02	0.19 ± 0.11	0.19 ± 0.05
17P (Outburst)	-	-	1.85 ± 0.92	0.34 ± 0.05	0.54 ± 0.07	2.37 ± 1.09
9P(Pre Impact)	-	-	0.19 ± 0.12	-	0.18 ± 0.06	1.23 ± 0.11
9P(Post Impact)	4.3 ± 1.7	0.54 ± 0.30	0.35 ± 0.03	0.13 ± 0.04	0.21 ± 0.03	0.99 ± 0.17
6P	-	-	0.29 ± 0.12	< 0.05	0.03 ± 0.01	1.61 ± 0.32

Table 6.14: Comparison between C/2007 W1 organic composition (mixing ratios), and other already observed comets. For each of these comets, references, production rates and other interesting values are tabulated in appendix D.

Comet	e	a (AU)	q (AU)	i (degrees)	P (years)	T_j	Dynamical Class	CO	CH$_4$	C$_2$H$_6$	C$_2$H$_2$	HCN	CH$_3$OH
C/2004 Q2	0.9995	2391.35	1.205	38.58	116942.88		LP	N	E	N	D	D	N
C/1999 H1	0.9997	2773	0.71	149	146000	-0.90	LP	N	N	N	N	N	N
C/2000 W1	1.0002736		0.555	72.55				D	D	N	D	D	D
C/2006 P1	0.999969	10000	0.1712	77.83				D	D	N	SE	N	-
C/2001 A2	0.9997	2530	0.78	36	127000	0.88	LP	N	SE	SE	E	SE	SE
C/1996 B2	0.9999	2296	0.23	125	110000	-0.34	LP	SE	N	N	E	N	N
C/1995 O1	0.9951	186	0.91	89	2537	0.04	LP	SE	E	N	E	E	E
C/2006 M4	1.000265		0.132	111.822				D	N	N	-	-	SE
C/2007 W1	-	-	0.85	9.89	-	-	DN	E	SE	SE	N	SE	E
C/1999 S4	1.0001	-	0.77	149	-	-	DN	D	D	D	N	D	SD
8P/Tuttle	0.8198	5.7	1.03	55	13.6	1.6	HT	D	D	D	D	D	E
1P/Halley	0.967	35.1	0.586	162.3	75.3	-0.58	HT	N	E	N	E	N	N
153P/I.Z.	0.9901	51.2	0.51	28	366.5	0.88	HT/IP	N	N	N	N	N	E
21P/	0.705	3.53	1.04	31.8	6.621	2.471	JF	E	-	D	E	N	D
73P-C	0.6934	3.1	0.94	11	5.4	2.78	JF	D	D	D	D	N	SD
73P-B	0.6935	3.1	0.94	11	5.4	2.78	JF	N	-	D	D	N	SD
17P(outburst)	0.413	3.62	2.161	19.2	6.88	2.86	JF	-	-	SE	E	SE	E
9P(pre impact)	0.5175	3.1	1.51	11	5.5	2.97	JF	-	-	D	-	N	N
9P(post impact)	0.5175	3.1	1.51	11	5.5	2.97	JF	N	N	N	N	N	D
6P	0.613	3.496	0.613	19.5	6.51	2.709	JF	-	-	D	D	SD	N

Table 6.15: Comparison between dynamical and chemical properties of comets. In the table, e is the eccentricity of the orbit, a the semimajor axis, q the perihelion, P the orbital period, T_j the Tisserand's parameter. In column 8, the dynamical types are indicated: LP = long period, DN = dynamically new, HT = Halley type, JF = Jupiter family. In the last six column the chemical properties are listed: SE = super enriched, E = enriched, N = normal, D = depleted, SD = super depleted.

7 Conclusions

Significant progress in measuring parent gas species sublimating from cometary nuclei was achieved over the past decade; newly developed instrumentation made new discoveries possible, and the overall knowledge that scientist have on comets is improving day after day. Nevertheless, a complete full picture of their formation and evolution is far away to be achieved, and every contribution to these studies constitute an important step in cometary science.

The results that we presented in this thesis, together with the description of the methodology used to retrieve production rates of volatiles in cometary comae, represent a small contribution for improving the knowledge that we have in cometary chemistry. In particular:

- observations of comets 8P/Tuttle and C/2007 W1 (Boattini) were performed using CRIRES at VLT. For each comet, production rates of different molecular species have been retrieved and the resulting chemical composition have been studied.

- A new analytical model for the HCN-v_1 transition was developed; this model includes perturbations and updated values for rotational constants; moreover, a highly realistic solar spectrum, including Fraunhofer lines and Sun-comet relative velocity effects (Swings effect), was used in the calculation of fluorescence pumping by solar radiation.

- When possible, the obtained mixing ratios were compared with data present in the literature for the same comet, to test the reliability of our method.

- For each observed comet the retrieved composition was compared with the ones measured for other comets, in order to build a possible chemical classification.

Comet 8P/Tuttle, a Halley type comet, showed a peculiar composition: while the content of carbon monoxide, methane, ethane, and hydrogen cyanide is depleted with respect to water, the amount of methanol is particularly high. Except for the low content of carbon monoxide and hydrogen cyanide, this comet shows similarities with other Halley type comets and, with the exception of methanol, it can be classified as an organic depleted comet.

Comet C/2007 W1 (Boattini), classified as a dynamically new comet, revealed instead a high to medium content, with respect to water, of carbon monoxide, methanol, and hydrogen cyanide and a high content of ethane; it has in general a composition similar to the one of Oort cloud comets, and it can be classified as an organic enriched comet.

The compositional differences among comets may suggest a chemical gradient and/or heterogeneity in the proto-planetary nebula where comet formed, or different processes that can have affected them during their lifetime. No clear connections between chemical compositions and dynamical classes are emerging from comparisons, even if some trends are present: in general, long period comets show a higher range of values for the relative abundances of different species and they are more rich in carbon compounds than short period comets, even if exceptions are present. However, the statistics of objects is not yet adequate to permit firm conclusions on population properties and/or physical conditions at the time of formation. Each comet that can be observed is a significant contribution for increasing the knowledge on primordial conditions in the proto-planetary nebula of the Solar System.

A   Other results for comet C/2007 W1 Boattini

We present here other results obtained during the observations of comet C/2007 W1 (Boattini); these data were analyzed by Michael A. DiSanti and in part by Geronimo L. Villanueva, using the procedures described in chapters 4 and 5.

A.0.1   Results and discussion

We detected emission lines relative to the water molecule during the observations performed on May 11th, between May 26th and May 30th, and on July 1st, 2008, using the wavelength setting covering the spectral range between 3520.49 and 3446.43 cm^{-1}; during the night on May 27th, water was detected using the same setting as used for the CO molecule (spectral range between 2183.07 and 2129.63 cm^{-1}); for this night the obtained production rate, $(75.98 \pm 12.25)10^{26}$ mol/s, is in agreement with the results obtained for the other observing nights, $(35.64 \pm 4.50)10^{26}$ mol/s (11 May 2008), $(65.42 \pm 4.87)10^{26}$ mol/s (26 May 2008), $(104.2 \pm 13.96)10^{26}$ mol/s (30 May 2008), $(138.2 \pm 5.8)10^{26}$ mol/s (1 July 2008); note that the water production rate (and all the production rates in general) increases as the comet get closer to the Sun, as one should expect; the evolution of water production rate with the heliocentric distance is described below, in paragraph A.0.1.1.

CO molecule for this comet presents a production rate of $(3.34 \pm 0.76)10^{26}$ mol/s, and, after water molecule, it is the most abundant observed species in this comet.

We retrieved a production rate of $(2.05 \pm 0.42)10^{26}$ mol/s for CH_3OH, and a production rate of $(1.37 \pm 0.07)10^{26}$ mol/s for C_2H_6; both these molecules were detected in the period between May 26th and May 30th, 2008 (the first using the wavelength setting covering the spectral range between 2847.67 and 2784.40 cm^{-1}, the latter covering the spectral range from 3050.65 to 2980.01 cm^{-1}); C_2H_6 have been detected also on July 1st, giving a production rate of $(3.04 \pm 0.28)10^{26}$ mol/s, and a corresponding mixing ratio compatible with the one measured in May.

CH_4, has been detected the first of July through 3 strong lines, in the same spectral region of C_2H_6; the inferred production rate for this molecule is $(2.62 \pm 0.41)10^{26}$ mol/s; C_2H_2 has been measured on May 30th, 2008, using the same wavelength setting of HCN, for a corresponding retrieved production rate of $(0.25 \pm 0.05)10^{26}$ mol/s.

A.0.1.1   Evolution of water production rate with heliocentric distance

Since the observations of water molecule have covered a relatively long orbital arc of this comet, it was possible to study the dependence of water sublimation on heliocentric distances. In figure A.1 the water production rates versus the heliocentric distance r_h are plotted in a logarithmic scale: a least squares fit to the data give an heliocentric dependence as $Q = (7.41 \pm 1.06)10^{27} r_h^{(-4.55 \pm 0.61)}$, that is a quite steep dependence if we consider that an insolation-limited dependence is given by r_h^{-2}. Other comets, observed in the past, showed flatter heliocentric dependences, for example, as $r_h^{-1.88}$ for comet C/1995 O1 (Dello Russo et al., 2000) or as $r_h^{-1.7}$ for comet C/2001 Q4 Neat (Combi et al., 2009); on the other hand, comet 153P/Ikeya-Zhang showed a dependence as $r_h^{-3.2}$ (Dello Russo et al., 2004).

The r_h^{-2} dependence occurs when and where, in the cometary orbit, the sublimation energy loss rate dominates over the one due to thermal radiation; the steeper dependence that was found in comet C/2007 W1 could be related to seasonal effects (night-day) or to the release of water, not only from the nucleus surface, but also from dust grains present in the coma.
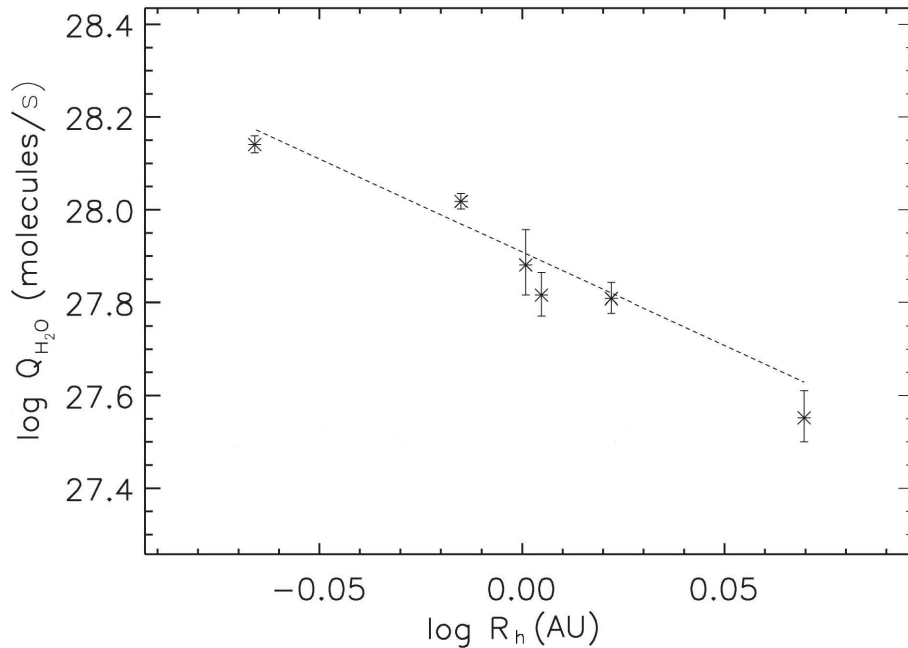
Figure A.1: Heliocentric dependence of water production rate in comet C/2007 W1 (Boattini). (Source Michael DiSanti, private communication).

Date	R_h (AU)	v_h (km/s)	Δ (AU)	v_Δ (km/s)	Molecule	λ (cm^{-1})	Q (10^{25} mol/s)	M.R. %	Instrument
11 May 2008	1.17	-20.45	0.34	-10.47	H_2O	3455	356.4 ± 45.0	100	CRIRES
26 May 2008	1.01	-16.75	0.21	-8.05	H_2O	3455	645.2 ± 48.7	100	CRIRES
27 May 2008	0.99	-16.07	0.25	-7.82	H_2O	3455	759.8 ± 122.5	100	CRIRES
					CO	2160	33.4 ± 7.6	6.8 ± 1.5	
30 May 2008	0.97	-15.26	0.24	-7.04	H_2O	3455	1042.0 ± 139.8	100	CRIRES
					HCN	3290	5.2 ± 0.6	0.49 ± 0.06	
26-30 May 2008					C_2H_6	3000	13.7 ± 0.7	2.5 ± 0.2	CRIRES
mean					CH_3OH	2848	20.5 ± 4.2	2.7 ± 0.6	
01 Jul 2008	0.86	4.72	0.29	12.34	H_2O	3445	1382 ± 58	100	CRIRES
					CH_3OH	2844	33.2 ± 6.9	2.4 ± 0.5	
					C_2H_6	3000	30.4 ± 2.8	2.2 ± 0.2	

Table A.1: Comparison between C/2007 W1 mixing ratios measured in different times. Data are from this work and M. DiSanti, via private communication (paper in preparation).

Species	Mean ν (cm^{-1})	Q (10^{26}s^{-1})	Mixing Ratio (%)	T_{rot} (K)
11 May 2008				
H_2O	3445	35.64 ± 4.50	100	
26-30 May 2008				
H_2O (26May)	3445	65.42 ± 4.87	100	(88)
H_2O (27May)	2160	75.98 ± 12.25	100	(88)
CO (27 May)	2160	3.34 ± 0.76	6.8 ± 1.5	(88)
H_2O (30May)	3445	104.2 ± 13.98	100	88^{+2}_{-3}
HCN (30May)	3290	0.52 ± 0.06	0.49 ± 0.06	89^{+30}_{-18}
C_2H_2 (30 May)	3290	0.25 ± 0.05	0.24 ± 0.05	
C_2H_6 (mean)	3000	1.37 ± 0.07	2.5 ± 0.2	(88)
CH_3OH (mean)	2848	2.05 ± 0.42	2.7 ± 0.6	(88)
1 Jul 2008				
H_2O	3445	138.2 ± 5.8	100	80^{+6}_{-5}
C_2H_6	3000	3.04 ± 0.28	2.2 ± 0.2	(80)
CH_4	3000	2.62 ± 0.41	1.9 ± 0.3	(80)

Table A.2: The parent volatile composition of comet C/2007 W1 as measured with CRIRES/VLT. Except for HCN, molecular production rates, mixing ratios and rotational temperatures presented here, have been retrieved by Michael A. DiSanti (paper in preparation).

B   Ro-vibrational spectra of diatomic and linear molecules.

B.1   Rotational spectra of diatomic molecules and linear polyatomic molecules.

B.1.1   Rotational spectra in the rigid rotor approximation

A diatomic molecule can be considered as two point masses m_1 and m_2 connected by a rigid rod long R. In this approximation the molecule can rotate as a whole about an axis passing through the center of mass and perpendicular to the internuclear axis (rigid rotator approximation). This is the simplest model for a rotating molecule. The quantized rotational energy corresponding to a certain rotational level r can be calculated solving the Schroedinger equation related to the rigid rotor, and it is given by

$$E_r = \frac{h^2 J(J+1)}{8\pi^2 I},\tag{B.1}$$

where J is the rotational quantum number, that can assume integer values $1, 2, 3, \ldots$, and I is the moment of inertia associated to the molecule; for a diatomic molecule $I = \mu R^2$, where μ is the reduced mass and R the internuclear distance.

In the infrared spectral range it is common to express the same concept using wavenumbers, so that equation B.1 can be written as

$$F_J = \frac{E_r}{hc} = \frac{hJ(J+1)}{8c\pi^2 I} = BJ(J+1),\tag{B.2}$$

where the rotational constant $B = h/8c\pi^2 I$ has been introduced; F_J is called rotational term value.

According to classical electrodynamics the rotation of the molecule can produce radiation of light only if the corresponding dipole moment change; for a rigid rotator the change in dipole moment can be induced by the fact that the different masses have a different charge, or to the fact that a permanent dipole moment for these molecules lies in the direction perpendicular to rotational axis. In these cases, during the rotation the dipole moment change periodically with a frequency equal to the rotational frequency. It follows that pure rotational transitions are forbidden for homonuclear diatomic molecules, and in general for symmetric molecules, since their electric dipole moment is zero.

The rotational selection rules for the quantum number J are obtained evaluating the matrix elements R_x^{ul}, R_y^{ul} and R_z^{ul} of the dipole moment. It can be demonstrated that these

matrix elements are different from zero when the dipole moment of the molecule is not zero, and when $\Delta J = \pm 1$[1].

From the selection rules it follows also that the frequency of a transition between the rotational levels J_u and J_l can be expressed as

$$\nu = F(J_u) - F(J_l) = F(J + 1) - F(J) = 2B(J + 1). \tag{B.3}$$

Thus the spectrum of the simple rigid rotator consists of a series of equidistant lines, separated by a distance equal to $2B$.

B.1.2   Population of the levels and intensity of the lines

The population of the rotational energy levels can be expressed in terms of a Boltzmann distribution:

$$\frac{N_J}{N_0} = (2J + 1)e^{-E_r/kT}, \tag{B.4}$$

where N_J is the population of the considered level, N_0 is the population of the level for $J = 0$ and the factor $(2J + 1)$ represents the degeneracy of each rotational energy level, in the absence of an electric or magnetic field.

The intensities of pure rotational transitions are proportional to the fraction of the total number of molecules N which occupies each rotational level:

$$\frac{N_J}{N} = \frac{(2J + 1)e^{-E_r/kT}}{Q_r}; \tag{B.5}$$

Q_r is the rotational partition function given by

$$Q_r = \sum_i g_i e^{(-E_r)_i/kT}, \tag{B.6}$$

where the sum runs over all occupied rotational levels; g_i represent the degeneracy of the i level.

B.1.3   Centrifugal distortion

The bond between the atoms that compose the molecule can stretch and contract in a vibrational motion, and centrifugal distortions associated with the rotation of the molecule has to be introduced. Classically, the effect related to the centrifugal distortion increases for increasing rotational speed and therefore with high J.

The rotational term values comprising the centrifugal effect are given by

$$F_J = BJ(J + 1) + DJ^2(J + 1)^2. \tag{B.7}$$

D is called centrifugal distortion constant and it is always positive for diatomic molecules; it depends on the vibrational frequency ω of the molecule and on the rotational constant ($D = 4B^3/\omega^2$). The corresponding frequency of the transition between J_u and J_l are:

---

[1]In addition to this selection rule, one should take into account also spin and magnetic quantum number selection rules. See Herzberg (1939) for a detailed discussion.

$$v = F(J_u) - F(J_l) = F(J + 1) - F(J) = 2B(J + 1) - 4DJ^2(J + 1)^2. \qquad \text{(B.8)}$$

When very accurate measurements are taken, higher approximation terms that take into account other effects (like for example the anharmonicity of the potential energy of the molecule) should be used, and equations B.7 and B.8 can be written as:

$$F_J = BJ(J + 1) + DJ^2(J + 1)^2 + HJ^3(J + 1)^3 + \ldots \qquad \text{(B.9)}$$

$$v = F(J_u) - F(J_l) = F(J + 1) - F(J) = 2B(J + 1) - 4DJ^2(J + 1)^2 + 8HJ^3(J + 1)^3 \qquad \text{(B.10)}$$

B.2   Rotational and vibrational spectra of diatomic and linear molecules

B.2.1   Vibrational spectra in the simple harmonic oscillator approximation

The simplest model for a diatomic vibrating molecule is made considering the atoms as two particles of reduced mass μ, connected by a spring of force constant k. The corresponding energy levels associated to the vibrational transition of the molecule will be given by:

$$E_V = hv\left(V + \frac{1}{2}\right), \qquad \text{(B.11)}$$

where

$$v = \frac{1}{2\pi}\sqrt{\frac{k}{\mu}} \qquad \text{(B.12)}$$

is the classical vibrational frequency and the vibrational quantum number V can take the values $0, 1, 2 \ldots$.

In analogy with the rotational terms, it is possible to define vibrational terms as

$$G(V) = \omega\left(V + \frac{1}{2}\right), \qquad \text{(B.13)}$$

where ω is the classical vibrational wavenumber; this is an approximation, and also in this case, for very accurate measurements, second and higher orders corrections should be introduced.

The dipole moment of a molecule will change, if the internuclear distance changes, with a frequency scale equal to the one of the mechanical vibration. Similarly to the case of the rotational spectra, we can define this frequency as:

$$v = G(V_u) - G(V_l), \qquad \text{(B.14)}$$

where V_u and V_l are the vibrational quantum numbers of the upper and lower state, respectively.

For the oscillator, the matrix elements R_x^{ul}, R_y^{ul} and R_z^{ul}, associated to the dipole moment, are zero except when $\Delta V = V_u - V_l = \pm 1$: this is the selection rule for the vibrational quantum number of the harmonic oscillator.

B.2.2 Vibration-rotation spectroscopy

When a molecule has both vibrational and rotational energy, that is always the case for a vibrational transitions, the total term values S are given by the sum of the rotational terms $F(J)$ and the vibrational terms $G(V)$:

$$S = G(V) + F(J) = BJ(J + 1) + DJ^2(J + 1)^2 + HJ^3(J + 1)^3 + \omega(V + \frac{1}{2}) + \ldots \quad \text{(B.15)}$$

For each transition between two vibrational states v_u and v_l, different rotational transitions, following the selection rules $\Delta J = \pm 1$, are possible. As a consequence, the spectra of a ro-vibrational transition will show a R-branch (for $\Delta J = 1$) and a P-branch (for $\Delta J = -1$). Usually each of these transitions is labeled with $R(J)$ or $P(J)$, where J represents the J-value for the rotational level in the lower vibrational state. The fact that the transition corresponding to $\Delta J = 0$ is forbidden, means that the $P(0)$ line cannot exist, i.e. the pure vibrational transition is not observed. The position at which this would occur is called band center. Exceptions to this rule are molecules that have an electronic angular momentum in the ground electronic state. In this cases, for the transitions corresponding to $\Delta J = 0$ (the transition $J = 0$ to $J = 0$ is anyway forbidden) a Q-Branch will be visible.

The intensity distribution of the rotational transitions in a ro-vibrational transition is governed principally by the Boltzmann population distribution among the initial states of the transition:

$$\frac{N_{J_l}}{N} = \frac{hcB_l}{kT}(2J + 1)e^{-hcB_l J_l(J_l+1)/kT}, \quad \text{(B.16)}$$

where N_{J_l} is the number of molecules with quantum number J_l, N is the total number of molecules, (kT/hcB_l) is the rotational partition function (defined as in B.6). For bands showing only P and R branches the intensity distribution I_e in vibration-rotation bands observed in emission is given by

$$I_e = C_e v^4 \frac{hcB_u}{kT}(J_u + J_l + 1)e^{-hcB_u J_u(J_u+1)/kT}, \quad \text{(B.17)}$$

where C_e is a constant depending on the absolute intensity of the vibrational transition.

B.3 Emission and absorption of radiation

When a molecule interacts with electromagnetic radiation it can undergo in a transition from the initial state l, with corresponding energy E_l, to the new state u, with corresponding energy E_u, if the electromagnetic radiation has wavenumber $v = (E_u - E_l)/hc$.

The interaction of the molecule with the electromagnetic radiation can be described through the matrix elements associated to the dipole moment of the molecule[2].

For spontaneous emission, the intensity of the light emitted by the molecule for a transition from a higher to a lower energy state, is given by

$$I_{\text{em}}^{ul} = N_u h c \nu_{ul} A_{ul}, \tag{B.18}$$

where N_u is the number of atoms in the initial state, ν_{ul} is the frequency of the transition and A_{ul} is the Einstein transition probability of spontaneous emission. According to quantum mechanics, this probability is related to the matrix elements as:

$$A_{ul} = \frac{64\pi\nu_{ul}^3}{3h} \left|R^{ul}\right|^2 . \tag{B.19}$$

The intensity for absorption line is instead defined as:

$$I_{\text{abs}}^{ul} = I_0 N_l h c \nu_{ul} \Delta x B_{lu}, \tag{B.20}$$

where Δx is the thickness of the absorbing layer, N_l is the number of atoms (per cm^3) in the initial lower state, I_0 is the intensity of the incident radiation, and B_{lu} is the Einstein transition probability of the absorption.

The Einstein transition probability for absorption is also related to the matrix elements

$$B_{lu} = \frac{8\pi^3}{3h^2c} \left|R^{ul}\right|^2 , \tag{B.21}$$

and this leads to a simple relation between the two Einstein coefficients:

$$B_{lu} = \frac{1}{8\pi h c \nu^3} A_{ul}. \tag{B.22}$$

---

[2]If for a given transition the matrix elements associated to the dipole are zero, the corresponding transition may still occur if a non zero quadrupole moment is present.

C High resolution grating spectrographs

C.1 Diffraction gratings

In spectroscopy gratings are widely used since they have almost linear dispersion and low losses of light due to absorption. A grating consist of a series of equally separated and parallel grooves or slits, the width of each being comparable to the wavelength of the radiation to be dispersed. If a beam of light falls on the surface of the grating, the radiation is diffracted into discrete directions, in several spectra; the resulting distribution of light can be described by the well known Fraunhofer's grating equation:

$$n\lambda = d\left(\sin\alpha + \sin\beta\right), \tag{C.1}$$

where n is an integer that represents the order of the observed image, d is the spacing of the parallel grooves, α is the angle of the incident radiation and β the angle of the refracted light, measured from the normal to the grating surface[1]; the angle of the refracted light is thus wavelength dependent (see Fig. C.1).

For a particular wavelength λ, all values of n for which $|n\lambda/d| < 2$ correspond to propagating (rather than evanescent) diffraction orders. The special case $n = 0$ leads to the law of reflection $\beta = -\alpha$.

The different integers n for which the grating equation is satisfied are called diffraction orders, and for a particular groove spacing d, wavelength λ and incidence angle α, the grating equation is generally satisfied by more than one diffraction angle β: it is evident from the grating equation that light of wavelength λ diffracted by a grating along direction β will be accompanied by integral fractions $\lambda/2$, $\lambda/3$. For $\lambda/d << 1$, a large number of diffracted orders will exist, and the respective spectra will overlap (see Fig. C.2). There are some important quantities that characterize a grating.

Angular dispersion: it is a measure of the separation between diffracted light of different wavelengths. Fine spectral details will be more easily identify by gratings with a

---

[1]If the incidence of the beam is not perpendicular to the plane of the grating surface and the plane of the grooves, the equation of the grating becomes

$$n\lambda = d\cos\gamma\left(\sin\alpha + \sin\beta\right),$$

where γ is the angle of incidence of the beam with respect to the normal plane to the grating and the grooves. This kind of configuration can be used in some Echelle spectrographs, but in general the incident light is perpendicular to the grating plane so that $\gamma = 0$ and the grating equation reduce simply to equation C.1.
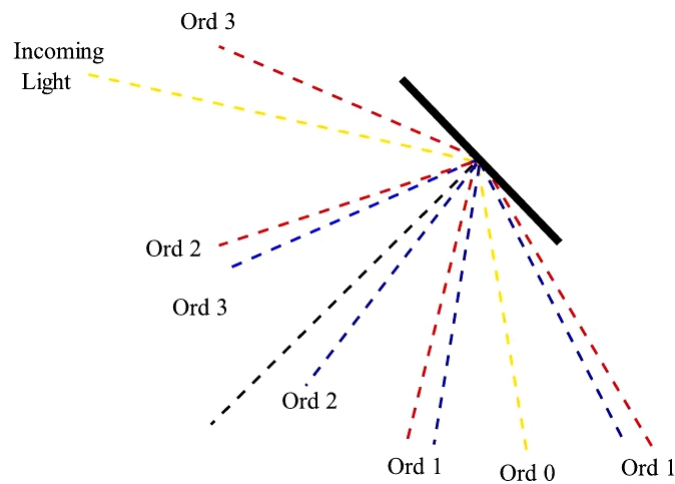
Figure C.1: Schematic representation of the distribution of the diffracted light by a grating (Source: http://gratings.newport.com/library/handbook/chapter2.asp).
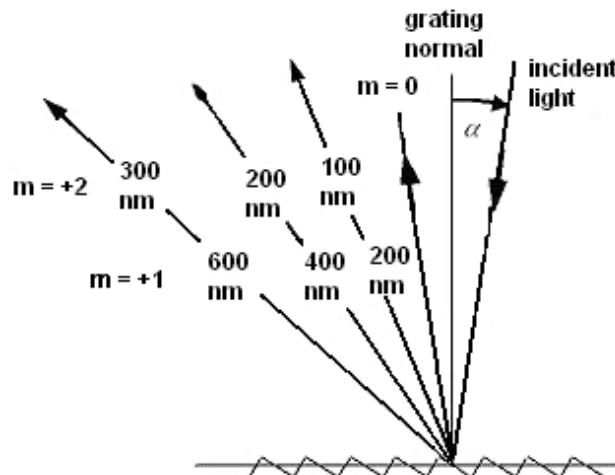
Figure C.2: Overlapping of spectral orders. The light of wavelengths 100, 200 and 300 nm in the second order is diffracted in the same direction as the light of wavelengths 200, 400 and 600 nm in the first order (Source: http://gratings.newport.com/library/handbook/chapter2.asp).

high dispersion. It can be calculated by holding α constant and differentiating the grating equation respect to β:

$$D = \frac{d\beta}{d\lambda} = \frac{n}{d}\frac{1}{\cos\beta}. \qquad (C.2)$$

Angular dispersion in a given order n, is a function of d and β; high dispersion can be achieved either by choosing a grating with a high groove frequency, or by using a coarse grating in high diffraction order.

   Resolving power: the ability to observe two close lying wavelengths λ and $\lambda + \delta\lambda$ separated, is a measure of what is called resolving power. The theoretical resolving power of a grating is simply given by the product between the order and the number of grooves N in the grating:

118
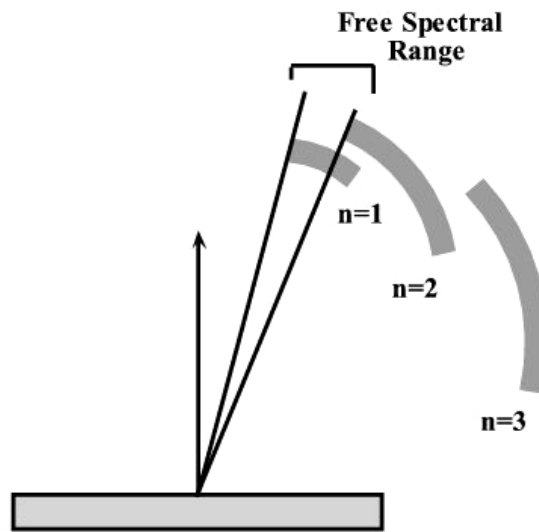
Figure C.3: Schematic representation of the free spectral range.

$$R = \frac{\lambda}{d\lambda} = nN. \tag{C.3}$$

Note that the resolving power should not be confused with the resolution, $d\lambda$, which is instead the smallest separation of two monochromatic spectral lines that can just be resolved as two by a given spectrograph (see below). High resolving power can be obtained using a grating with a high number of grooves, i.e. a long grating; moreover, the grating should be used at high orders. This last option is favorable since in this way both the resolving power and the dispersion can be increased, even using a smaller, and thus more practical, grating.

Spectral resolution: while resolving power can be considered a characteristic of the grating and the angles at which it is used, the ability to resolve two wavelengths λ_1 and $\lambda_2 = \lambda_1 + d\lambda$ generally depends not only on the grating but on the entrance and exit slits, the possible aberrations, and the magnification of the images. The minimum wavelength difference $d\lambda$ that a system can distinguish is considered more relevant than its resolving power, since it takes into account the image effects of the system. While resolving power is a dimensionless quantity, resolution has spectral units.

Free spectral range: light of several wavelengths, each in a different order, will be diffracted by the grating along the same direction: light of wavelength λ in order n will be diffracted along the same direction of light of wavelength $\lambda/2$ in order 2n, etc. The range of wavelengths, in a given spectral order, for which superposition of light from adjacent orders does not occur is called free spectral range (see Fig. C.3). The free spectral range can be calculated considering that $n\lambda' = (n + 1)\lambda$ and then

$$F_\lambda = \Delta\lambda = \frac{\lambda}{n}. \tag{C.4}$$

Gratings with small F_λ will suffer of superposition of orders and thus they will need to be paired up with other optical parts that work as cross dispersers and separate the orders, or with filters.
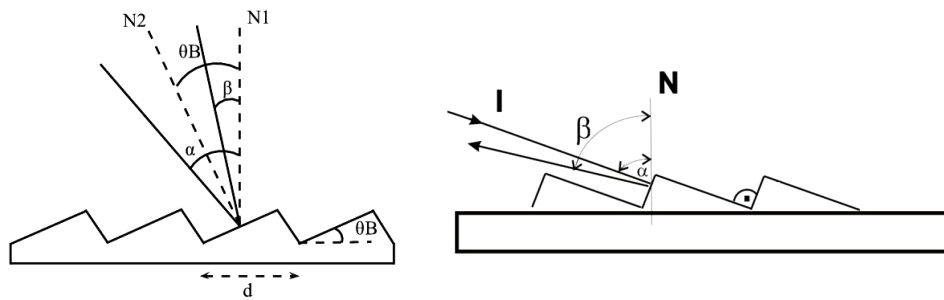
Figure C.4: A schematic view of a Blazed grating (on the left) and an Echelle grating (on the right).

Efficiency: the efficiency for a grating is defined as the amount of the incident flux that is diffracted into a given order. It depends on many factors, like the grooves frequency, the shape of the grooves and the grating material.

Blazed and Echelle gratings

The reflective surface of a grating can be tilted (blazed) to scatter the majority of the incoming light into the preferred direction of interest, into a specific diffraction order (see Fig. C.4); the maximum efficiency for these kind of gratings can be obtained for high orders, where there is high dispersion and high resolving power; in this respect, this kind of grating is the best for high resolution spectroscopy.

Blazed gratings suffer from order overlapping: if the grating operates in multiple wavelengths, it is possible that longer wavelengths of a higher order might overlap with the next order(s) of a shorter wavelength; usually, this is an unwanted side effect and it can be reduced using a second, perpendicularly mounted dispersive element or filters.

If the incidence of the light occurs on the small facet instead of the long one, the result is a high blaze angle grating; this is the principle by which **Echelle gratings** work (see Fig. C.4). Echelle gratings are mostly efficient at very high orders, and they can thus reach very high dispersion and resolving power. As seen before, also Echelle gratings will suffer from orders overlapping. Since this overlap is not directly useful, a second, perpendicularly mounted dispersive element (a grating or a prism) is inserted as an "order separator" or "cross disperser" into the beam path. Hence the spectrum consists of stripes with different, but slightly overlapping, wavelength ranges that run across the imaging plane, usually in an oblique pattern (see Fig. C.5).

The angular dispersion of an Echelle grating may be 5-10 times larger than the one for a normal grating, even if the Echelle is coarsely ruled (i.e. even if it has fewer grooves per mm) that makes these instruments the best choice for high resolution spectroscopy.

C.2   Grating spectrographs

A spectrograph is an instrument that receives light from a source, disperses the light according to its wavelength into a spectrum, and focuses the spectrum onto a detector, which records the spectral image

Echelle Spectrum of QSO HE2217-2818 (330 - 450 nm)   (VLT KUEYEN + UVES)

ESO PR Photo 37d/99 (5 October 1999)   © European Southern Observatory
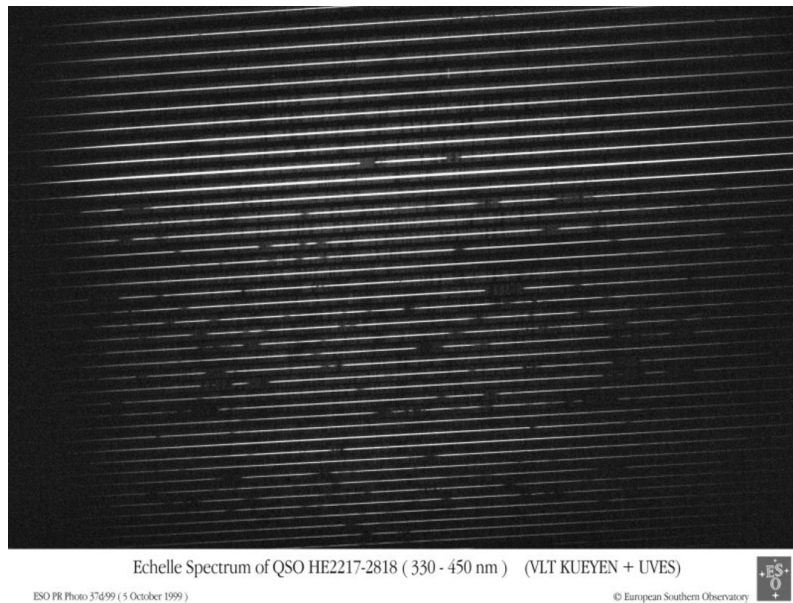
Figure C.5: Typical image pattern from an Echelle spectrometer. The typical tilted pattern is due to the optics of the instrument. (Source: https//www.eso.org/gallery/d/19374-2/phot-37d-99-hires.jpg).
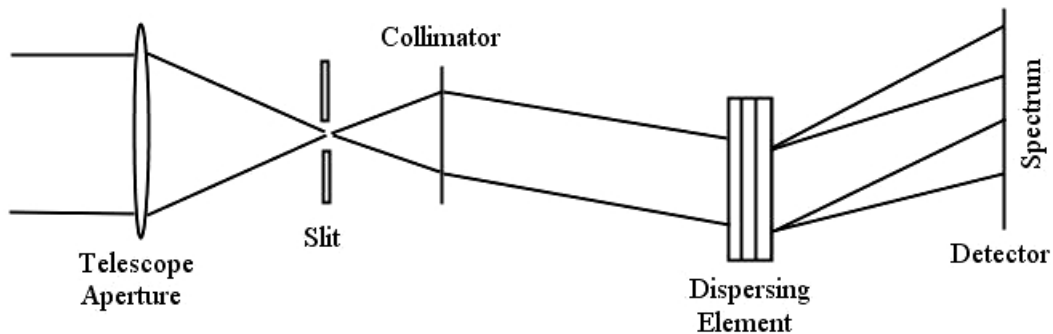
Figure C.6: General layout of an astronomical slit spectrograph

In figure C.6 a simple schematic diagram for a typical astronomical spectrograph is presented with its main components: the entrance slit limits the spatial distribution of the light entering in the spectrograph, and helps to define the light cone required to illuminate the system; the collimator, usually a mirror or a lens, assures the light will hit the dispersing element in a parallel collimated fashion; the dispersing element, a prism or a grating, disperses the incoming light while the focusing optical element collects the light coming from the dispersing element in the detector area; finally, the detector records the image. Similarly to the diffraction gratings, it is possible to define some important quantities that characterize a grating spectrometer.

Angular and linear dispersion: the angular dispersion is directly given by the dispersing element. If the dispersing element is associated with other optical elements, the linear dispersion is defined as $dl/d\lambda$ where dl is the linear separation on a focal surface between two rays of wavelength difference equal to $d\lambda$ (see Fig. C.7).

121
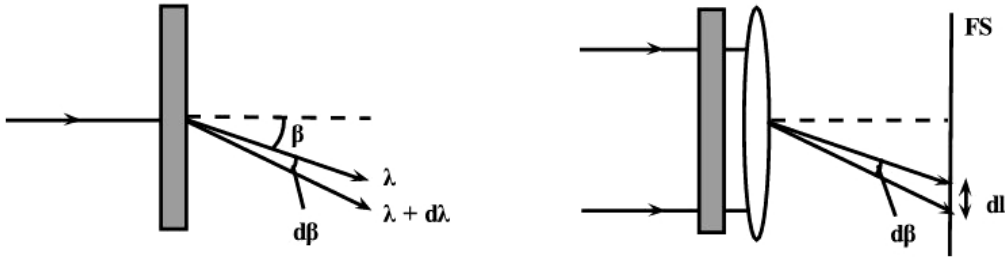
Figure C.7: Angular dispersion (left) and linear dispersion (right) for a spectrometer.

Resolving power: the resolving power of the instrument is influenced by all the optics that composes it, and it depends on the width of the slit: two main expressions for the resolving power of the spectrograph can be derived:

$$R_{\text{slit}} = \frac{\lambda}{\delta\lambda} = \frac{f_{\text{coll}}\,(\sin\alpha + \sin\beta)}{w\cos\alpha} \tag{C.5}$$

and

$$R_{\text{slit}} = \frac{\lambda}{\delta\lambda} = \frac{A_{\text{coll}}f_{\text{tel}}}{wD}\frac{(\sin\alpha + \sin\beta)}{\cos\alpha} \tag{C.6}$$

In case of blazed configuration, a third formula for the slit limited resolving power can be retrieved:

$$R_{\text{slit}} = \frac{\lambda}{\delta\lambda} = \frac{2L\sin\theta_B}{\theta_s D}. \tag{C.7}$$

In these three formulas, f_{coll} is the collimator focal length, w is the width of the slit, α is the angle of incidence, β is the angle of diffraction, A_{coll} is the beam diameter before the grating, D is the telescope aperture, θ_s is the angular size of the slit in radians projected onto the sky.

From the first two expressions it becomes clear that high resolving power can be obtained with narrow slits and high blaze angle gratings, i.e. with Echelle gratings. In the last two formulas, there is an inverse dependence from the diameter of the telescope: big telescopes can collect more light, but the spectrograph is then less efficient.

Throughput: throughput can be defined as the fraction of the photons in the focal plane of the telescope that are recorded by the detector. Throughput is then a measure of the spectrograph efficiency in not wasting the light that it receives. Usually the product between the throughput and the resolving power define the Figure of Merit of the spectrograph.

D Cometary volatile ices measured in the infrared

Hereafter, production rates Q and mixing ratios M.R., relative to different observed comets are tabulated. Comets are divided in three groups, according to their dynamical properties. For each comet, the date of the observations, together with the approximate orbital parameters for the observing period, are indicated. For each instrument, indicated in the last column, the (approximate) wavelengths used are given. References are annotated at the bottom of the pages. The values presented here, were used to compare the obtained results for comet 8P/Tuttle and C/2007 W1 (Boattini), with other comets already observed in the past (see section 6.1.1.1).

Chemical classes were defined as followed:

- For each comet, the weighted mean for the listed mixing ratios, relative to a certain specie, have been calculated in the following way:

$$\bar{x} = \frac{\sum_i x_i w_i}{\sum_i w_i}, \tag{D.1}$$

  where x_i are the measured values and w_i are the weights, calculated as $1/dx_i^2$, with dx_i the error associated to the measure. The relative error associated to the weighted mean have been calculated as $\sigma = \sqrt{\sum_i (1/w_i)}$.

- Once the weighted mean are calculated, we defined the organic normal range for a certain species, using a simple arithmetic mean; if the standard deviation of the values for each comet is within 1σ interval centered on the mean value, then the comet is defined as organic normal.

- We defined the organic enriched range and organic depleted range, values higher and lower, respectively, with respect to the organic normal range.

- When the deviation from the mean value is more than 3σ, we refer the values as super enriched or super depleted.

- The final retrieved values are listed in tables 1.4, 6.5 and 6.14.

D.1 Oort cloud - long period comets

C/2004 Q2 (Machholz)

Date	R_h (AU)	v_h (km/s)	Δ (AU)	v_Δ (km/s)	Molecule	λ (cm^{-1})	Q (10^{25} mol/s)	M.R. %	Instrument
28 Nov 2004	1.49	-15.20	0.65	-21.70	H_2O	3429	15350 ± 690	100	NIRSPEC[1]
					C_2H_6	2982	86.2 ± 3.5	0.56 ± 0.03	
					CH_3OH	2852	311.1 ± 12.1	2.03 ± 0.11	
					CH_4	3037	192.1 ± 16.5	1.25 ± 0.12	
					H_2O	3429	14350 ± 730	100	
					HCN	3297	20.2 ± 2.0	0.14 ± 0.02	
					C_2H_2	3297	< 9.1	< 0.06	
					H_2CO	3037	14.5 ± 4.5	0.10 ± 0.03	
					CH_4	3037	180.8 ± 3.6	1.26 ± 0.10	
29 Nov 2004	1.48	-15.00	0.64	-21.50	H_2O	2148	12530 ± 1530	100	NIRSPEC[1]
					CO	2148	634.6 ± 27.7	5.07 ± 0.51	
19 Jan 2005	1.21	-2.00	0.39	10.90	H_2O	3429	27270 ± 1140	100	NIRSPEC[1]
					C_2H_6	2982	148.9 ± 8.5	0.55 ± 0.04	
					CH_3OH	2852	619.7 ± 21.2	2.27 ± 0.12	
					CH_4	3037	390.5 ± 24.1	1.43 ± 0.10	
					H_2O	3429	27550 ± 750	100	
					HCN	3297	41.2 ± 0.7	0.15 ± 0.05	
					C_2H_2	3297	23.1 ± 1.2	0.08 ± 0.01	
					H_2CO	3037	33.8 ± 3.5	0.12 ± 0.02	
					CH_4	3037	425.0 ± 12.0	1.54 ± 0.06	
30 Jan 2005	1.21	1.91	0.48	15.73	H_2O	3429	34200 ± 19000	100	NIRSPEC[2]
					HCN	3297	55.3 ± 3.8	0.16 ± 0.01	
					C_2H_6	2982	146 ± 20	0.43 ± 0.06	
					C_2H_2	3297	19.4 ± 1.4	0.06 ± 0.01	
					CH_4	3037	343 ± 19	1.0 ± 0.1	
					CH_3OH	2852	401 ± 21	1.2 ± 0.1	
					H_2CO	3037	60.6 ± 4.6	0.18 ± 0.01	
					NH_3	3037	10.8 ± 4.8	0.32 ± 0.05	

C/1999 H1 (Lee)

Date	R_h (AU)	v_h (km/s)	Δ (AU)	v_Δ (km/s)	Molecule	λ (cm^{-1})	Q (10^{25} mol/s)	M.R. %	Instrument
20 Aug 1999	1.062	23.58	1.36	-28.70	H_2O	3429	12600 ± 1000	100	NIRSPEC[3]
					CO	2148	230 ± 20	1.8 ± 0.2	
					CH_3OH	2852	270 ± 50	2.1 ± 0.5	
21 Aug 1999	1.076	23.74	1.348	-29.03	CH_3OH	2858	260 ± 50	2.1 ± 0.5	NIRSPEC[3]
					CH_4	3037	102 ± 5	0.81 ± 0.08	
					C_2H_6	2982	84 ± 5	0.67 ± 0.07	
					C_2H_2	3037	34 ± 3	0.27 ± 0.03	
					HCN	3297	29 ± 2	0.23 ± 0.02	
19-21 Aug 1999					H_2O	3429	14310 ± 1330	100	NIRSPEC[4]
					CH_3OH	2858	230 ± 20	1.6 ± 0.2	
					CH_4	3037	162 ± 32	1.13 ± 0.25	
					C_2H_2	3037	34 ± 3	0.24 ± 0.03	
					HCN	3297	29 ± 2	0.20 ± 0.02	

[1]Bonev et al. (2009)

[2]Kobayashi and Kawakita (2009)

[3]Mumma et al. (2001b)

[4]Dello Russo et al. (2006)

C/2000 WM 1 (Linear)

Date	R_h (AU)	v_h (km/s)	Δ (AU)	v_Δ (km/s)	Molecule	λ (cm^{-1})	Q (10^{25} mol/s)	M.R. %	Instrument
23 Nov 2001	1.36	-27.8	0.38	-24.13	H_2O	3429	2090.61 ± 164.59	100	NIRSPEC[5]
					C_2H_6	2982	10.77 ± 1.02	0.52 ± 0.05	
					CH_3OH	2852	31.06 ± 2.58	1.49 ± 0.20	
					H_2O	3429	2049.03 ± 155.29	100	
					H_2CO	3037	4.93 ± 1.15	0.24 ± 0.06	
					CH_4	3037	7.04 ± 0.44	0.34 ± 0.06	
					HCN	3297	2.58 ± 0.31	0.13 ± 0.02	
					C_2H_2	3297	< 0.95	< 0.05	
					H_2O	2148	1599.29 ± 266.85	100	
					CO	2148	< 22.32	< 1.4	
24 Nov 2001	1.34	-27.85	0.37	-22.17	H_2O	3429	2382.76 ± 307.07	100	NIRSPEC[5]
					C_2H_6	2982	9.47 ± 1.18	0.40 ± 0.04	
					CH_3OH	2852	25.74 ± 3.57	1.08 ± 0.13	
					H_2O	3429	2321.49 ± 130.83	100	
					H_2CO	3037	3.95 ± 1.67	0.17 ± 0.07	
					CH_4	3037	9.78 ± 0.63	0.42 ± 0.07	
					HCN	3297	3.47 ± 0.29	0.15 ± 0.01	
					C_2H_2	3297	< 1.90	< 0.08	
					H_2O	2148	2097.74 ± 294.06	100	
					CO	2148	< 11.26	< 0.54	
25 Nov 2001	1.32	-27.90	0.36	-20.03	H_2O	3429	2212.44 ± 280.97	100	NIRSPEC[5]
					C_2H_6	2982	12.30 ± 1.04	0.56 ± 0.06	
					CH_3OH	2852	28.38 ± 3.54	1.28 ± 0.19	
					H_2O	3429	1954.10 ± 75.52	100	
					H_2CO	3037	3.68 ± 1.06	0.19 ± 0.05	
					CH_4	3037	5.85 ± 0.97	0.30 ± 0.05	
					HCN	3297	2.85 ± 0.16	0.15 ± 0.01	
					C_2H_2	3297	< 1.03	< 0.05	
					H_2O	2148	1770.70 ± 140.93	100	
					CO	2148	9.19 ± 1.94	0.52 ± 0.12	

C/2006 P1 (McNaught)

Date	R_h (AU)	v_h (km/s)	Δ (AU)	v_Δ (km/s)	Molecule	λ (cm^{-1})	Q (10^{25} mol/s)	M.R. %	Instrument
26 Jan 2007	0.53	47.80	1.03	38.72	H_2O	3452.5	1400 ± 330	100	CSHELL[6]
27 Jan 2007	0.53	47.13	1.05	38.21	H_2O	2146.2	1960 ± 190	100	CSHELL[6]
					CO	2146.2	28 ± 2.3	1.45 ± 0.18	
					CH_4	3028.4	5.2 ± 0.8	0.26 ± 0.05	
					C_2H_6	2985.8	7.1 ± 0.6	0.36 ± 0.05	
					C_2H_2	3302.1	7.6 ± 1.6	0.39 ± 0.09	
					HCN	3333.9	3.8 ± 0.6	0.19 ± 0.03	
					NH_3	3333.9	25.8 ± 3.9	1.32 ± 0.24	
28 Jan 2007	0.54	46.48	1.05	38.25	H_2CO	2782.7	9.5 ± 1.6	0.48 ± 0.09	CSHELL[6]

---

[5]Radeva et al. Icarus, 2009, In press.
[6]Dello Russo et al. (2009b)

C/2001 A2 (LINEAR)

Date	R_h (AU)	v_h (km/s)	Δ (AU)	v_Δ (km/s)	Molecule	λ (cm^{-1})	Q (10^{25} mol/s)	M.R. %	Instrument
09 Jul 2001	1.16	22.40	0.28	11.50	H_2O	3429	3770 ± 340	100	NIRSPEC[7]
					C_2H_6	2982	63 ± 6	1.67 ± 0.16	
					C_2H_2	3297	18 ± 5	0.48 ± 0.13	
					HCN	3297	21 ± 2	0.56 ± 0.05	
					CH_4	3037	45 ± 4	1.19 ± 0.11	
					CH_3OH	2852	145 ± 4	3.85 ± 0.10	
					H_2CO	3037	8.9 ± 0.9	0.24 ± 0.02	
10 Jul 2001	1.17	22.51	0.28	12.12	H_2O	3429	4300 ± 370	100	NIRSPEC[7]
					C_2H_6	2982	64 ± 6	1.45 ± 0.14	
					C_2H_2	3297	14 ± 3	0.32 ± 0.07	
					HCN	3297	19 ± 1	0.44 ± 0.02	
					CH_4	3037	65 ± 5	1.51 ± 0.12	
					CO	2148	166 ± 44	3.86 ± 1.02	
					CH_3OH	2852	120 ± 10	2.76 ± 0.23	
					H_2CO	3037	2.1 ± 1.1	0.05 ± 0.02	
04 Aug 2001	1.51	23.84	0.58	25.93	H_2O	3429	1090 ± 170	100	NIRSPEC[7]
					HCN	3297	5 ± 1	0.46 ± 0.09	
					CH_4	3037	31 ± 2	2.84 ± 0.18	
					H_2CO	3037	1.9 ± 1.6	0.17 ± 0.15	
05 Aug 2001	1.59	23.85	0.59	26.63	H_2O	3429	620 ± 140	100	NIRSPEC[7]
					C_2H_6	2982	14 ± 2	2.26 ± 0.32	
					HCN	3297	5 ± 1	0.81 ± 0.16	
					CH_4	3037	17 ± 2	2.74 ± 0.32	

C/1996 B2 (Hyakutake)

Date	R_h (AU)	v_h (km/s)	Δ (AU)	v_Δ (km/s)	Molecule	λ (cm^{-1})	Q (10^{25} mol/s)	M.R. %	Instrument
23 Mar 1996	1.08	-35.95	0.12	-28.55	H_2O	5084	20000 ± 2300	100	CSHELL[8]
24 Mar 1996	1.06	-36.25	0.10	-12.23	H_2O	5084	25400 ± 2500	100	CSHELL[9]
					HCN		45.0 ± 8.1	0.18 ± 0.04	CSHELL[10]
					C_2H_6	2985	182 ± 31	0.72 ± 0.14	CSHELL[8]
					CO	2152	5110 ± 250	17 ± 2	
					CH_4		202 ± 44	0.80 ± 0.19	CSH.+NIR.[11]
10 Apr 1996	0.67	-41.65	0.55	55.66	C_2H_6	2985	220 ± 37	0.56 ± 0.10	CSHELL[8]
					H_2O	5084	41700 ± 420	100	
					CO	2152	6080 ± 570	14.6 ± 2.0	
					CH_4		484 ± 38	0.72 ± 0.16	CSH.+NIR.[11]
12 Apr 1996	0.64	-42.11	0.59	56.55	C_2H_6	2985	237 ± 19	0.59 ± 0.13	CSHELL[8]
					H_2O	5084	39900 ± 7600	100	
					CO	2152	6220 ± 490	15.6 ± 3.2	
					CH_4		364.3 ± 75.7	0.83 ± 0.18	CSH.+NIR.[11]

[7]Gibb et al. (2007)

[8]DiSanti et al. (2003)

[9]Mumma et al. (1996)

[10]Magee-Sauer et al. (2002b)

[11]Gibb et al. (2003)

C/1995 O1 (Hale Bopp)

Date	R_h (AU)	v_h (km/s)	Δ (AU)	v_Δ (km/s)	Molecule	λ (cm^{-1})	Q (10^{25} mol/s)	M.R. %	Instrument
21 Jan 1997	1.49	-21.40	2.20	-33.15	C_2H_6	2987	2150 ± 470	0.54 ± 0.12	CSHELL[12]
					H_2O	2154	400000 ± 39000	100	
					CO	2160	53200 ± 3000	13.1 ± 1.4	CSHELL[13]
23 Feb 1997	1.12	-16.96	1.57	-29.66	CO	2160	88300 ± 7500	11.7 ± 0.8	CSHELL[9]
24 Feb 1997	1.11	-16.68	1.56	-29.04	C_2H_6	2987	5000 ± 420	0.56 ± 0.05	CSHELL[8]
					H_2O	2154	889000 ± 89000	100	
					C_2H_2	2987	3400 ± 600	0.38 ± 0.07	
					CH_4	2987	8370 ± 1530	0.94 ± 0.17	CSHELL[14]
					HCN	3300	2390 ± 200	0.27 ± 0.04	CSHELL[15]
01 Mar 1997	1.06	-15.21	1.48	-25.47	CO	2160	95800 ± 5700	13.1 ± 0.5	CSHELL[9]
06 Apr 1997	0.92	3.06	1.40	18.67	C_2H_6	2987	7050 ± 710	0.66 ± 0.09	CSHELL[8]
					H_2O	2154	1069000 ± 107000	100	
					C_2H_2	2987	3400 ± 600	0.21 ± 0.08	
06 Apr 1997	0.92	3.06	1.40	18.67	HCN	3300	5620 ± 540	0.53 ± 0.07	CSHELL[11]
08 Apr 1997	0.92	4.27	1.42	20.59	C_2H_6	2987	5630 ± 480	0.60 ± 0.08	CSHELL[8]
					H_2O	2154	934000 ± 93000	100	
09 Apr 1997	0.92	4.83	1.43	21.43	C_2H_6	2987	5990 ± 720	0.64 ± 0.09	CSHELL[8]
					H_2O	2154	933000 ± 54000	100	
09 Apr 1997	0.92	4.83	1.43	21.43	CO	2160	120600 ± 13500	14.8 ± 1.2	CSHELL[9]
10 Apr 1997	0.92	5.41	1.44	22.21	C_2H_6	2987	6280 ± 630	0.63 ± 0.07	CSHELL[8]
					H_2O	2154	999000 ± 38000	100	
16 Apr 1997	0.95	8.69	1.53	26.16	CO	2160	116100 ± 20400	13.9 ± 1.3	CSHELL[9]
29 Apr 1997	1.04	14.37	1.74	29.99	HCN	3300	3090 ± 130	0.46 ± 0.03	CSHELL[11]
30 Apr 1997	1.05	14.39	1.74	29.97	C_2H_6	2987	6710 ± 750	0.99 ± 0.12	CSHELL[8]
					H_2O	2154	667000 ± 33000	100	
					C_2H_2	2987	2400 ± 200	0.28 ± 0.04	
					CO	2160	97400 ± 10000	15.0 ± 1.5	CSHELL[9]
					CH_4	2987	9635 ± 1876	1.42 ± 0.28	CSHELL[10]
01 May 1997	1.06	15.05	1.77	30.09	C_2H_6	2987	5030 ± 650	0.68 ± 0.09	CSHELL[8]
					H_2O	2154	743000 ± 41000	100	
					C_2H_2	2987	1600 ± 700	0.31 ± 0.14	
					CO	2160	95700 ± 8700	14.9 ± 1.3	CSHELL[9]
					CH_4	2987	11180 ± 2020	1.50 ± 0.27	CSHELL[10]
					HCN	3300	2800 ± 360	0.38 ± 0.05	CSHELL[11]

---

[12] Dello Russo et al. (2001)

[13] DiSanti et al. (2001)

[14] Gibb et al. (2003)

[15] Magee-Sauer et al. (1999)

C/2006 M4 (Swan)

Date	R_h (AU)	v_h (km/s)	Δ (AU)	v_Δ (km/s)	Molecule	λ (cm^{-1})	Q (10^{25} mol/s)	M.R. %	Instrument
07 Nov 2006	1.09	21.38	1.11	27.92	C_2H_6	2985	86.1 ± 9.3	0.49 ± 0.05	CSHELL[16]
					H_2O	2152.5	17560 ± 1450	100	
					CO	2152.5	86.9 ± 37.6	0.49 ± 0.21	
09 Nov 2006	1.11	21.74	1.14	31.00	H_2O	2152.5	12800 ± 1260	100	CSHELL[16]
					CO	2152.5	64.7 ± 25.8	0.50 ± 0.20	
					CH_3OH	2844	433.0 ± 36.5	3.38 ± 0.28	
10 Nov 2006	1.12	21.90	1.17	32.40	H_2O	3452.3	14700 ± 580	100	CSHELL[16]
					CH_4	3041	1200 ± 13.6	0.82 ± 0.09	
					CH_3OH	2844	464 ± 109	3.16 ± 0.74	

C/2007 W1 (Boattini)

See table A.1, in appendix A.

C/1999 S4 (LINEAR)

Date	R_h (AU)	v_h (km/s)	Δ (AU)	v_Δ (km/s)	Molecule	λ (cm^{-1})	Q (10^{25} mol/s)	M.R. %	Instrument
03 Jul 2000	0.88	-16.37	0.90	-63.72	CO	2149.5	< 42	< 1.9	IRTF[17]
					H_2O	2149.5	2000 ± 600	100	
04 Jul 2000	0.87	-15.88	0.86	-63.64	C_2H_6	2981	< 6.8	< 0.3	IRTF[17]
					H_2O	2149.5	2300 ± 500	100	
					H_2O	3452	2100 ± 1100	100	
					CO	2149	< 42	< 1.9	
05 Jul 2000	0.86	-15.37	0.82	-63.42	C_2H_6	2981	< 5.6	< 0.08	IRTF[17]
					CH_4	3041	5.9 ± 1.3	0.09 ± 0.02	
					CO	2149	70 ± 20	0.94 ± 0.27	
					H_2O	2149	7460 ± 740	100	
09 Jul 2000	0.83	-13.07	0.68	-61.28	C_2H_6	2981	< 2.4	< 0.08	IRTF[17]
					H_2O	2149	3200 ± 700	100	
13 Jul 2000	0.80	-10.38	0.55	-54.77	C_2H_6	2981	8.13 ± 1.85	0.13 ± 0.02	IRTF[17]
					CH_3OH	2844	< 11	< 0.17	
					CH_4	3041	9.5 ± 1.4	0.15 ± 0.02	
					C_2H_2	3297	< 8.9	< 0.14	
					HCN	3297	6.1 ± 1.7	0.10 ± 0.03	
					H_2O	2149	4460 ± 720	100	
					CO	2149	20 ± 15	0.45 ± 0.34	

---

[16]DiSanti et al. (2009)
[17]Mumma et al. (2001a)

D.2   Halley type comets

8P/Tuttle

See table 6.6, in chapter 6.

1P/Halley

Molecule	M.R. %
From Mass spectrometry, GIOTTO, 1986[18]	
H_2O	100
CO	3.5
CO_2	3
H_2CO	< 0.4
CH_3OH	1.7
CH_4	< 1
C_2H_2	0.3
C_2H_6	0.4
HCN	0.2

153P/Ikeya-Zhang (C/2002 C1)

Date	R_h (AU)	v_h (km/s)	Δ (AU)	v_Δ (km/s)	Molecule	λ (cm^{-1})	Q (10^{25} mol/s)	M.R. %	Instrument
21 Mar 2002	0.51	5.40	0.76	-32.40	CH_4	3037	356.5 ± 71.2	0.54 ± 0.11	CSHELL[19]
					H_2O	3453	66000 ± 5000	100	
22 Mar 2002	0.51	7.48	0.74	-31.37	CH_4	3037	4390 ± 75	0.46 ± 0.10	CSHELL[19]
					H_2O	3453	21000 ± 3000	100	
					H_2O	3448	72300 ± 4600	100	CSHELL[20]
23 Mar 2002	0.516	9.07	0.742	-31.12	H_2O	3448	91400 ± 7200	100	CSHELL[20]
27 Mar 2002	0.549	14.04	0.661	-27.6	H_2O	3448	59700 ± 8000	100	CSHELL[20]
10 Apr 2002	0.732	27.05	0.490	-15.48	H_2O	3448	19900 ± 1500	100	CSHELL[20]
11 Apr 2002	0.749	27.39	0.480	-14.30	H_2O	3448	26300 ± 2300	100	CSHELL[20]
12 Apr 2002	0.764	27.71	0.473	-13.63	H_2O	3448	28300 ± 3500	100	CSHELL[20]
13 Apr 2002	0.779	28.01	0.466	-13.12	C_2H_2	3287.76	37 ± 8	0.18 ± 0.05	CSHELL[21]
					HCN	3302.55	38 ± 5	0.18 ± 0.04	
					C_2H_6	2983	130 ± 20	0.62 ± 0.09	CSHELL[22]
					H_2O	3453	21000 ± 3000	100	
21 Mar - 13 Apr 2002					CO	2170	1010 ± 130	4.7 ± 0.8	CSHELL[23]
					H_2CO	2781	180 ± 8	0.62 ± 0.18	
					CH_3OH	2844	520 ± 80	2.5 ± 0.5	

[18] Eberhardt (1999)

[19] Gibb et al. (2003)

[20] Dello Russo et al. (2004)

[21] Magee-Sauer et al. (2002a)

[22] Dello Russo et al. (2002)

[23] DiSanti et al. (2002)

D.3   Jupiter family comets

21P/Giacobini- Zinner[24]

Date	R_h (AU)	v_h (km/s)	Δ (AU)	v_Δ (km/s)	Molecule	λ (cm^{-1})	Q (10^{25} mol/s)	M.R. %	Instrument
2-10 Oct 1998	≈ 1.22	≈ -11.67	≈ 1.05	≈ -9.5	CO	2147.08	330 ± 60	10.31 ± 1.87	CSHELL[25]
					C_2H_6	2986.75	7.0 ± 1.5	0.22 ± 0.05	
					H_2O	2147.08	3200 ± 1700	100	
25 Oct 1998	1.10	-8.37	0.95	-8.66	C_2H_6	2986.75	≤ 1.5	$\leq 0.05 - 0.08$	CSHELL[26]
26 Oct 1998	1.09	-8.11	0.94	-8.53	CO	2147.08	64	$\leq 2.1 - 3.2$	CSHELL[26]
					CO	2150.86	68	$\leq 2.3 - 3.4$	
					H_2O	2148.19	5300 ± 2600	100	
					H_2O	2151.19	1200 ± 600	100	
27 Oct 1998	1.09	-7.85	0.94	-8.40	H_2O	2002.99	4300 ± 2200	100	CSHELL[26]
					H_2O	2003.39	2400 ± 1200	100	
28 Oct 1998	1.09	-7.59	0.93	-8.30	HCN	3302.55	≤ 5.4	$\leq 0.18 - 0.27$	CSHELL[26]
					C_2H_2	3304.17	≤ 8.3	$\leq 0.28 - 0.42$	
29 Oct 1998	1.08	-7.32	-0.93	-8.16	CH_3OH	2849	27.0 ± 0.8	$0.9 - 1.4$	UKIRT[26]
					H_2CO	2789	≤ 15	$\leq 0.5 - 0.8$	

73P/Schwassmann-Wachmann

Fragment C

Date	R_h (AU)	v_h (km/s)	Δ (AU)	v_Δ (km/s)	Molecule	λ (cm^{-1})	Q (10^{25} mol/s)	M.R. %	Instrument
07 Apr 2006	1.27	-15.27	0.33	-17.20	H_2O	3429	590 ± 60	100	NIRSPEC[27]
					C_2H_6	2986	0.9 ± 0.2	0.15 ± 0.04	
					CH_3OH	2144	< 3.0	< 0.51	
					HCN	3303	1.0 ± 0.1	0.17 ± 0.02	
					CH_4	3038	< 1.5	< 0.25	
					H_2CO	2910	< 3.0	< 0.51	
16 Apr 2006	1.19	-14.39	0.24	-15.66	H_2O	3435	620 ± 80	100	NIRSPEC[27]
					HCN	3303	1.3 ± 0.2	0.21 ± 0.04	
					C_2H_2	3300	1.4 ± 0.3	0.23 ± 0.06	
					CH_4	3038	< 2.4	< 0.39	
					H_2CO	2910	< 3.0	< 0.48	
03 May 2006	1.06	-11.54	0.11	-10.96	H_2O	3435	817 ± 98	100	NIRSPEC[28]
					CO	2151.19	< 21	< 2.6	
					C_2H_6	2986	0.53 ± 0.26	0.065 ± 0.033	
09 May 2006	1.03	-10.05	0.08	-5.09	H_2O	3435	1136 ± 154	100	NIRSPEC[28]
					HCN	3303	3.4 ± 0.9	0.30 ± 0.09	
					C_2H_6	2986	1.3 ± 0.4	0.11 ± 0.03	
					C_2H_2	3300	< 15	< 0.44	
14 May 2006	1.00	-8.60	0.08	2.81	H_2O	3435	712 ± 48	100	NIRSPEC[28]
					CH_3OH	2144	1.06 ± 0.21	0.149 ± 0.029	
					HCN	3303	2.30 ± 0.22	0.211 ± 0.010	
					C_2H_6	2986	0.77 ± 0.08	0.11 ± 0.04	
					C_2H_2	3300	0.35 ± 0.14	0.049 ± 0.020	

<div align="center">Continue in the next page</div>

---

[24]For CO and C_2H_6, Weaver et al. (1999) and Mumma et al. (2000) reported quite different results. For the discussion in this thesis we used the results from Mumma et al. (2000), since they reported a clear detection for both the molecules.

[25]Mumma et al. (2000)

[26]Weaver et al. (1999)

[27]Villanueva et al. (2006)

[28]Dello Russo et al. (2007)

15 May 2006	0.99	-8.30	0.08	4.25	H_2O	3435	1090 ± 62	100	NIRSPEC[28]
					CH_3OH	2144	2.77 ± 0.41	0.254 ± 0.037	
					HCN	3303	0.53 ± 0.26	0.065 ± 0.033	
					C_2H_6	2986	1.30 ± 0.13	0.119 ± 0.011	
					C_2H_2	3300	< 0.36	< 0.033	
27 May 2006	0.95	-4.10	0.15	12.50	H_2O	2151.19	1310 ± 69	100	CSHELL[29]
					CO	2151.19	6.1 ± 2.3	0.47 ± 0.19	
30 May 2006	0.95	-3.17	0.17	13.10	H_2O	2151.19	1220 ± 59	100	CSHELL[29]
					CO	2151.19	7.1 ± 2.1	0.58 ± 0.18	

Fragment B

Date	R_h (AU)	v_h (km/s)	Δ (AU)	v_Δ (km/s)	Molecule	λ (cm^{-1})	Q (10^{25} mol/s)	M.R. %	Instrument
15 Apr 2006	1.20	-14.48	0.25	-15.53	H_2O	3429	100 ± 20	100	NIRSPEC[30]
					C_2H_6	2986	< 0.3	< 0.3	
					HCN	3303	< 0.2	< 0.2	
09 May 2006	1.03	-9.93	0.078	-7.4	H_2O	3514	3500 ± 200	100	SUBARU[31]
					HCN	3320	9.5 ± 1.1	0.27 ± 0.03	
					C_2H_6	2990	5.6 ± 0.4	0.16 ± 0.01	
					H_2O	3435	3483 ± 280	100	NIRSPEC[32]
					CO	2151.19	< 67	< 1.9	
					CH_3OH	2144	7.17 ± 1.31	0.21 ± 0.04	
					HCN	3303	8.78 ± 0.80	0.25 ± 0.03	
					C_2H_6	2986	4.74 ± 0.54	0.14 ± 0.02	
					C_2H_2	3300	< 3.5	< 0.10	
10 May 2006	1.03	-9.75	0.074	-6.4	H_2O	3514	1900 ± 200	100	SUBARU[33]
					HCN	3320	6.6 ± 0.7	0.35 ± 0.02	
					C_2H_6	2990	402 ± 0.5	0.22 ± 0.02	
14 May 2006	1.00	-8.92	0.07	-0.13	H_2O	3435	1208 ± 88	100	NIRSPEC[34]
					CH_3OH	2144	2.14 ± 0.29	0.18 ± 0.02	
					HCN	3303	3.37 ± 0.34	0.28 ± 0.02	
					C_2H_6	2986	1.88 ± 0.28	0.16 ± 0.03	
					C_2H_2	3300	0.31 ± 0.13	0.03 ± 0.01	
15 May 2006	1.00	-8.61	0.07	1.71	H_2O	3435	502 ± 29	100	NIRSPEC[34]
					CH_3OH	2144	1.70 ± 0.33	0.34 ± 0.07	
					HCN	3303	1.44 ± 0.14	0.29 ± 0.02	
					C_2H_6	2986	0.97 ± 0.10	0.19 ± 0.02	
					C_2H_2	3300	< 0.30	< 0.06	

17P/Holmes (outburst)

Date	R_h (AU)	v_h (km/s)	Δ (AU)	v_Δ (km/s)	Molecule	λ (cm^{-1})	Q (10^{25} mol/s)	M.R. %	Instrument
27 Oct 2007	2.45	6.65	1.63	-3.07	H_2O	3429	45000 ± 5700	100	NIRSPEC[33]
					CH_3OH	2852	1010 ± 160	2.25 ± 0.43	
					C_2H_6	2982	8010 ± 790	1.78 ± 0.26	
					HCN	3297	2420 ± 220	0.54 ± 0.07	
					C_2H_2	3297	1500 ± 180	0.34 ± 0.05	
31 Oct 2007	2.46	6.72	1.62	-1.82	H_2O	3429	17500 ± 3000	100	NIRSPEC[33]
					CH_3OH	2852	520 ± 140	3.0 ± 1.0	
					C_2H_6	2982	332 ± 76	1.90 ± 0.54	
02 Nov 2007	2.47	6.79	1.62	-1.02	H_2O	3429	6600 ± 1400	100	NIRSPEC[33]
					C_2H_6	2982	155 ± 33	2.3 ± 0.7	

[29]DiSanti et al. (2007)

[30]Villanueva et al. (2006)

[31]Kobayashi et al. (2007)

[32]Dello Russo et al. (2007)

[33]Dello Russo et al. (2008)

9P/Tempel 1

Date	R_h (AU)	v_h (km/s)	Δ (AU)	v_Δ (km/s)	Molecule	λ (cm^{-1})	Q (10^{25} mol/s)	M.R. %	Instrument
					Pre-impact				
03 Jun 2005	1.54	-3.61	0.76	5.35	H_2O	3429	1244 ± 95	100	NIRSPEC[34]
					C_2H_6	2982	2.42 ± 0.47	0.19 ± 0.04	
					CH_3OH	2852	16.4 ± 2.1	1.32 ± 0.20	
					H_2O	3429	1184 ± 207	100	
					HCN	3297	2.11 ± 0.61	0.18 ± 0.06	
04 Jul 2005	1.51	-0.13	0.89	9.11	H_2O	3429	1037 ± 174	100	NIRSPEC[34]
					C_2H_6	2982	2.8 ± 1.2	0.27 ± 0.12	
					CH_3OH	2852	11.1 ± 2.0	1.07 ± 0.26	
					Post-impact				
04 Jul 2005	1.51	-0.13	0.89	9.11	H_2O	3429	1835 ± 256	100	NIRSPEC[34]
					C_2H_6	2982	6.13 ± 0.43	0.35 ± 0.03	
					CH_3OH	2852	17.2 ± 2.9	0.99 ± 0.17	
					H_2O	3429	1703 ± 192	100	
					HCN	3297	3.61 ± 0.37	0.21 ± 0.03	
					C_2H_2	3297	2.06 ± 0.61	0.13 ± 0.04	
					CH_4	3037	9.22 ± 5.00	0.54 ± 0.30	
					H_2CO	3037	15.3 ± 2.7	0.84 ± 0.18	
					H_2O	2148	2100 ± 400	100	
					CO	2148	91.3 ± 32.0	4.3 ± 1.7	
05 Jul 2005	1.51	-0.02	0.90	8.99	H_2O	2148	2000 ± 400	100	NIRSPEC[34]
					CO	2148	86.5 ± 16.0	4.3 ± 1.7	

6P/D'Arrest

Date	R_h (AU)	v_h (km/s)	Δ (AU)	v_Δ (km/s)	Molecule	λ (cm^{-1})	Q (10^{25} mol/s)	M.R. %	Instrument
28 Jul 2008	1.37	-3.02	0.37	-5.14	CH_3OH	2859.6	5.38 ± 0.99	2.11 ± 0.48	NIRSPEC[35]
					C_2H_6	2989.3	0.91 ± 0.23	0.36 ± 0.10	
					H_2O	3377.3	255 ± 49	100	
11 Ago 2008	1.35	-0.51	0.35	0.61	CH_3OH	2863	6.81 ± 1.20	1.42 ± 0.30	NIRSPEC[35]
					C_2H_6	2989.3	1.23 ± 0.26	0.26 ± 0.06	
					H_2O	3510.4	481 ± 86	100	
					H_2CO	2778.1	1.7 ± 0.4	0.36 ± 0.09	
					HCN	3304.6	0.16 ± 0.04	0.03 ± 0.01	
					C_2H_2	3304.6	< 2.5	< 0.05	

---

[34]Mumma et al. (2005)
[35]Dello Russo et al. (2009a)

Bibliography

A'Hearn, M. F., Schleicher, D. G., Feldman, P. D., 1983, The discovery of S_2 in comet IRAS-Araki-Alcock 1983d, ApJL, 274, L99–L103

A'Hearn, M. F., Millis, R. L., Schleicher, D. G., Osip, D. J., Birch, P. V., 1995, The ensemble properties of comets: Results from narrowband photometry of 85 comets, 1976-1992., Icarus, 118, 223–270

Altenhoff, W. J., Batrla, W. K., Huchtmeier, W. K., Schmidt, J., Stumpff, P., Walmsley, M., 1983, Radio observations of Comet 1983d, A&A, 125, L19–L22

Altwegg, K., Bockelée-Morvan, D., 2003, Isotopic Abundances in Comets, Space Science Reviews, 106, 139–154

Bird, M. K., Huchtmeier, W. K., Gensheimer, P., Wilson, T. L., Janardhan, P., Lemme, C., 1997, Radio detection of ammonia in comet Hale-Bopp, A&A, 325, L5–L8

Biver, N., Bockelée-Morvan, D., Colom, P., Crovisier, J., Germain, B., Lellouch, E., Davies, J. K., Dent, W. R. F., Moreno, R., Paubert, G., Wink, J., Despois, D., Lis, D. C., Mehringer, D., Benford, D., Gardner, M., Phillips, T. G., Gunnarsson, M., Rickman, H., Winnberg, A., Bergman, P., Johansson, L. E. B., Rauer, H., 1997, Long-term Evolution of the Outgassing of Comet Hale-Bopp From Radio Observations, Earth Moon and Planets, 78, 5–11

Bockelee-Morvan, D., Colom, P., Crovisier, J., Despois, D., Paubert, G., 1991, Microwave detection of hydrogen sulphide and methanol in Comet Austin (1989c1), Nature, 350, 318–320

Bockelee-Morvan, D., Gautier, D., Lis, D. C., Young, K., Keene, J., Phillips, T., Owen, T., Crovisier, J., Goldsmith, P. F., Bergin, E. A., Despois, D., Wootten, A., 1998, Deuterated Water in Comet C/1996 B2 (Hyakutake) and Its Implications for the Origin of Comets, Icarus, 133, 147–162

Bockelée-Morvan, D., Lis, D. C., Wink, J. E., Despois, D., Crovisier, J., Bachiller, R., Benford, D. J., Biver, N., Colom, P., Davies, J. K., Gérard, E., Germain, B., Houde, M., Mehringer, D., Moreno, R., Paubert, G., Phillips, T. G., Rauer, H., 2000, New molecules found in comet C/1995 O1 (Hale-Bopp). Investigating the link between cometary and interstellar material, A&A, 353, 1101–1114

Bockelée-Morvan, D., Crovisier, J., Mumma, M. J., Weaver, H. A., 2004, The composition of cometary volatiles, in Comets II, (Ed.) M. C. Festou & H. U. Keller & H. A. Weaver, pp. 391–423, University of Arizona press, Tucson

Böhnhardt, H., Mumma, M. J., Villanueva, G. L., DiSanti, M. A., Bonev, B. P., Lippi, M., Käufl, H. U., 2008, The Unusual Volatile Composition of the Halley-Type Comet 8P/Tuttle: Addressing the Existence of an Inner Oort Cloud, ApJL, 683, L71–L74

Bonev, B. P., 2005, Towards a Chemical Taxonomy of Comets: Infrared Spectroscopic Methods for Quantitative Measurements of Cometary Water (With an Independent Chapter on Mars Polar Science) , The University of Toledo

Bonev, B. P., Mumma, M. J., Radeva, Y. L., DiSanti, M. A., Gibb, E. L., Villanueva, G. L., 2008, The Peculiar Volatile Composition of Comet 8P/Tuttle: A Contact Binary of Chemically Distinct Cometesimals?, ApJL, 680, L61–L64

Bonev, B. P., Mumma, M. J., Gibb, E. L., DiSanti, M. A., Villanueva, G. L., Magee-Sauer, K., Ellis, R. S., 2009, Comet C/2004 Q2 (Machholz): Parent Volatiles, a Search for Deuterated Methane, and Constraint on the CH_4 Spin Temperature, ApJ, 699, 1563–1572

Charnoz, S., Morbidelli, A., 2007, Coupling dynamical and collisional evolution of small bodies. II. Forming the Kuiper belt, the Scattered Disk and the Oort Cloud, Icarus, 188, 468–480

Combi, M. R., Delsemme, A. H., 1980, Neutral cometary atmospheres. II - The production of CN in comets, ApJ, 237, 641–645

Combi, M. R., Mäkinen, J. T. T., Bertaux, J., Lee, Y., Quémerais, E., 2009, Water Production in Comets 2001 Q4 (NEAT) and 2002 T7 (LINEAR) Determined from SOHO/SWAN Observations, AJ, 137, 4734–4743

Cremonese, G., Boehnhardt, H., Crovisier, J., Rauer, H., Fitzsimmons, A., Fulle, M., Licandro, J., Pollacco, D., Tozzi, G. P., West, R. M., 1997, Neutral Sodium from Comet Hale-Bopp: A Third Type of Tail, ApJL, 490, L199–L202, `arXiv:astro-ph/9710022`

Crovisier, J., 1989, Infrared cometary spectroscopy, in Infrared Spectroscopy in Astronomy, (Ed.) B. H. Kaldeich, vol. 290 of ESA Special Publication, pp. 15–36

Crovisier, J., Encrenaz, T., 1983, Infrared fluorescence of molecules in comets - The general synthetic spectrum, A& A, 126, 170–182

Crovisier, J., Bockelee-Morvan, D., Colom, P., Despois, D., Paubert, G., 1991, Microwave observations of hydrogen sulfide and searches for other sulfur compounds in Comets Austin (1989c1) and Levy (1990c), Icarus, 93, 246–258

Dello Russo, N., DiSanti, M. A., Mumma, M. J., Magee-Sauer, K., Rettig, T. W., 1998, Carbonyl Sulfide in Comets C/1996 B2 (Hyakutake) and C/1995 O1 (Hale-Bopp): Evidence for an Extended Source in Hale-Bopp, Icarus, 135, 377–388

134

Dello Russo, N., Mumma, M. J., DiSanti, M. A., Magee-Sauer, K., Novak, R., Rettig, T. W., 2000, Water Production and Release in Comet C/1995 O1 Hale-Bopp, Icarus, 143, 324–337

Dello Russo, N., Mumma, M. J., DiSanti, M. A., Magee-Sauer, K., Novak, R., 2001, Ethane Production and Release in Comet C/1995 O1 Hale-Bopp, Icarus, 153, 162–179

Dello Russo, N., DiSanti, M. A., Magee-Sauer, K., Gibb, E., Mumma, M. J., 2002, Production of C_2H_6 and H_2O in comet 2002 C1 Ikeya-Zhang on UT 2002 April 13.7 - 13.9, in Asteroids, Comets, and Meteors: ACM 2002, (Ed.) B. Warmbein, vol. 500 of ESA Special Publication, pp. 689–692

Dello Russo, N., DiSanti, M. A., Magee-Sauer, K., Gibb, E. L., Mumma, M. J., Barber, R. J., Tennyson, J., 2004, Water production and release in Comet 153P/Ikeya-Zhang (C/2002 C1): accurate rotational temperature retrievals from hot-band lines near 2.9μm, Icarus, 168, 186–200

Dello Russo, N., Mumma, M. J., DiSanti, M. A., Magee-Sauer, K., Gibb, E. L., Bonev, B. P., McLean, I. S., Xu, L., 2006, A high-resolution infrared spectral survey of Comet C/1999 H1 Lee, Icarus, 184, 255–276

Dello Russo, N., Vervack, R. J., Weaver, H. A., Biver, N., Bockelée-Morvan, D., Crovisier, J., Lisse, C. M., 2007, Compositional homogeneity in the fragmented comet 73P/Schwassmann-Wachmann 3, Nature, 448, 172–175

Dello Russo, N., Vervack, Jr., R. J., Weaver, H. A., Montgomery, M. M., Deshpande, R., Fernández, Y. R., Martin, E. L., 2008, The Volatile Composition of Comet 17P/Holmes after its Extraordinary Outburst, ApJ, 680, 793–802

Dello Russo, N., Vervack, R. J., Weaver, H. A., Kawakita, H., Kobayashi, H., Biver, N., Bockelée-Morvan, D., Crovisier, J., 2009a, The Parent Volatile Composition of 6P/d'Arrest and a Chemical Comparison of Jupiter-Family Comets Measured at Infrared Wavelengths, ApJ, 703, 187–197

Dello Russo, N., Vervack, R. J., Weaver, H. A., Lisse, C. M., 2009b, Infrared measurements of the chemical composition of C/2006 P1 McNaught, Icarus, 200, 271–279

Despois, D., Crovisier, J., Bockelee-Morvan, D., Gerard, E., Schraml, J., 1986, Observations of hydrogen cyanide in comet Halley, A&A, 160, L11–L12

DiSanti, M. A., Mumma, M. J., 2008, Reservoirs for Comets: Compositional Differences Based on Infrared Observations, Space Science Reviews, 138, 127–145

DiSanti, M. A., Mumma, M. J., Dello Russo, N., Magee-Sauer, K., 2001, Carbon Monoxide Production and Excitation in Comet C/1995 O1 (Hale-Bopp): Isolation of Native and Distributed CO Sources, Icarus, 153, 361–390

DiSanti, M. A., Dello Russo, N., Magee-Sauer, K., Gibb, E. L., Reuter, D. C., Mumma, M. J., 2002, CO, H_2CO, and CH_3OH in comet 2002 C1 Ikeya-Zhang, in Asteroids, Comets, and Meteors: ACM 2002, (Ed.) B. Warmbein, vol. 500 of ESA Special Publication, pp. 571–574

DiSanti, M. A., Mumma, M. J., Dello Russo, N., Magee-Sauer, K., Griep, D. M., 2003, Evidence for a dominant native source of carbon monoxide in Comet C/1996 B2 (Hyakutake), Journal of Geophysical Research (Planets), 108

DiSanti, M. A., Anderson, W. M., Villanueva, G. L., Bonev, B. P., Magee-Sauer, K., Gibb, E. L., Mumma, M. J., 2007, Depleted Carbon Monoxide in Fragment C of the Jupiter-Family Comet 73P/Schwassmann-Wachmann 3, ApJL, 661, L101–L104

DiSanti, M. A., Villanueva, G. L., Milam, S. N., Zack, L. N., Bonev, B. P., Mumma, M. J., Ziurys, L. M., Anderson, W. M., 2009, A multi-wavelength study of parent volatile abundances in Comet C/2006 M4 (SWAN), Icarus, 203, 589–598

Eberhardt, P., 1999, Comet Halley's Gas Composition and Extended Sources: Results from the Neutral Mass Spectrometer on Giotto, Space Science Reviews, 90, 45–52

Eberhardt, P., Reber, M., Krankowsky, D., Hodges, R. R., 1995, The D/H and $^{18}O/^{16}O$ ratios in water from comet P/Halley, A&A, 302, 301–316

Edwards, D. P., 1992, GENLN2: A general line-by-line atmospheric transmittance and radiance model. Version 3.0: Description and users guide, Tech. rep., National Center For Atmospheric Research Boulder, Colorado

Ehrenfreund, P., Charnley, S. B., Wooden, D., 2004, From interstellar material to comet particles and molecules, in Comets II, (Ed.) Festou, M. C., Keller, H. U., & Weaver, H. A., pp. 115–133, University of Arizona press, Tucson

Feldman, P. D., Festou, M. C., Tozzi, G. P., Weaver, H. A., 1997, The CO_2/CO Abundance Ratio in 1P/Halley and Several Other Comets Observed by IUE and HST, ApJ, 475, 829–834

Feldman, P. D., Cochran, A. L., Combi, M. R., 2004, Spectroscopic investigations of fragment species in the coma, in Comets II, (Ed.) M. C. Festou & H. U. Keller & H. A. Weaver, pp. 425–447, University of Arizona press, Tucson

Flynn, G. J., Bleuet, P., Borg, J., Bradley, J. P., Brenker, F. E., Brennan, S., Bridges, J., Brownlee, D. E., Bullock, E. S., Burghammer, M., Clark, B. C., Dai, Z. R., Daghlian, C. P., Djouadi, Z., Fakra, S., Ferroir, T., Floss, C., Franchi, I. A., Gainsforth, Z., Gallien, J., Gillet, P., Grant, P. G., Graham, G. A., Green, S. F., Grossemy, F., Heck, P. R., Herzog, G. F., Hoppe, P., Hörz, F., Huth, J., Ignatyev, K., Ishii, H. A., Janssens, K., Joswiak, D., Kearsley, A. T., Khodja, H., Lanzirotti, A., Leitner, J., Lemelle, L., Leroux, H., Luening, K., MacPherson, G. J., Marhas, K. K., Marcus, M. A., Matrajt, G., Nakamura, T., Nakamura-Messenger, K., Nakano, T., Newville, M., Papanastassiou, D. A., Pianetta, P., Rao, W., Riekel, C., Rietmeijer, F. J. M., Rost, D., Schwandt, C. S., See, T. H., Sheffield-Parker, J., Simionovici, A., Sitnitsky, I., Snead, C. J., Stadermann, F. J., Stephan, T., Stroud, R. M., Susini, J., Suzuki, Y., Sutton, S. R., Taylor, S., Teslich, N., Troadec, D., Tsou, P., Tsuchiyama, A., Uesugi, K., Vekemans, B., Vicenzi, E. P., Vincze, L., Westphal, A. J., Wozniakiewicz, P., Zinner, E., Zolensky, M. E., 2006, Elemental Compositions of Comet 81P/Wild 2 Samples Collected by Stardust, Science, 314, 1731–1735

Fray, N., Bénilan, Y., Cottin, H., Gazeau, M., Crovisier, J., 2005, The origin of the CN radical in comets: A review from observations and models, P&SS, 53, 1243–1262

Gibb, E. L., Mumma, M. J., Dello Russo, N., DiSanti, M. A., Magee-Sauer, K., 2003, Methane in Oort cloud comets, Icarus, 165, 391–406

Gibb, E. L., DiSanti, M. A., Magee-Sauer, K., Dello Russo, N., Bonev, B. P., Mumma, M. J., 2007, The organic composition of C/2001 A2 (LINEAR). II. Search for heterogeneity within a comet nucleus, Icarus, 188, 224–232

Gomes, R., Levison, H. F., Tsiganis, K., Morbidelli, A., 2005, Origin of the cataclysmic Late Heavy Bombardment period of the terrestrial planets, Nature, 435, 466–469

Greenstein, J. L., 1958, High-resolution spectra of Comet MRKOS (1957d), ApJ, 128, 106–106

Hanner, M. S., Bradley, J. P., 2004, Composition and mineralogy of cometary dust, in Comets II, (Ed.) Festou, M. C., Keller, H. U., & Weaver, H. A., pp. 555–564, University of Arizona press, Tucson

Harmon, J. K., Nolan, M. C., Howell, E. S., Giorgini, J. D., 2008, Comet 8P/Tuttle: Arecibo Radar Observations of the First Bilobate Comet, LPI Contributions, 1405

Hase, F., Demoulin, P., Sauval, A., Toon, G., Bernath, P., Goldman, A., Hannigan, J., Rinsland, C., 2006, An empirical line-by-line model for the infrared solar transmittance spectrum from 700 to 5000 cm^{-1}, Journal of Quantitative Spectroscopy and Radiative Transfer, 102, 450–463

Haser, L., 1957, Distribution d'intensite dans la tete d'une comete, Bulletin de la Societe Royale des Sciences de Liege, 43, 740–750

Herbst, E., Adams, N. G., Smith, D., 1983, Laboratory measurements of ion-molecule reactions pertaining to interstellar hydrocarbon synthesis, ApJ, 269, 329–333

Herzberg, G., 1939, Molecular spectra and molecular structure. Vol. 1: Spectra of Diatomic Molecules, D. Van Nostrand Company, INC.

Hiraoka, K., Sato, T., Takayama, T., 2000, Laboratory Simulation of Chemical Reactions in Interstellar Ices, in From Molecular Clouds to Planetary, (Ed.) Y. C. Minh & E. F. van Dishoeck, vol. 197 of IAU Symposium, p. 283

Hoban, S., Mumma, M., Reuter, D. C., Disanti, M., Joyce, R. R., Storrs, A., 1991, A tentative identification of methanol as the progenitor of the 3.52-micron emission feature in several comets, Icarus, 93, 122–134

Jacquinet-Husson, N., Scott, N. A., Chédin, A., Crépeau, L., Armante, R., Capelle, V., Orphal, J., Coustenis, A., Boonne, C., Poulet-Crovisier, N., Barbe, A., Birk, M., Brown, L. R., Camy-Peyret, C., Claveau, C., Chance, K., Christidis, N., Clerbaux, C., Coheur, P. F., Dana, V., Daumont, L., De Backer-Barilly, M. R., Di Lonardo, G., Flaud, J. M., Goldman, A., Hamdouni, A., Hess, M., Hurley, M. D., Jacquemart, D., Kleiner, I,

Köpke, P., Mandin, J. Y., Massie, S., Mikhailenko, S., Nemtchinov, V., Nikitin, A., Newnham, D., Perrin, A., Perevalov, V. I., Pinnock, S., Régalia-Jarlot, L., Rinsland, C. P., Rublev, A., Schreier, F., Schult, L., Smith, K. M., Tashkun, S. A., Teffo, J. L., Toth, R. A., Tyuterev, V. G., Vander Auwera, J., Varanasi, P., Wagner, G., 2008, The GEISA spectroscopic database: Current and future archive for Earth and planetary atmosphere studies, Journal of Quantitative Spectroscopy and Radiative Transfer, 109, 1043–1059

Jewitt, D., 2008, Kuiper Belt and Comets: An Observational Perspective, in Saas-Fee Advanced Course 35: Trans-Neptunian Objects and Comets, (Ed.) D. J. D. . A. M. . H. Rauer, pp. 1–78

Kawakita, H., Dello Russo, N., Kobayashi, H., 2008, Revised Water Hot-Band Emission Model in Comets, LPI Contributions, 1405, 8104

Kissel, J., Brownlee, D. E., Buchler, K., Clark, B. C., Fechtig, H., Grun, E., Hornung, K., Igenbergs, E. B., Jessberger, E. K., Krueger, F. R., Kuczera, H., McDonnell, J. A. M., Morfill, G. M., Rahe, J., Schwehm, G. H., Sekanina, Z., Utterback, N. G., Volk, H. J., Zook, H. A., 1986, Composition of comet Halley dust particles from Giotto observations, Nature, 321, 336–337

Kobayashi, H., Kawakita, H., 2009, Formation Conditions of Icy Materials in Comet C/2004 Q2 (Machholz). I. Mixing Ratios of Organic Volatiles, ApJ, 703, 121–130

Kobayashi, H., Kawakita, H., Mumma, M. J., Bonev, B. P., Watanabe, J., Fuse, T., 2007, Organic Volatiles in Comet 73P-B/Schwassmann-Wachmann 3 Observed during Its Outburst: A Clue to the Formation Region of the Jupiter-Family Comets, ApJL, 668, L75–L78

Kobayashi, H., Bockelée-Morvan, D., Kawakita, H., Dello Russo, N., Jehin, E., Manfroid, J., Smette, A., Hutsemékers, D., Stüwe, J., Weiler, M., Arpigny, C., Biver, N., Cochran, A., Crovisier, J., Magain, P., Sana, H., Schulz, R., Vervack, R. J., Weaver, H., Zucconi, J.-M., 2010, High-dispersion infrared spectroscopic observations of comet 8P/Tuttle with VLT/CRIRES , A&A, 509

Kurucz, R. L., 1997, Progress on model atmospheres and line data, in IAU Symposium, (Ed.) T. R. Bedding, A. J. Booth, & J. Davis, vol. 189 of IAU Symposium, pp. 217–226

Lamy, P. L., Toth, I., Fernandez, Y. R., Weaver, H. A., 2004, The sizes, shapes, albedos, and colors of cometary nuclei, in Comets II, (Ed.) M. C. Festou & H. U. Keller & H. A. Weaver, pp. 223–264, University of Arizona press, Tucson

Levison, H. F., 1996, Comet Taxonomy, in Completing the Inventory of the Solar System, (Ed.) T. Rettig & J. M. Hahn, vol. 107 of PASP Conference Series, pp. 173–191

Magee-Sauer, K., Mumma, M. J., DiSanti, M. A., Russo, N. D., Rettig, T. W., 1999, Infrared Spectroscopy of the ν_3 Band of Hydrogen Cyanide in Comet C/1995 O1 Hale-Bopp, Icarus, 142, 498–508

Magee-Sauer, K., Dello Russo, N., DiSanti, M. A., Gibb, E. L., Mumma, M. J., 2002a, Production of HCN and C_2H_2 in comet C/2002 C1 Ikeya-Zhang on UT 2002 April 13.8, in Asteroids, Comets, and Meteors: ACM 2002, (Ed.) B. Warmbein, vol. 500 of ESA Special Publication, pp. 549–552

Magee-Sauer, K., Mumma, M. J., DiSanti, M. A., Dello Russo, N., 2002b, Hydrogen cyanide in comet C/1996 B2 Hyakutake, Journal of Geophysical Research (Planets), 107

Maki, A., 1996, Infrared Transitions of $H^{12}C^{14}N$ and $H^{12}C^{15}N$ between 500 and 10000 cm^{-1}, Journal of Molecular Spectroscopy, 180, 323–336

Malathy Devi, V., Benner, D., Smith, M., Rinsland, C., Sharpe, S., Sams, R., 2003, A multispectrum analysis of the ν_1 band of $H^{12}C^{14}N$: Part I. Intensities, self-broadening and self-shift coefficients, Journal of Quantitative Spectroscopy and Radiative Transfer, 82, 319–341

Matthews, C. N., Minard, R. D., 2008, Hydrogen cyanide polymers connect cosmochemistry and biochemistry, in IAU Symposium, (Ed.) S. Kwok & S. Sandford, vol. 251 of IAU Symposium, pp. 453–458

Meech, K. J., Svoren, J., 2004, Using cometary activity to trace the physical and chemical evolution of cometary nuclei, in Comets II, (Ed.) M. C. Festou & H. U. Keller & H. A. Weaver, pp. 317–335, University of Arizona press, Tucson

Meier, R., Owen, T. C., Matthews, H. E., Jewitt, D. C., Bockelee-Morvan, D., Biver, N., Crovisier, J., Gautier, D., 1998, A Determination of the HDO/H_2O Ratio in Comet C/1995 O1 (Hale-Bopp), Science, 279, 842–844

Mumma, M. J., Weaver, H. A., Larson, H. P., Williams, M., Davis, D. S., 1986, Detection of water vapor in Halley's comet, Science, 232, 1523–1528

Mumma, M. J., DiSanti, M. A., Dello Russo, N., Fomenkova, M., Magee-Sauer, K., Kaminski, C. D., Xie, D. X., 1996, Detection of Abundant Ethane and Methane, Along with Carbon Monoxide and Water, in Comet C/1996 B2 Hyakutake: Evidence for Interstellar Origin, Science, 272, 1310–1314

Mumma, M. J., DiSanti, M. A., Dello Russo, N., Magee-Sauer, K., Rettig, T. W., 2000, Detection of CO and Ethane in Comet 21P/Giacobini-Zinner: Evidence for Variable Chemistry in the Outer Solar Nebula, ApJL, 531, L155–L159

Mumma, M. J., Dello Russo, N., DiSanti, M. A., Magee-Sauer, K., Novak, R. E., Brittain, S., Rettig, T., McLean, I. S., Reuter, D. C., Xu, L., 2001a, Organic Composition of C/1999 S4 (LINEAR): A Comet Formed Near Jupiter?, Science, 292, 1334–1339

Mumma, M. J., McLean, I. S., DiSanti, M. A., Larkin, J. E., Dello Russo, N., Magee-Sauer, K., Becklin, E. E., Bida, T., Chaffee, F., Conrad, A. R., Figer, D. F., Gilbert, A. M., Graham, J. R., Levenson, N. A., Novak, R. E., Reuter, D. C., Teplitz, H. I., Wilcox, M. K., Xu, L., 2001b, A Survey of Organic Volatile Species in Comet C/1999 H1 (Lee) Using NIRSPEC at the Keck Observatory, ApJ, 546, 1183–1193

Mumma, M. J., DiSanti, M. A., Magee-Sauer, K., Bonev, B. P., Villanueva, G. L., Kawakita, H., Dello Russo, N., Gibb, E. L., Blake, G. A., Lyke, J. E., Campbell, R. D., Aycock, J., Conrad, A., Hill, G. M., 2005, Parent Volatiles in Comet 9P/Tempel 1: Before and After Impact, Science, 310, 270–274

Oort, J. H., 1950, The structure of the cloud of comets surrounding the Solar System and a hypothesis concerning its origin, Bull. Astron. Inst. Neth., 11, 91–110

Palmer, P., Wootten, A., Butler, B., Bockelee-Morvan, D., Crovisier, J., Despois, D., Yeomans, D. K., 1996, Comet Hyakutake: First Secure Detection of Ammonia in a Comet, in Bulletin of the American Astronomical Society, vol. 28, p. 927

Prialnik, D., 2006, What makes comets active?, in Asteroids, Comets, Meteors, (Ed.) L. Daniela, M. Sylvio Ferraz, & F. J. Angel, vol. 229 of IAU Symposium, pp. 153–170

Prialnik, D., Benkhoff, J., Podolak, M., 2004, Modeling the structure and activity of comet nuclei, in Comets II, (Ed.) M. C. Festou & H. U. Keller & H. A. Weaver, pp. 359–387, University of Arizona press, Tucson

Rao, K. N., Mathews, C. W., 1972, Molecular spectroscopy: modern research, edited by K. Narahari Rao and C. Weldon Mathews, Academic Press, New York, ISBN 0125806434 0125806426

Rothman, L. S., Gordon, I. E., Barbe, A., Benner, D. C., Bernath, P. F., Birk, M., Boudon, V., Brown, L. R., Campargue, A., Champion, J., Chance, K., Coudert, L. H., Dana, V., Devi, V. M., Fally, S., Flaud, J., Gamache, R. R., Goldman, A., Jacquemart, D., Kleiner, I., Lacome, N., Lafferty, W. J., Mandin, J., Massie, S. T., Mikhailenko, S. N., Miller, C. E., Moazzen-Ahmadi, N., Naumenko, O. V., Nikitin, A. V., Orphal, J., Perevalov, V. I., Perrin, A., Predoi-Cross, A., Rinsland, C. P., Rotger, M., Šimečková, M., Smith, M. A. H., Sung, K., Tashkun, S. A., Tennyson, J., Toth, R. A., Vandaele, A. C., Vander Auwera, J., 2009, The HITRAN 2008 molecular spectroscopic database, Journal of Quantitative Spectroscopy and Radiative Transfer, 110, 533–572

Schleicher, D., Woodney, L., 2007, Comet 8P/Tuttle, IAU circ., 8906, 2

Stern, S. A., 2003, The evolution of comets in the Oort cloud and Kuiper belt, Nature, 424, 639–642

Swings, P., 1941, Complex structure of cometary bands tentatively ascribed to the contour of the solar spectrum, Lick Observatory Bulletin, 19, 131–136

Šimečková, M., Jacquemart, D., Rothman, L. S., Gamache, R. R., Goldman, A., 2006, Einstein A-coefficients and statistical weights for molecular absorption transitions in the HITRAN database, Journal of Quantitative Spectroscopy and Radiative Transfer, 98, 130–155

Villanueva, G. L., Bonev, B. P., Mumma, M. J., Magee-Sauer, K., DiSanti, M. A., Salyk, C., Blake, G. A., 2006, The Volatile Composition of the Split Ecliptic comet 73P/Schwassmann-Wachmann 3: A Comparison of Fragments C and B, ApJL, 650, L87–L90

Villanueva, G. L., Mumma, M. J., Bonev, B. P., DiSanti, M. A., Gibb, E. L., Böhnhardt, H., Lippi, M., 2009, A Sensitive Search for Deuterated Water in Comet 8P/Tuttle, ApJL, 690, L5–L9

Watanabe, N., Nagaoka, A., Shiraki, T., Kouchi, A., 2004, Hydrogenation of CO on Pure Solid CO and CO-H_2O Mixed Ice, ApJ, 616, 638–642

Weaver, H. A., Mumma, M. J., 1984, Infrared molecular emissions from comets, ApJ, 276, 782–797

Weaver, H. A., Chin, G., Bockelée-Morvan, D., Crovisier, J., Brooke, T. Y., Cruikshank, D. P., Geballe, T. R., Kim, S. J., Meier, R., 1999, An Infrared Investigation of Volatiles in Comet 21P/Giacobini-Zinner, Icarus, 142, 482–497

Whipple, F. L., 1949, Comets, meteors and the interplanetary complex, AJ, 54, 179–180

Yamamoto, T., 1982, Evaluation of infrared line emission from constituent molecules of cometary nuclei, A&A, 109, 326–330

Publications

Refereed Publications

- H. Böhnhardt, M. J. Mumma, G. L. Villanueva, M. A. DiSanti, B. P. Bonev, **Lippi, M.**, and H. U. Käufl. The Unusual Volatile Composition of the Halley-Type Comet 8P/Tuttle: Addressing the Existence of an Inner Oort Cloud. ApJL, 683: L71-L74, August 2008.

- G. L. Villanueva, M. J. Mumma, B. P. Bonev, M. A. DiSanti, E. L. Gibb, H. Böhnhardt, and **Lippi, M.**. A Sensitive Search for Deuterated Water in Comet 8P/Tuttle. ApJL, 690: L5-L9, January 2009.

Oral Presentations and Posters

- **M. Lippi**, H. Böhnhardt, M. J. Mumma, G. L. Villanueva, M. A. DiSanti, and B. Bonev. A comprehensive study of the composition of comets 8P/Tuttle and C/2007 W1 Boattini, from IR high resolution spectroscopy observations, performed with CRIRES at VLT. In European Planetary Science Congress 2009, Potsdam, Germany, 14-18 September 2009. (Oral)

- **M. Lippi**, M. J. Mumma, G. L. Villanueva, M. A. DiSanti, B. Bonev, and H. Böhnhardt. The Volatile Composition of the Periodic Comet 8P/Tuttle as Measured with CRIRES at ESO's VLT Observatory. ACM 2008, Baltimore, Maryland, USA, 13-18 July 2008. (Poster)

- **M. Lippi**, M. J. Mumma, G. L. Villanueva, M. A. DiSanti, B. Bonev, and H. Böhnhardt. The Volatile Composition of the Periodic Comet 8P/Tuttle as Measured with CRIRES at ESO's VLT Observatory. Future Ground based Solar System Research: Synergies with Space Probes and Space Telescopes, Portoferraio, Isola D'Elba, Livorno, Italy, 8-12 September 2008. (Oral)

Acknowledgements

In these three years, and more in general during my life, I've met lots of different people that gave me their support and offered me their friendship, and I'm grateful to all of them, since they helped me to arrive at this point.

In particular, I would like to thank my supervisor, Dr Hermann Böhnhardt: he accepted me as his PhD student and he taught me many things about comets and research in general; he gave me the opportunity to observe at VLT in Chile, one of the biggest telescope worldwide, and he put me in contact with other many important professors and researchers.

I'm particular thankful to Dr. Prof. Michael J. Mumma for giving me the opportunity to work in his group, at Goddard Space Flight Center in Washington DC, and for explaining and teaching me lots of interesting things, showing me that cometary science is even more interesting than what I thought. Thanks to Geronimo L. Villanueva always present during my PhD period: he helped me with everything and he made me more confident in my capabilities as a researcher: he is not only a colleague, but also a very good friend. I'm grateful to Michael A. DiSanti for the support and the clues regarding data reduction, especially for comet Boattini, and to Boncho P. Bonev and his helpfulness; and I wish to thank Dennis Bodewits, a perfect office mate!

I would like to thank the Max Planck Institute for Solar System Research (MPS) and the International Max Planck School on Physical Processes in the Solar System and Beyond (IMPRS), in person of Dr. Dieter Schmitt, for giving me the opportunity to carry out the research presented in this thesis; the international environment that I've found since the first day helped me to open my mind and to grow both in my scientific career and in my life. I'm also glad to thank my Braunschweig supervisor Dr. Prof. Jürgen Blum, Dr. Prof. Jockers, and Dr. Prof. Dina Prialnik, in Tel Aviv University, since they always showed interest and curiosity toward my work, giving me important insights; thanks, for the support, to the German-Israeli Foundation for Scientific Research and Development.

I will forever thank my family: my grandparents (not with me anymore), my parents and my sister have always believed in me and helped me to become what I am.

My gratitude (and my love) goes especially to Giovanni: he was always by my side and he fought to keep our love alive, even when everything was really dark and confused in my mind. I'm grateful for his patience, for his understanding, for all the wonderful moments that we have had together, and I'm looking forward to have, finally, a normal life with him.

Thanks to Elena, Loredana and Elisa: unfortunately, during these three years we passed through very dark moments, but we did it together and this made us stronger: you will always be my second family.

A huge hug is reserved for some special friends that I've met here in the institute: to

Julia that is my angel, to Silvia (I love our special love-and-hate relationship), to Daniel for our Thursday evenings, to Arianna, Jean, Maria, Laura, Cecilia and Julian (the best Santa ever!).

Thanks to my friends in Italy, especially to Barbara, Michele, Francesca, Riccardo, Paola, Elena, Simona, Diego, Domenico e il Della, always present in my life, even if I was kilometers far away from them.

And last but not least, as I always do, I thank the sea, the wine, the dreams, the music, the love and the life.

Curriculum Vitae

Persönliche Daten

Name: Manuela Lippi

Geburtsdatum: 5. September 1978

Geburtsort: Carrara (Massa-Carrara), Italien

Staatsangehörigkeit: Italienisch

Schulausbildung

1984-1989:   Scuola Elementare Statale "D. Giromini"

1989-1991   Scuola Media Statale "G. Taliercio"

1991-1997   Liceo Scientifico Statale "G. Marconi"

Studium

1997-2003   Bachelor in Physics
              Università degli studi di Pisa, Italien

2003-2006   Master in Physics, course of studies Astrophysics
              Università degli studi di Pisa, Italien

2007-2010   PhD, course of studies Astrophysics
              IMPRS Katlenburg Lindau & T.U. Braunschweig, Germany